Numerical and analytical studies of kinetics, equilibrium, and stability of the chemical reaction fronts in deformable solids

vorgelegt von
Aleksandr Morozov, M.Eng.

von der Fakultät V – Verkehrs- und Maschinensysteme
der Technischen Universität Berlin
zur Erlangung des akademischen Grades

Doktor der Ingenieurwissenschaften
– Dr.-Ing. –

genehmigte Dissertation

Promotionsausschuss:

Vorsitzender:	Prof. Dr.-Ing. U. von Wagner
Gutachter:	Prof. Dr. rer. nat. W. H. Müller
	Prof. Dr. Sc. A. B. Freidin
	Prof. Dr. hab. V. A. Eremeev
	Prof. Dr.-Ing. habil. Dr. h. c. mult. H. Altenbach

Tag der wissenschaftlichen Aussprache: 22. Dezember 2020

Berlin 2021

Abstract

In the present work a chemical reaction between a solid and a diffusing constituent is considered. Many experimental observations show a coupling between mechanical stresses and the kinetics at a chemical reaction interface that propagates in a deformable solid. In general, two major processes control the chemical reaction: diffusion of a reactant through the reacted material and the consumption of the diffusing reactant by a chemical reaction. Mechanical stresses may affect the reaction front propagation via the direct influence on the diffusion process, the reaction rate, or both.

The reaction localized at a sharp interface is considered. The kinetics of the interface is modeled by using the chemical affinity tensor concept, which, in a thermodynamically consistent way, couples mechanical stresses and the chemical reaction rate. The tensorial nature of the affinity tensor follows from the fact that the reaction occurs at the oriented surface element.

The chemical interface can be retarded or even blocked by mechanical stresses. When modeling the moving interface, especially when approaching the blocking position, the question of stability arises naturally. A kinetic stability approach for the analytical stability analysis of interfaces at a chemical equilibrium is formulated and applied in several examples.

A finite element procedure for numerical simulations of the reaction front propagation is developed based on remeshing algorithms. In order to check as to whether the numerical procedure can be used for the stability analysis of the interface, several problems are examined numerically, and the results are verified with analytical solutions and predictions of stability. Also, the developed procedure is cross-validated with another numerical method for simulating the moving interface, namely CutFEM.

The last part of the manuscript reports experimental findings of IMC growth in microchips during a high-temperature storage test. The growth kinetics is modeled by applying a continuum model based on the chemical affinity tensor. By evaluating and combining a real experiment with theory, values for the diffusion coefficient and the chemical reaction constants are obtained. These values demonstrate the consistency of the developed theoretical models.

Zusammenfassung

In dieser Arbeit wird die chemische Reaktion zwischen einem Festkörper und einem diffundierenden Anteil untersucht. Viele experimentelle Beobachtungen zeigen eine Kopplung der mechanischen Spannungen mit der Kinetik an der chemischen Reaktionsfläche auf, die sich in einem verformbaren Festkörper ausbreiten kann. Hauptsächlich steuern zwei Prozesse die chemische Reaktion: die Diffusion eines Reaktionspartners innerhalb des reagierenden Materials und die Umsetzung des diffundierenden Reaktionspartners aufgrund der chemischen Reaktion. Die mechanischen Spannungen können somit eine direkte Auswirkung auf die Ausbreitung der Reaktionsfront haben, indem sie entweder den Diffusionsprozess beeinflussen, oder indem sie die Reaktionsgeschwindigkeit manipulieren, wobei auch beides gleichzeitig möglich ist.

Der Reaktionsvorgang an einer ausgezeichneten Grenzschicht wird untersucht. Die Kinetik der Grenzschicht wird mit Hilfe des Konzeptes des chemischen Affinitätstensors modelliert, der, aufbauend auf den thermodynamischen Grundgesetzen, die mechanischen Spannungen mit der chemischen Reaktionsgeschwindigkeit in Verbindung setzt. Der Affinitätstensors orientiert sich am entsprechenden Oberflächenelement, an dem der Reaktionsvorgang stattfindet.

Die Ausbreitung der chemischen Grenzschicht kann durch die mechanische Beanspruchungen behindert oder sogar komplett blockiert werden. Bei der Modellierung der sich bewegenden Grenzschicht, insbesondere beim Erreichen der Blockade, stellt sich die Frage nach der Stabilität. Ein kinetischer Ansatz für die analytische Stabilitätsuntersuchung von Grenzschichten im chemischen Gleichgewicht wird formuliert und in mehreren Beispielen angewendet.

Ein Finite-Elemente-Verfahren zur numerischen Simulation der Ausbreitung der Reaktionsfront wird mit Hilfe von Algorithmen zur Wiedervernetzung entwickelt. Um zu prüfen, ob das numerische Verfahren für die Stabilitätsanalyse an den Grenzschichten hinreichend genau ist, werden verschiedene Problemstellungen auch numerisch untersucht. Diese Ergebnisse werden mit den analytischen Lösungen und den Stabilitätsvorhersagen bestätigt. Zusätzlich wird das entwickelte Verfahren zur Simulation der Ausbreitung der sich bewegenden Grenzschicht auch mit einer anderen numerischen Methode, der sogenannten CutFEM, validiert.

Im letzten Teil der Arbeit werden experimentelle Neuheiten des IMC-Wachstums in Mikrochips während eines Hochtemperatur-Storage-Tests vorgestellt. Die Kinetik des Wachstums wird mit Hilfe eines Kontinuumsmod-

ells, das auf dem chemischen Affinitätstensor basiert, nachgestellt. Durch die Auswertung und Kombination von realen Experimenten mit der Theorie, werden der Diffusionskoeffizient und die Konstanten der chemischen Reaktion genau bestimmt. Diese Werte zeigen die Konsistenz der entwickelten theoretischen Modelle.

Preface

The research reported in this doctoral dissertation has been carried out in the Technical University of Berlin, Institute of Mechanics, Chair of Continuum Mechanics and Constitutive Theory, during 2017– 2020. The work was supported by DFG/RFFI grants (No. MU 1752/47-1 and 17-51-12055) on topic "Mechanochemistry of advanced anode designs in Li-ion batteries".

I would like to thank both my supervisors, Professor Wolfgang H. Müller and Professor Alexander Freidin, for allowing me to perform research in this fascinating interdisciplinary field of science. I am grateful for their guidance and the kind support which they gave me during the last years. They created a working environment in which I felt comfortable and could fully concentrate on my research. Further, I would like to express my gratitude to Professor Victor Eremeev and Professor Holm Altenbach for accepting my work for review and providing valuable feedback, and to Professor Utz von Wagner for being a chairman at the dissertation procedure.

The main numerical results of this work were obtained during my extremely productive research visits to the Aalto University and to the University of Warwick. For these opportunities and warm hosting, I want to thank Professor Jarkko Niiranen and Professor Łukasz Figiel. Many significant improvements for my numerical procedure were investigated during our brainstorming discussions with Dr. Mikhail Poluektov, for which I am very grateful. I am also thankful to Dr. Alexander Semencha, whose help in organizing and running the experiments cannot be overestimated.

Special gratitude should be addressed to my friends and colleagues Dr. Viacheslav Balobanov, Dr. Sergei Khakalo for their inspiration, curiosity, and fruitful discussions about this research, the science in general, and far beyond these topics. Also, I would like to thank the group of Professor Müller at the TU-Berlin, especially M.Sc. Wilhelm Rickert, M.Sc. Gregor Ganzosch, Arion Juritza, and Miriam Ziert, who helped me a lot to organize my work and private life in Germany.

And last but not least, I want to thank all my family for the belief and support and my dear Dr. Galina Lavrenteva, who was waiting for me so long.

Contents

Abstract **III**

Zusammenfassung **V**

Preface **VII**

1 Introduction **1**

2 Chemical reaction front kinetics and stability **9**
2.1 Chemical affinity tensor and general problem statement . . . 9
2.2 On stability of a chemical interface 16
2.2.1 Variation of the normal 17
2.2.2 Variation of a jump across the interface 18
2.2.3 Linearized kinetic equation for perturbed phase interfaces 20
2.2.4 Linearized kinetic equation for perturbed chemical interfaces 22
2.3 Stability of a planar chemical interface 23
2.4 Stability of a cylindrical chemical interface 30
2.5 Remark on phase transition zones 37
2.6 Conclusions 39

3 Numerical simulation and study of the chemical reaction front kinetics **43**
3.1 Description of the numerical procedure 44
3.2 Kinetics of the cylindrical chemical reaction front approaching the blocking state 48
3.3 A note about stresses caused by the interface instability . . . 51
3.4 Comparison of the CutFEM and remeshing results 55
3.4.1 CutFEM overview 55
3.4.2 Stable and unstable configurations for planar chemical interface 56
3.4.3 Stable configuration for the chemical interface under shear 59
3.4.4 Closed interface in the square domain 60
3.5 Kinetics of a chemical reaction front in a body with a pore or an inclusion 63

3.6 Conclusions 66

4 Experimental and theoretical studies of Cu-Sn intermetallic phase growth 69
4.1 Overview on intermetallic compound growth 69
4.2 Experiment overview 72
4.2.1 Specimen preparation 72
4.2.2 Experimental procedure 73
4.3 Experimental results 74
4.3.1 Chemical composition of the compounds 75
4.3.2 Thickness data for the IMC layers 77
4.4 Theoretical model 82
4.4.1 Analytical solution of a model problem 82
4.4.2 Fitting the model parameters 86
4.5 Conclusions 90

5 Conclusions 91

List of Figures XI

List of Tables XV

Bibliography XVII

A Analytical solutions for planar and cylindrical reaction fronts kinetics i
A.1 Planar reaction front kinetics i
A.2 Cylindrical reaction front kinetics iii

1 Introduction

During the last decades, much attention in continuum mechanics has been paid to the study of materials, which change their structure due to phase or chemical transformations under thermomechanical actions (see, e.g., Grinfeld [1991]; Gurtin [2000]; Abeyaratne and Knowles [2006]; Müller, Vilchevskaya, and Freidin [2015]; Freidin and Vilchevskaya [2020] and the references therein). The peculiarity of such studies is their interdisciplinarity, where coupled problems of mechanics, physics, and chemistry arise. As an example of mechanical and physical phenomena coupling, one can consider austenite-martensite phase transformation or orientation (ordering) transformation in polymers. In the present work, coupled problems of mechanics and chemistry are considered. There are two terms to describe such a coupling: mechanochemistry and chemomechanics (see, e.g., Freidin and Vilchevskaya [2020]). Both of them used to emphasize that mechanical processes influence the chemical ones and vice versa. In this work, stress-affected chemical reactions in solids are considered. Without further elaboration on etymology, the coupling of chemical and mechanical phenomena is defined by the word "mechanochemistry" in the following text.

Some examples of mechanochemical problems come from MicroElectroMechanical Systems (MEMS) and microelectronics. Oxidation processes interconnected with crack growth in polycrystalline silicon microscale parts determine the lifetime of MEMS (e.g., Muhlstein, Stach, and Ritchie [2001]; Muhlstein, Brown, and Ritchie [2002]; Muhlstein and Ritchie [2003]). In Buttner and Zacharias [2006] it was shown that on nanoscale mechanical stresses can retard the oxidation of silicon nanowires.

In microelectronics, the growth of the Intermetallic Compound (IMC) phases in Pb-free solders is of great interest. The main technological process for creating an electrical contact between components in a (micro-) electric circuit is soldering. After soldering, an IMC layer appears and establishes a mechanical contact between eutectic tin-silver solder bumps and Cu interconnects, see, e.g., Callister Jr. and Rethwisch [2010]. IMC formation is a result of diffusion and chemical reaction processes, which involve a change in shape and volume between the products and reactants. Strictly speaking, IMC formation is based on a multicomponent diffusion in solids, including vacancies as a migrating species leading to Kirkendall voiding (Dybkov [2010]; Ross, Vuorinen, and Paulasto-Kröckel [2016]). In addition to mechanical stress it can be enhanced

by electric currents (Chao *et al.* [2009]) Fig. 1.1. Consequently, the rate of IMC growth has a strong implication on solder joint reliability.

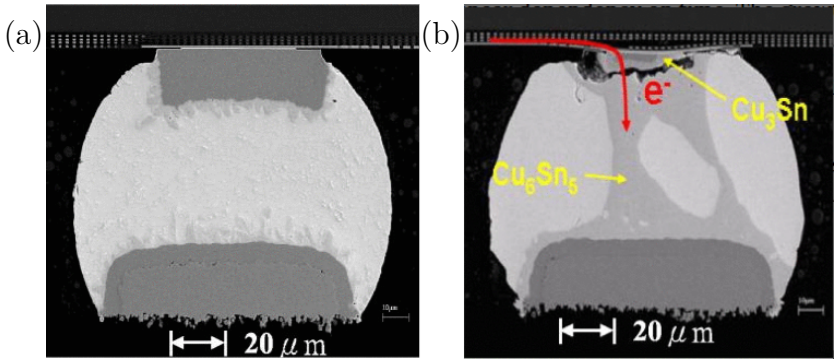

Fig. 1.1: Cross section of a solder bump prior (a) and after (b) current stressing, reprinted from Chao *et al.* [2007]

Other examples of such mechanochemical studies are Lithium-Ion Batteries (LIBs) with novel anode materials, such as silicon. The charge capacity of a silicon-based anode is about ten times higher than the capacity of graphite anodes, which are most commonly used in the industry (Kasavajjula, Wang, and Appleby [2007]). However, the lithiation and de-lithiation with large amounts of Li result in dramatic volumetric changes of 300% in the Si anodes, which can lead to fracture of the anode, Fig. 1.2. In order to cope with the large

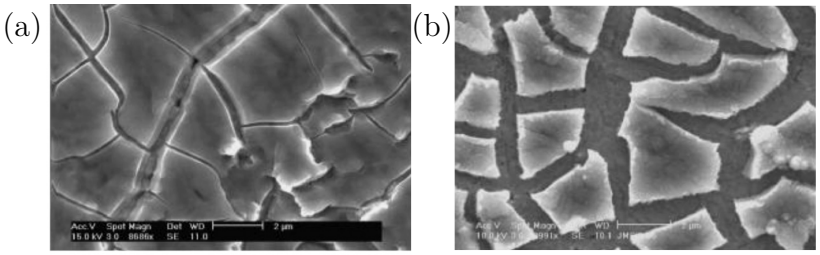

Fig. 1.2: SEM morphology of 250 nm a-Si film on Cu after 1 (a), and 30 cycles (b), reprinted from Kasavajjula, Wang, and Appleby [2007]

volume change and, therefore, to obtain better capacity retention and cycle life for Si anodes, various designs of different anode structures have been proposed, such as thin films (Bourderau, Brousse, and Schleich [1999]), nanoparticles (Liu *et al.* [2012a]), nanowires or hollow nanowires (Jia and Li [2015]; Zhao *et al.* [2012b]), and even remarkable morphologies, such as honeycomb structures (Baggetto, Danilov, and Notten [2011]). Unless accommodated by appropriate compensating deformation, the large volumetric change generates mechanical

stresses, which, in turn, may affect the diffusion (Yang [2010], Chang, Moon, and Cho [2015]). Recent experimental observation shows (Liu *et al.* [2012a]; Liu *et al.* [2012b]; McDowell *et al.* [2013]; Liu *et al.* [2013]) that there is a sharp interface between lithiated and unlithiated phases, that the lithiation process may be controlled by an interfacial chemical reaction (Zenga *et al.* [2016]), and that the chemical reaction rate is affected by mechanical stresses as well (Yang [2010]; Cui, Gao, and Qu [2012a]; Levitas and Hamed [2013]). As a result, one faces a complex coupled problem of mechanochemistry with a moving chemical reaction front.

A distinctive feature of the aforementioned examples is that the thickness of the interface is negligible when compared to the characteristic dimensions of considered solid bodies. For instance, in the case of silicon lithiation, the interface thickness is roughly 1 nm when the silicon nanoparticle or nanowire has a diameter of 150 -250 nm, see, e.g., McDowell *et al.* [2013].

In general, two major processes control the propagation of a sharp chemical reaction front: (i) diffusion of a reactant in the body undergoing a chemical reaction, (ii) consumption of the diffusing reactant by a chemical reaction at the reaction front. Thus, stresses may affect the reaction front propagation via the influence on diffusion, or the reaction rate, or both. To couple the chemical reaction rate with the mechanical stresses, some models include additional stress-dependent cross-effect terms in the diffusion flux which appears based on generalized expressions of stress-dependent scalar chemical potentials: Knyazeva [2003]; Loeffel and Anand [2011]; Cui, Gao, and Qu [2012b]; Bower and Guduru [2012]; Levitas and Hamed [2013]; Brassart and Suo [2013]. However, the velocity of the reaction front may be controlled by the reaction rate rather than by the diffusion (see, e.g., Zhao *et al.* [2012a]; Jia and Li [2015] and references therein). In this case, the influence of stresses on the reaction rate becomes important. In classical physical chemistry, the reaction rate is determined by a scalar chemical affinity, which is equal to a combination of scalar chemical potentials of the reaction constituents (Prigogine and Defay [1954]). Scalar chemical potentials were derived for the case of phase transformations in gases and liquids where stresses were reduced to a scalar pressure (Gibbs [1948]).

In the last decades of the XXth century, it was recognized, that chemical potential is a tensor in the case of solid phases. The tensorial nature followed from the fact that the equilibrium was considered not just in a point of the interface but at oriented surface element, see, e.g., Bowen [1967]; Truesdell [1969]; Grinfeld [1980]; James [1981]. Later, a tensorial nature of the chemical potential was discussed in Rusanov [2005]; Rusanov [2006]. These results could be considered as a prelude to the tensorial chemical affinity, and in Freidin [2013]; Freidin, Vilchevskaya, and Korolev [2014] it was shown, that in the case of a propagating reaction front the driving force is equal to the

normal component of the chemical affinity tensor which, in turn, equals to the combination of the chemical potential tensors of solid constituents and the chemical potential of the diffusing constituent. By this approach, mechanical stresses affect the reaction rate via the chemical affinity tensor. A kinetic equation for the propagating chemical reaction front was formulated in the form of the dependence of the normal component of the reaction front velocity on the normal component of the chemical affinity tensor.

This work can be considered as a step of further utilization of the chemical affinity tensor concept in a form developed in Freidin [2009]; Freidin [2013]; Freidin, Vilchevskaya, and Korolev [2014]; Freidin [2015]; Freidin *et al.* [2016], for studying stress-controlled chemical reaction front propagation. The kinetics of the front propagation is described within the frames of the mechanics of configurational forces. It is known that in the case of quasi-static stress-induced phase transformations the configurational force driving the interface is given by the jump of the normal component of the Eshelby stress tensor (see, e.g., monographs Silhavy [1997]; Abeyaratne and Knowles [2006]; Maugin [2010]; Gurtin [2000] and reference therein). As it was derived and approbated during the last years, in the case of stress-assisted chemical reactions, the configurational force is determined by the normal component of a chemical affinity tensor. In both cases, based on irreversible thermodynamics reasons, a kinetic equation can be formulated in the form of the dependence of the interface velocity on the corresponding configurational force. Then stresses and strains affect the interface propagation as they are presented in the configurational force.

In the case of phase transformation, a zero configurational force corresponds to phase equilibrium, but this is only a necessary condition of phase equilibrium, and the interface may be unstable in such a state (Grinfeld [1982]; Grinfeld [1990]; Grinfeld [1991]). In the case of a chemical reaction, zero configurational force corresponds to chemical equilibrium at which the reaction front propagation is blocked. Therefore, by analogy with phase transformations, the question about the stability of the reaction front in the vicinity of the blocking state arises naturally. Chemical reaction retardation and even blocking by mechanical stresses were experimentally observed in, e.g., Marcus [1982]; Kao *et al.* [1988]; Mihalyi, Jaccodine, and Delph [1999]; Heidemeyer *et al.* [2000]; Buttner and Zacharias [2006]. Special attention was paid to the influence of mechanical stresses on the stability of the growing interface in Ortiz, Repetto, and Si [1999]; Phan *et al.* [2001]; Barvosa-Carter and Aziz [2004]; Zeeshan and Venkatasubramanian [2017]; Ahmad and Viswanathan [2017]. These problems occur in the solid electrolyte interfaces modeling for Li-ion batteries, Natsiavas *et al.* [2016]; Hüter *et al.* [2017].

The importance of the stability analysis of chemical reaction fronts also follows from the following circumstances. The difference between phase and

chemical transformations is that in the latter case one deals with an open system with diffusion. One more equation – a diffusion equation – is included in the analysis in comparison with phase transformations. But a more important difference may be that a stress-induced phase transformation starts only if it provides minimization of the energy, and the origin of the transformation may be inside of a body or at the outer surface of a body depending on energy preferences and stability. For example, in the case of isotropic phases, for a spherical particle undergoing a phase transformation under increasing external strain, an equilibrium and stable new phase domain can grow only from the center of the particle if a shear module of a new phase is larger than a shear module of an initial phase. Other interfaces are unstable even if they satisfy phase equilibrium conditions. If the shear module of the new phase is less than the shear module of the initial phase, then a stable new phase grows from the outer surface of the particle (Eremeev, Freidin, and Sharipova [2003]; Eremeev, Freidin, and Sharipova [2007]). The origin of phase transformations can also be a new phase nucleus, which starts at imperfections or heterogeneities (see, e.g., Vilchevskaya, Filippov, and Freidin [2013]). Then the position of the interfaces is affected by the position of the imperfections. Moreover, two-phase microstructures may be more preferential then two-phase configurations with one smooth interface (Ball and James [1987]; Chenchiah and Bhattacharya [2008]; Antimonov, Cherkaev, and Freidin [2016]; Freidin and Sharipova [2018]). At given boundary conditions, it is a material "that decides" where to initiate a new phase and how it will grow.

The situation is different in the case of chemical reaction fronts. Here the direct reaction can go only if a diffusing reactant is delivered to the reaction front through the transformed material. In the case of the aforementioned spherical particle, the supply of the diffusing constituent is possible only through the surface of the particle. Therefore, the direct chemical reaction can start only at the outer surface and the front can propagate only inwards, irrespectively of the shear moduli of the solid reactants. In the case of the reverse reaction, the reactant is taken away from the front, and the front propagates outwards.

Therefore, starting place of the reaction and direction of the front propagation are controlled by the supply or removal of the diffusing reactant. It means that the reaction front may be forced to go in the direction of an unstable blocking state and this instability may affect the propagation of the interface. Thus, in the case of chemical reactions unstable reaction fronts are of interest not only from the mathematical point of view but also because they are physically meaningful.

Stability of the interface between material phases for phase transformation was previously studied in, e.g., Grinfeld [1982]; Gurtin [1983]; Grinfeld [1990]; Grinfeld [1991]; Fried [1993]; Osmolovsky [2000]. In the current work, the

stability of the reaction front is studied by using the procedure of so-called linear kinetic stability analysis and says that the interface is unstable if its small perturbations grow due to the kinetic equations. The utilized procedure was developed and explored earlier for the case of equilibrium phase interfaces in Eremeev, Freidin, and Sharipova [2003]; Fu and Freidin [2004]; Freidin *et al.* [2006]; Eremeev, Freidin, and Sharipova [2007].

Note that kinetic stability analysis performs not only an energy-based checking of the stability and states the fact of the stability loss, but also gives hints on types (or modes) of instabilities formation and the tendencies of further kinetics of the perturbations. In Phan *et al.* [2001]; Barvosa-Carter and Aziz [2004] the authors numerically considered the growth stability of crystalline silicon from the amorphous phase. Based on a kinetic model from Barvosa-Carter *et al.* [1998], the authors considered the influence of mechanical stresses and growth kinetic anisotropy on the interface roughening. Considering the kinetic model of film growth resulting from deposition and mass transport proposed in Ortiz, Repetto, and Si [1999], the authors in Natsiavas *et al.* [2016] analyzed the influence of the elastic pre-stress on the stability of planar growth asymptotic analysis of a nearly flat interface for the problem of anode-electrolyte interaction. Based on these results, the authors in Hüter *et al.* [2017] considered the stability of the electrode-coating-electrolyte interface depending on the thickness of the thin film interlayer and the magnitude of the elastic pre-stresses.

In Zeeshan and Venkatasubramanian [2017] the stability criteria for electrodeposition at solid-solid interfaces is derived using linear stability analysis assuming that the solids are linearly elastic isotropic materials based on a kinetic model proposed by Monroe and Newman [2004]. It described later cathodic roughening and dendritic growth by taking into account mechanical stresses and their influence on the current exchange densities and potentials at the roughened interface.

Independently of the kinetic stability analysis, the concept of phase transition zones (PTZ) was introduced in Freidin and Chiskis [1994a]; Freidin and Chiskis [1994b]. The PTZ is a zone in a strain space formed by all strains which can exist at the equilibrium interfaces in a given material. The procedure was developed for the case of nonlinear-elastic materials in Freidin and Chiskis [1994a]; Freidin and Chiskis [1994b]; Freidin *et al.* [2006], and then for the case of linear elastic phases in Freidin [1999]; Morozov and Freidin [1998]. Correlation of the results obtained by the kinetic stability analysis and the PTZ approach is discussed in Fu and Freidin [2004]; Eremeev, Freidin, and Sharipova [2003]; Freidin *et al.* [2006]; Eremeev, Freidin, and Sharipova [2007]; Vilchevskaya, Filippov, and Freidin [2013]. In these works, it was shown that instability of phase interface is not observed if the strains at the interface in a body belong to the boundary of the PTZ. Then in the papers Grabovsky and

Truskinovsky [2011]; Grabovsky and Truskinovsky [2013], it was proved that belonging of strains to the external PTZ-boundaries is a necessary stability condition.

In the current work, the kinetic stability analysis and the PTZ procedure are compared for the interfaces at the equilibrium position. However, the PTZ approach cannot be explicitly extrapolated to the case of the chemical interface at the reaction blocking state. The linear stability analysis procedure for phase transformations is extended to the case of a chemical reaction. Note that analytical investigation of the interface stability based on the perturbed kinetic equation is rather complicated, even for simple geometries. Therefore, in this work, a numerical procedure for simulating the reaction front propagation is developed. This procedure is verified with analytical solutions, and special attention is paid to the interfaces approaching the equilibrium position. It is done to check whether the developed numerical methods can reveal physically stable and unstable configurations.

Many numerical simulations of the transformation fronts propagation have been made earlier in problems of different nature. For the case of phase transformations see, e.g., Finite Element Analysis (FEA) applications in Mueller and Gross [1998]; Mueller and Gross [1999]; Gross, Mueller, and Kolling [2002]; Mueller, Gross, and Lupascu [2006]. Stress-field analysis in Li-ion batteries during propagation of the lithiation front propagation was performed using FE in Jia and Li [2015]. A description of the FE simulation of the propagation of a chemical reaction front with the reaction front kinetics controlled by the chemical affinity tensor was implemented in Freidin *et al.* [2016].

In this work, an FEM procedure for numerical simulations of the reaction front propagation is developed based on remeshing algorithms. Utilizing the proposed procedures, the propagation of the transformation fronts is simulated, and the consistency between the numerical and analytical results is checked. The method itself is compared to other numerical approaches to simulate the interface propagation, namely the CutFEM approach. A more detailed discussion about this is given in Chapter 3. The numerical simulations demonstrate how interfaces propagate if the equilibrium positions, found analytically, are stable or unstable. In the case of stable configuration, the interface converges smoothly to the equilibrium position. If the configuration is unstable, the interface also propagates smoothly toward the equilibrium position, but in the vicinity of the equilibrium, when the interface velocity is almost zero, the instabilities become visible and start to grow. This effect may be explained by the competition between global and local kinetics of the interface propagation. It should be emphasized that the existence and propagation of the chemical reaction fronts far from equilibrium is a natural process and stress-induced front retardation and these instabilities, which might

grow considerably, may be the source of further fracture, or another type of failure.

This manuscript is organized as follows. In Chapter 2, an overview of the chemical affinity tensor concept is given. A kinetic stability approach for the analytical stability analysis of interfaces at a chemical equilibrium is formulated. It is done by extending the linear stability analysis procedure developed for phase transformations. In this chapter two simplest problems are studied for linear elastic solid phases of reactants: stability of the plane problem with planar interface in the infinite layer and axially-symmetric plane problem with a cylindrical interface. The influence of the material parameters on the stability of the interface is studied, and, as a result, "stable" and "unstable" sets of parameters are proposed for the following numerical simulations. An FE procedure for numerical simulations of the reaction front propagation based on remeshining algorithms is introduced in Chapter 3. Different approaches to simulating numerically the moving interface are discussed and compared. To check whether the numerical procedure for simulating the reaction front propagation can adequately reveal stable and unstable behavior of the interface, several problems are examined numerically and compared with the analytical solutions and stability predictions from the previous chapter. Also, the remeshing procedure is cross-validated with the other numerical method for simulating the moving interface, namely the CutFEM. Chapter 4 contains theoretical and experimental studies of the IMC growth at the interface between copper pads and tin-based solder alloys. The first part of Chapter 4 reports experimental findings of IMC growth in different microchips during a high-temperature storage test. The growth kinetics is modeled employing a continuum model based on the chemical affinity tensor concept. By combining experiment, theory, and a comparison of experimental data and theoretical predictions, the values of the diffusion coefficient and an estimate for the chemical reaction constants are obtained. Each chapter is finalized by the conclusions section, and the final Chapter 5 gives the general conclusions and the outlook.

2 Chemical reaction front kinetics and stability

2.1 Chemical affinity tensor and general problem statement

Consider a solid body undergoing a chemical transformation caused by a chemical reaction localized at a sharp interface. In general, the equation of a chemical reaction can be written as follows

$$n_- B_- + n_* B_* \to n_+ B_+, \tag{2.1}$$

where n_-, n_* and n_+ are the stoichiometric coefficients, B_-, B_* and B_+ are the species involved in the reaction: initial material, diffusing reactant, and the reaction product, respectively. The reaction between B_- and B_* is localized at the reaction front Γ and is supported by the diffusion of B_* through B_+ as schematically shown in Fig. 2.1. It is assumed that all delivered B_* is consumed by the reaction. The reaction is accompanied by the change of volume at the reaction front. This deformation produces mechanical stresses at the front which in turn may affect the front propagation. Here and further in the text of the manuscript index "$-$" denotes the initial material, "$*$" states for the diffusing constituent, and "$+$" denotes the transformed material, which is the product of the chemical reaction.

The notion of the chemical affinity arises from fundamental results by Gibbs and De Donde (see, e.g., Prigogine and Defay [1954]). It was shown that in the case of a chemical reaction the factor conjugate to the reaction rate ω in the expression of the entropy production P multiplied by temperature T was equal to the combination of the chemical potentials of the reaction constituents:

$$TP = A\omega, \quad A = -\sum n_k M_k \mu_k, \tag{2.2}$$

where μ_k is the chemical potential of the k-th constituent (per unit mass), M_k is the molar mass of k-th constituent, the stoichiometric coefficient n_k contributes to the sum with a positive sign "$+$" if the k-th constituent is produced in the reaction and with a negative sign "$-$" if the k-th constituent

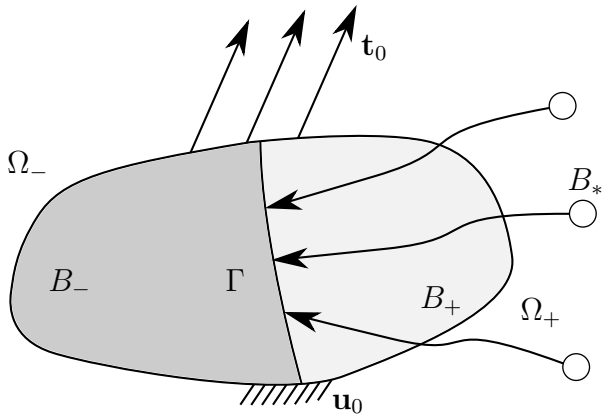

Fig. 2.1: A schematic representation of a localized chemical reaction in solids.

is consumed. For the reaction (2.1) the classical chemical affinity would be

$$A = n_- M_- \mu_- + n_* M_* \mu_* - n_+ M_+ \mu_+, \tag{2.3}$$

where μ_+, μ_- and μ_* are the mass densities of the chemical potentials of the constituents B_+, B_- and B_*, respectively. The factor A was called the chemical affinity of the reaction. Then a kinetic equation in a form of the dependence of the reaction rate on the chemical affinity can be formulated. One of the accepted dependencies (see Glansdorff and Prigogine [1971]) for the reaction rate is the equation

$$\omega = \overline{\omega} \left[1 - \exp\left(-\frac{A}{RT} \right) \right], \tag{2.4}$$

where $\overline{\omega}$ is the so-called partial rate of a direct reaction, which is defined by the concentrations of the reactants, R is the universal gas constant.

The relationships (2.2)–(2.4) were formulated for reactions in systems like gases or liquids for which chemical potentials and, therefore, chemical affinity can be presented as scalar values. The observation that the phase equilibrium and chemical reaction take place not just in a point but at an oriented area element passing through the point, led to the idea of a tensorial nature of the chemical potential and chemical affinity (see the discussion on the tensorial nature of a chemical potential in Grinfeld [1991] and on the tensorial nature of the chemical affinity in Freidin and Vilchevskaya [2020]). One can see here an analogy to the concept of stress. A stress state is determined by a scalar pressure acting in a point in the case of liquids and gases. However, in the case of a solid, instead of pressure, a stress tensor determines a traction acting at the oriented area element passing through a point.

It was shown that the reaction rate is determined by the normal component A_{nn} of the chemical affinity tensor $\mathbf{A}$, see the derivations in Freidin [2013];

Freidin, Vilchevskaya, and Korolev [2014]; Freidin [2015], and the chemical affinity tensor has the same mathematical form as the scalar affinity (2.3) but with tensorial chemical potentials instead of scalar ones. A kinetic equation similar to the equation (2.4) can be taken for the reaction rate ω_n at the area element with the normal $\mathbf{n}$:

$$\omega_n = k_* c \left[1 - \exp\left(-\frac{A_{nn}}{RT}\right)\right], \tag{2.5}$$

where it is taken into account that in the case of the reaction between solid and gaseous constituents $\overline{\omega}$ can be taken in a form $\overline{\omega} = k_* c$ where c is the partial molar concentration of the diffusing reactant. Mechanical stresses affect the reaction rate via the normal component of the affinity tensor. The normal component of the reaction front velocity V_n can be expressed in terms of the reaction rate from the mass balance at the reaction front:

$$V_n = \frac{n_- M_-}{\rho_-}\omega_n. \tag{2.6}$$

In order to handle further analytical calculations and to obtain the unknown parameters of the model, linear elastic solid reactants are considered. In this case the constitutive equations of B_- and B_+ are

$$\begin{aligned} \boldsymbol{\sigma}_- &= \mathbf{C}_- : \boldsymbol{\varepsilon}_-, \\ \boldsymbol{\sigma}_+ &= \mathbf{C}_+ : (\boldsymbol{\varepsilon}_+ - \boldsymbol{\varepsilon}^{\mathrm{tr}}), \end{aligned} \tag{2.7}$$

and the Helmholtz free energies of the solid reactants are represented by

$$\begin{aligned} f_-(\boldsymbol{\varepsilon}) &= \eta_- + \frac{1}{2}\boldsymbol{\varepsilon}_- : \mathbf{C}_- : \boldsymbol{\varepsilon}_-, \\ f_+(\boldsymbol{\varepsilon}) &= \eta_+ + \frac{1}{2}(\boldsymbol{\varepsilon}_+ - \boldsymbol{\varepsilon}^{\mathrm{tr}}) : \mathbf{C}_+ : (\boldsymbol{\varepsilon}_+ - \boldsymbol{\varepsilon}^{\mathrm{tr}}), \end{aligned} \tag{2.8}$$

where $\mathbf{C}_\pm$ are stiffness tensors, $\eta_\pm$ are temperature dependent chemical energies of the reactants $B_\pm$. An isotropic transformation strain tensor can be considered

$$\boldsymbol{\varepsilon}^{\mathrm{tr}} = \varepsilon_{\mathrm{tr}}\mathbf{I}, \tag{2.9}$$

where principal strains $\varepsilon_{\mathrm{tr}}$ are the same at all points of the domain occupied by B_+, and differences related to the deviations of the concentration of the diffusing reactant are neglected.

Two sources of the volume change are considered: deformation due to the chemical transformation itself and deformation due to the diffusion of the diffusing reactant (see, e.g., Freidin [2013]; Müller, Vilchevskaya, and Freidin [2015]; Freidin and Vilchevskaya [2020]). The total deformation can

be estimated as follows. A material B_- is placed on one side of the reaction front and the mix of the materials B_+ and B_* is on the other side. Due to the chemical reaction (2.1), the elementary volume $\mathrm{d}V_- = n_- M_-/\rho_-$ transforms into the volume $\mathrm{d}V_+ = n_+ M_+/\rho_+$ where $\rho_\pm$ are the reference mass densities of solid reactants $B_\pm$. The ratio of these volumes is

$$J_{\mathrm{ch}} = \frac{n_+ M_+/\rho_+}{n_- M_-/\rho_-}. \tag{2.10}$$

The diffusion may produce additional volume $\xi n_* M_*/\rho_*$ inside material B_+, where ρ_* is the reference mass density of the diffusing reactant B_*. The parameter ξ reflects the deformational interaction between the reactants B_* and B_+. In fact, B_- "transforms" into the mix of B_+ and B_* at the interface Γ. Then the ratio of stress-free volumes of materials coexisting across the reaction front is given by

$$J_{\mathrm{tr}} = \frac{n_+ M_+/\rho_+ + \xi n_* M_*/\rho_*}{n_- M_-/\rho_-}. \tag{2.11}$$

The case $\xi = 0$ in (2.11) corresponds to a solid skeleton approach, according to which the diffusion of B_* is not accompanied by volume expansion of B_+. The case $\xi = 1$ corresponds to adding the volumes of B_+ and B_*. The value of the parameter ξ depends on the mechanism of the diffusion of B_* and saturations ability of B_+ with respect to diffusing B_*. The diffusion of B_* through B_+ may occur by a vacancy mechanism involving two counter fluxes: of B_* and of vacancies. Then at the reaction front atoms of B_* take places of these vacancies, and this may also lead to shrinkage of B_+, which corresponds to the case $\xi < 0$.

In the case of small deformations, the transformation strain can be calculated as $\varepsilon_{\mathrm{tr}} = (J_{\mathrm{tr}}^{1/3} - 1)$. To keep strain compatibility conditions (i.e., continuity of a body) across the reaction front in the presence of volume change J_{tr}, additional strains appear and produce internal stresses. These internal stresses together with external loading influence the reaction front velocity.

Further, it is assumed that the chemical potential of the diffusing reactant is given by

$$M_* \mu_* = \eta_* + RT \ln \frac{c}{c_*}, \tag{2.12}$$

where η_* is the chemical energy of the diffusing constituent B_* and c_* is a reference concentration of B_*.

In quasi static approach, neglecting the pressure terms acting on the diffusing constituent (the solid skeleton approach) it can be shown (see, e.g., Freidin, Vilchevskaya, and Korolev [2014]) that from (2.7)–(2.12) the normal component

of the chemical affinity tensor can be expressed as

$$A_{nn} = \frac{n_- M_-}{\rho_-}\chi + n_* RT \ln \frac{c}{c_*}, \tag{2.13}$$

where the contribution of mechanical and chemical energies is presented by

$$\chi = \gamma + \frac{1}{2}\boldsymbol{\sigma}_- : \boldsymbol{\varepsilon}_- - \frac{1}{2}\boldsymbol{\sigma}_+ : (\boldsymbol{\varepsilon}_+ - \boldsymbol{\varepsilon}^{\mathrm{tr}}) + \boldsymbol{\sigma}_\pm : [\![\boldsymbol{\varepsilon}]\!]. \tag{2.14}$$

It should be noted that due to displacement and traction continuity conditions $\boldsymbol{\sigma}_- : [\![\boldsymbol{\varepsilon}]\!] = \boldsymbol{\sigma}_+ : [\![\boldsymbol{\varepsilon}]\!]$. In the expression (2.14)

$$\gamma = \eta_- - \eta_+ + \frac{\rho_-}{n_- M_-} n_* \eta_* \tag{2.15}$$

is the combination of the chemical energies of the reactants and square brackets denote the jump of the value across the reaction front, $[\![\phi]\!] = \phi_+ - \phi_-$.

In the works by Kubanov and Freidin [1988]; Freidin [1989]; Morozov and Freidin [1998]; Freidin [2010] a phase transformation problem was considered and expressions for the jump of the normal component of the Eshelby stress tensor across the interface were derived. These results were used in later work by Freidin, Vilchevskaya, and Korolev [2014]; Freidin [2015] where the expression for the normal component of the chemical affinity tensor was derived through strains at only one side of the chemical interface (e.g., here it is expressed by the strains from the "$-$" side):

$$\begin{aligned} A_{nn} = \frac{n_- M_-}{\rho_-}\Big(\gamma - \frac{1}{2}\,\boldsymbol{\varepsilon}^{\mathrm{tr}} \vdots \mathbf{C}_+ : \boldsymbol{\varepsilon}^{\mathrm{tr}} - \frac{1}{2}\,\boldsymbol{\varepsilon}_- \vdots [\![\mathbf{C}]\!] : \boldsymbol{\varepsilon}_- + \\ \boldsymbol{\varepsilon}_- \vdots \mathbf{C}_+ : \boldsymbol{\varepsilon}^{\mathrm{tr}} + \frac{1}{2}\,\mathbf{q}_- \vdots \mathbf{K}_+(\mathbf{n}) : \mathbf{q}_-\Big) + n_* RT \ln \frac{c}{c_*}, \end{aligned} \tag{2.16}$$

where

$$\begin{gathered} \mathbf{q}_\pm = [\![\mathbf{C}]\!] \vdots \boldsymbol{\varepsilon}_\pm - \mathbf{C}_+ : \boldsymbol{\varepsilon}^{\mathrm{tr}}, \\ \mathbf{K}_\mp(\mathbf{n}) = \{\mathbf{n}\,\mathbf{G}_\mp(\mathbf{n})\mathbf{n}\}^s, \qquad \mathbf{G}_\mp(\mathbf{n}) = (\mathbf{n}\cdot\mathbf{C}_\mp\cdot\mathbf{n})^{-1}. \end{gathered} \tag{2.17}$$

In (2.17) the upper and lower subscripts "$+$" and "$-$" in the relationships correspond to each other, $\mathbf{G}(\mathbf{n})$ is the Fourier transform of the Green tensor (the inverse of the acoustic tensor), and s means symmetrization: $K_{ijkl} = n_{(i}G_{j)(k}n_{l)}$. If the tensor $[\![\mathbf{C}]\!]^{-1}$ exists, then the mechanical contribution in the expression for A_{nn} can be rewritten in a similar manner as it was shown in Kubanov and

Freidin [1988] for the case of phase transformations:

$$A_{nn} = \frac{n_- M_-}{\rho_-}\left(\gamma_* - \frac{1}{2}\,\mathbf{q}_- : \left(\llbracket \mathbf{C} \rrbracket^{-1} - \mathbf{K}_+(\mathbf{n})\right) : \mathbf{q}_-\right) + n_* RT \ln\frac{c}{c_*}, \qquad \text{where} \qquad \gamma_* = \gamma - \frac{1}{2}\,\boldsymbol{\varepsilon}^{\mathrm{tr}} : \llbracket \mathbf{B} \rrbracket^{-1} : \boldsymbol{\varepsilon}^{\mathrm{tr}}, \qquad \mathbf{B}_\pm = \mathbf{C}_\pm^{-1}. \tag{2.18}$$

One should note that the latter expression is suitable for analytical solutions and for the following linear stability analysis. However, expressions (2.13)–(2.14) should be utilized in the numerical simulations.

The mechanical stresses $\boldsymbol{\sigma}$ and the concentration c of the diffusing reactant B_* can be found from the solution of the system of equations which include:

(i) Mechanical equilibrium equations:

$$\nabla \cdot \boldsymbol{\sigma} = \mathbf{0} \tag{2.19}$$

with boundary and interface conditions:

$$\begin{aligned} \mathbf{u}|_{\Omega_1} = \mathbf{u}_0, \quad \boldsymbol{\sigma}\cdot\mathbf{n}|_{\Omega_2} = \mathbf{t}_0, \\ \llbracket \mathbf{u} \rrbracket|_\Gamma = \mathbf{0}, \quad \llbracket \boldsymbol{\sigma} \rrbracket \cdot \mathbf{n}|_\Gamma = \mathbf{0}\ , \end{aligned} \tag{2.20}$$

where $\mathbf{u}_0$ and $\mathbf{t}_0$ are the given displacement and traction vectors at the corresponding outer boundaries Ω_1 and Ω_2 of the body;

(ii)The constitutive equations (2.7) of the solid reactants;

(iii) The diffusion equation defined over the domain occupied by the material B_+

$$\Delta \mathrm{c} = 0\ , \tag{2.21}$$

with the boundary and interface conditions:

$$\begin{aligned} D\mathbf{n}\cdot\nabla c - a(c_* - c) = 0 \quad \text{at} \quad \Omega_+, \\ D\mathbf{n}\cdot\nabla c + n_*\omega_n = 0 \quad \text{at} \quad \Gamma, \end{aligned} \tag{2.22}$$

where D is the diffusivity, a is the mass transfer coefficient, or the dissolution constant (Xin *et al.* [2003]; Lin *et al.* [2017]) at the outer boundary of the body, $\mathbf{n}$ is the normal directed outward the domain B_+. For the sake of simplicity, the steady-state diffusion is considered with stationary diffusion equation. One should note, that if the characteristic time of the reaction is much smaller than the relative time of the diffusion, then the chemical reaction is diffusion controlled. For this case a non-stationary diffusion equation should be utilized.

The first boundary condition in (2.22) defines the flux of B_* through the

external boundary in relation with the solubility of B_* in B_+ and means that the supply of B_* through the boundary stops if the saturation c_* is reached. On the other hand, the Dirichlet boundary condition $c = c_*$ can be prescribed at Γ_+, however, being less physically reasonable comparing to Robin boundary condition $(2.22)_1$.

The second boundary conditions in (2.22) follows from the mass balance between the supplied and consumed B_* at the reaction front and the assumption that the velocity of diffusing particles is much greater than the velocity of the reaction front. The reaction rate ω_n in the boundary condition at the chemical reaction front couples the elasticity and the diffusion problems. One should note that starting from equation (2.22), the coefficient n_* is assumed to be equal to one. This can be done by normalizing all of the stoichiometric coefficients in (2.1), i.e., $n_- \to n_-/n_*, n_+ \to n_+/n_*$. This also leads to avoiding a nonlinearity of the boundary condition at the moving interface $(2.22)_2$ when it is rewritten in terms of concentrations (see, e.g., Freidin *et al.* [2016]).

(iv) To close the system of equations one has to add the kinetic equation (2.5) for ω_n which defines the reaction front velocity via (2.6) with the dependence of A_{nn} on the stresses and concentration given by (2.13)–(2.15).

The reaction rate can be expressed in terms of the equilibrium concentration c_{eq} as shown, for instance, in Freidin, Vilchevskaya, and Korolev [2014]:

$$\omega = k_* \left(c - c_{\text{eq}}\right), \quad \text{where} \quad c_{\text{eq}} = c_* \exp\left(-\frac{n_- M_-}{\rho_-}\frac{\chi}{RT}\right),$$

where χ is taken from (2.14), or can be rewritten as

$$\begin{aligned}\chi =& \gamma(T) - \frac{1}{2}\boldsymbol{\varepsilon}^{\text{tr}} : \mathbf{C}_+ : \boldsymbol{\varepsilon}^{\text{tr}} - \frac{1}{2}\boldsymbol{\varepsilon}_- : [\![\mathbf{C}]\!] : \boldsymbol{\varepsilon}_- + \\ & \boldsymbol{\varepsilon}_- : \mathbf{C}_+ : \boldsymbol{\varepsilon}^{\text{tr}} + \frac{1}{2}\mathbf{q}_- : \mathbf{K}_+(\mathbf{n}) : \mathbf{q}_- \\ =& \gamma_* - \frac{1}{2}\,\mathbf{q}_- : \left([\![\mathbf{C}]\!]^{-1} - \mathbf{K}_+\left(\mathbf{n}\right)\right) : \mathbf{q}_-,\end{aligned} \tag{2.23}$$

similarly to (2.16) and (2.18).

It should be noted that if the concentration of the diffusing constituent at the reaction front is equal to c_{eq} then the driving force is equal to zero and the thermodynamic equilibrium is reached.

2.2 On stability of a chemical interface

A special case when the driving force is equal to zero for all points of the interface is considered as an equilibrium configuration. However, even if the interface velocity is zero, an additional stability analysis of the "reaction blocking" state is required. The kinetic equation and the behavior of the perturbed solution on the perturbed interface is analyzed in this section. To this end the procedure described by Eremeev, Freidin, and Sharipova [2007] is followed, where the authors analyzed the stability of the interface between two phases at the mechanical equilibrium during a phase transformation. In the next sections it will be shown that there are certain mathematical similarities between chemical and phase transformation regarding the linear stability analysis. Therefore phase transformation front kinetics and stability is studied as well as chemical interface stability.

It is important to notice that within perturbation approach the configuration is considered as stable if the equilibrium chemical reaction front with a normal parallel to the tensile or compressive deformation is stable. In other words, configurations, which tend to change their microstructure (e.g., optimal laminates discussed in Antimonov, Cherkaev, and Freidin [2016]) are considered as unstable.

The main idea behind perturbing the interface is that if the equilibrium position is stable then the perturbed configuration will return to its unperturbed state. As mentioned above, the equilibrium position of the interface is reached when the thermodynamic force is equal to zero in all points of the interface. Linear stability analysis considers small perturbations of the displacements and position of the interface. Consequently, the displacement and the interface position in the perturbed state are written as follows:

$$\mathbf{u} = \mathbf{u}^0 + \mathbf{w}, \quad \mathbf{R} = \mathbf{R}^0 + \eta \mathbf{n}^0, \tag{2.24}$$

where $\mathbf{u}^0$ and $\mathbf{R}^0$ correspond to the equilibrium displacements and interface position, $\mathbf{w}$ and η are the perturbations, $\mathbf{n}^0$ is a normal to the unperturbed interface (Fig. 2.2). Linearization of the Boundary Value Problem (BVP) defined by (2.19)–(2.20) using the constitutive equation (2.7) and the additional thermodynamic condition $\chi = 0$ leads to the following set of equations and boundary conditions for $\mathbf{w}$ and η which were obtained in Eremeev, Freidin, and Sharipova [2003]; Eremeev, Freidin, and Sharipova [2007]. In the domains $V_\pm$ the differential equation and the boundary conditions take the form:

$$\begin{gathered} \nabla \cdot \boldsymbol{\sigma}_\pm(\mathbf{w}) = \mathbf{0}, \qquad \boldsymbol{\sigma}_\pm(\mathbf{w}) = \mathbf{C}_\pm : \nabla \mathbf{w}, \\ \mathbf{w}|_{\Omega_1} = \mathbf{0}, \qquad \mathbf{n} \cdot \boldsymbol{\sigma}_+(\mathbf{w})|_{\Omega_2} = \mathbf{0}. \end{gathered} \tag{2.25}$$

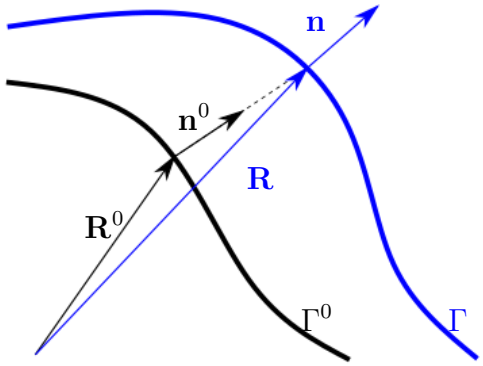

Fig. 2.2: Unperturbed and perturbed interfaces Γ^0 and Γ.

Displacement and traction continuity conditions at the interface are

$$[\![\mathbf{w}]\!] = -\eta[\![\mathbf{n}\cdot\nabla\mathbf{u}^0]\!], \qquad \mathbf{n}\cdot[\![\boldsymbol{\sigma}(\mathbf{w})]\!] = \nabla\eta\cdot[\![\boldsymbol{\sigma}^0]\!] - \eta\mathbf{n}\cdot[\![\mathbf{n}\cdot\nabla\boldsymbol{\sigma}^0]\!]. \tag{2.26}$$

Analogously to the perturbed displacements, the perturbed solution for the diffusion problem consists of the original solution c^0 and an additional small perturbation term:

$$c = c^0 + s. \tag{2.27}$$

A linearization of the boundary value problem defined by (2.21)–(2.22) provides the following set of equations for the diffusion perturbation value s, which are coupled with the displacement perturbation $\mathbf{w}$ by the chemical reaction rate

$$\begin{aligned} \Delta s &= 0, \\ D\mathbf{n}^0\cdot\nabla s + n_*\delta\omega(\mathbf{w},s) &= 0 \quad \text{at the reaction front interface,} \\ D\mathbf{n}^0\cdot\nabla s + \alpha s &= 0 \quad \text{at the reactant supply surface.} \end{aligned} \tag{2.28}$$

In the following sections a detailed derivation of the boundary and interface conditions is given for the perturbed boundary value problem written in (2.25)–(2.28). For this purpose a variation of the normal vector, jump across the interface conditions, the driving force and the chemical reaction rate are derived.

2.2.1 Variation of the normal

If q_1, q_2 are the curvilinear coordinates at the interface, then unperturbed and perturbed interfaces are presented by the vectorial functions $\mathbf{R} = \mathbf{R}^0_\Gamma(q_1,q_2)$ and $\mathbf{R} = \mathbf{R}_\Gamma(q_1,q_2)$, respectively. Then the basis vectors on the unperturbed

and perturbed interfaces are defined by

$$\mathbf{R}^0_\alpha = \frac{\partial \mathbf{R}^0_\Gamma}{\partial q^\alpha}, \qquad \mathbf{R}_\alpha = \mathbf{R}^0_\alpha + \frac{\partial(\eta \mathbf{n})}{\partial q^\alpha}, \qquad \alpha = 1, 2. \tag{2.29}$$

Due to the perturbation, the normal to the interface becomes

$$\mathbf{n} = \mathbf{n}^0 + \delta\mathbf{n}. \tag{2.30}$$

Then

$$\mathbf{n} \cdot \mathbf{R}_\alpha = 0 = (\mathbf{n}_0 + \delta\mathbf{n}) \cdot \mathbf{R}^0_\alpha + (\mathbf{n}_0 + \delta\mathbf{n}) \cdot \left(\frac{\partial \mathbf{n}^0}{\partial q^\alpha} \eta + \mathbf{n}^0 \frac{\partial \eta}{\partial q^\alpha} \right). \tag{2.31}$$

Neglecting second order terms and taking into account relationships $\mathbf{n}^0 \cdot \delta\mathbf{n} = 0$ and $\mathbf{n}^0 \cdot \dfrac{\partial \mathbf{n}^0}{\partial q^\alpha} = 0$, the following expression can be derived

$$\delta\mathbf{n} \cdot \mathbf{R}^0_\alpha = -\frac{\partial \eta}{\partial q^\alpha}. \tag{2.32}$$

Since $\delta\mathbf{n} \cdot \mathbf{R}^0_\alpha = \delta N_\alpha$ is the covariant component of the vector $\delta\mathbf{n}$ in the dual basis $\mathbf{R}^{\alpha 0}$, the above equality takes the vectorial form

$$\delta\mathbf{n} = -\widetilde{\nabla}\eta, \qquad \text{where} \qquad \widetilde{\nabla} = \mathbf{R}^{\alpha 0} \frac{\partial}{\partial q^\alpha} \tag{2.33}$$

stands for a 2D nabla-operator in q_1-q_2 coordinate system.

2.2.2 Variation of a jump across the interface

To formulate displacement and traction continuity conditions across the perturbed interface, a general expressions of the variation of a jump due to variation of the interface position and displacement field is derived.

Given displacement field $\mathbf{u}$, consider a function

$$\phi(\mathbf{R} \,|\, \mathbf{u}) = \begin{cases} \phi_-(\mathbf{R} \,|\, \mathbf{u}), & \mathbf{R} \in v_- \\ \phi_+(\mathbf{R} \,|\, \mathbf{u}), & \mathbf{R} \in v_+ \end{cases}$$

where the functions $\phi_-(\mathbf{R} \,|\, \mathbf{u})$ and $\phi_+(\mathbf{R} \,|\, \mathbf{u})$ are smooth enough in domains v_- and v_+. Denote by $\phi_\pm(\mathbf{R}_\Gamma \,|\, \mathbf{u})$ and $\nabla\phi_\pm(\mathbf{R}_\Gamma \,|\, \mathbf{u})$ the limit values of ϕ and $\nabla\phi$ at the corresponding sides of the interface. Referring to the Figure 2.2, consider two configurations: (i) with the unperturbed interface $\mathbf{R}^0_\Gamma$ at displacement field $\mathbf{u}^0$ and (ii) with the perturbed interface $\mathbf{R}_\Gamma = \mathbf{R}^0_\Gamma + \delta\mathbf{R}_\Gamma$ at perturbed displacement $\mathbf{u} = \mathbf{u}^0 + \mathbf{w}$. Then the jumps of $\phi\,(\mathbf{R}_\Gamma, \mathbf{u})$ across perturbed

interface, the jump of $\phi\left(\mathbf{R}_\Gamma^0, \mathbf{u}^0\right)$ across unperturbed interface and the jump of the variations $\delta_u\phi\left(\mathbf{R}_\Gamma^0 \,|\, \mathbf{u}^0\right)$ of ϕ due to displacement perturbations are related as

$$[\![\phi\left(\mathbf{R}_\Gamma \,|\, \mathbf{u}\right)]\!] = [\![\phi\left(\mathbf{R}_\Gamma^0 \,|\, \mathbf{u}^0\right)]\!] + [\![\delta_u\phi\left(\mathbf{R}_\Gamma^0 \,|\, \mathbf{u}^0\right)]\!] + \delta\mathbf{R}_\Gamma \cdot [\![\nabla\phi\left(\mathbf{R}_\Gamma^0 \,|\, \mathbf{u}^0\right)]\!]. \quad (2.34)$$

To prove (2.34) note that the functions $\phi_+(\mathbf{R} \,|\, \mathbf{u})$ and $\phi_-(\mathbf{R} \,|\, \mathbf{u})$ are defined only in the domains v_+ and v_-, respectively, and the interface position is given by $\mathbf{R}_\Gamma^0$ if the displacement is $\mathbf{u}^0$, and by $\mathbf{R}_\Gamma$ if the displacement is $\mathbf{u}$. Therefore ϕ_+ is defined in points $\mathbf{R}_\Gamma^0$ and $\mathbf{R}_\Gamma$ at displacement $\mathbf{u}$ and in points $\mathbf{R}_\Gamma^0$ at both displacements $\mathbf{u}^0$ and $\mathbf{u}$. Then, neglecting second (and higher) order terms with respect to perturbations one can obtain the following expressions

$$\begin{aligned} \phi_+\left(\mathbf{R}_\Gamma \,|\, \mathbf{u}\right) &= \phi_+\left(\mathbf{R}_\Gamma^0, \mathbf{u}\right) + \delta\mathbf{R}_\Gamma \cdot \nabla\phi_+\left(\mathbf{R}_\Gamma^0 \,|\, \mathbf{u}\right) \\ \phi_+\left(\mathbf{R}_\Gamma^0 \,|\, \mathbf{u}\right) &= \phi_+\left(\mathbf{R}_\Gamma^0 \,|\, \mathbf{u}^0\right) + \delta_u\phi_+\left(\mathbf{R}_\Gamma^0 \,|\, \mathbf{u}^0\right) \end{aligned} \quad (2.35)$$

and, thus, with the same accuracy

$$\phi_+\left(\mathbf{R}_\Gamma \,|\, \mathbf{u}\right) = \phi_+\left(\mathbf{R}_\Gamma^0 \,|\, \mathbf{u}^0\right) + \delta_u\phi_+\left(\mathbf{R}_\Gamma^0 \,|\, \mathbf{u}^0\right) + \delta\mathbf{R}_\Gamma \cdot \nabla\phi_+\left(\mathbf{R}_\Gamma^0 \,|\, \mathbf{u}^0\right). \quad (2.36)$$

Analogously, since function ϕ_- is defined in points $\mathbf{R}_\Gamma$ at displacement $\mathbf{u}$ and at displacement $\mathbf{u}_0$ and in points $\mathbf{R}_\Gamma$ and $\mathbf{R}_\Gamma^0$ at displacement $\mathbf{u}^0$, one can write

$$\phi_-\left(\mathbf{R}_\Gamma \,|\, \mathbf{u}\right) = \phi_-\left(\mathbf{R}_\Gamma^0 \,|\, \mathbf{u}^0\right) + \delta_u\phi_-\left(\mathbf{R}_\Gamma^0 \,|\, \mathbf{u}^0\right) + \delta\mathbf{R}_\Gamma \cdot \nabla\phi_-\left(\mathbf{R}_\Gamma^0 \,|\, \mathbf{u}^0\right). \quad (2.37)$$

Subtracting (2.37) from (2.36) gives the formula (2.34).

If quantity ϕ denotes the displacement vector field $\mathbf{u}$ then $\delta_u\phi$ denotes the displacement perturbation $\mathbf{w}$. Since, due to displacement continuity, $[\![\mathbf{u}^0(\mathbf{R}_\Gamma^0)]\!] = [\![\mathbf{u}(\mathbf{R}_\Gamma)]\!] = 0$, from (2.34) it follows that

$$[\![\mathbf{w}]\!] + \delta\mathbf{R}_\Gamma \cdot [\![\nabla\mathbf{u}^0]\!] = 0. \quad (2.38)$$

From the displacement continuity it follows that $[\![\nabla\mathbf{u}^0]\!] = \mathbf{n}^0\mathbf{a}$, where $\mathbf{a} = \mathbf{n}^0 \cdot [\![\nabla\mathbf{u}^0]\!]$ is the amplitude of jump. Then only normal component η of $\delta\mathbf{R}_\Gamma$ remains in the displacement continuity condition that becomes so-called second order compatibility condition $(2.26)_1$:

$$[\![\mathbf{w}]\!] + \eta\mathbf{n}^0 \cdot [\![\nabla\mathbf{u}^0]\!] = 0. \quad (2.39)$$

Further, without loss of generality, we assume that $\delta\mathbf{R}_\Gamma = \eta\mathbf{n}^0$.

For the jump of stresses (2.34) can be rewritten as follows

$$[\![\boldsymbol{\sigma}\left(\mathbf{R}_\Gamma, \mathbf{u}\right)]\!] = [\![\boldsymbol{\sigma}\left(\mathbf{R}_\Gamma^0, \mathbf{u}^0\right)]\!] + [\![\boldsymbol{\sigma}\left(\mathbf{R}_\Gamma^0, \mathbf{w}\right)]\!] + \eta\mathbf{n}^0 \cdot [\![\nabla\boldsymbol{\sigma}\left(\mathbf{R}_\Gamma^0, \mathbf{u}^0\right)]\!] \quad (2.40)$$

where $\boldsymbol{\sigma}\left(\mathbf{R}, \mathbf{u}^0\right)$ and $\boldsymbol{\sigma}_\pm(\mathbf{R}, \mathbf{u})$ are given by (2.7) with strain tensors $\boldsymbol{\varepsilon}^0 = \nabla\mathbf{u}^0$ and $\boldsymbol{\varepsilon} = \nabla\mathbf{u}$, respectively, $\boldsymbol{\sigma}_\pm(\mathbf{w}) = \mathbf{C}_\pm : \nabla\mathbf{w}$. Then at the perturbed interface

$$\begin{aligned}\mathbf{n} \cdot [\![\boldsymbol{\sigma}\left(\mathbf{R}_\Gamma, \mathbf{u}\right)]\!] = (\mathbf{n}^0 + \delta\mathbf{n}) \cdot \Big([\![\boldsymbol{\sigma}\left(\mathbf{R}_\Gamma^0, \mathbf{u}^0\right)]\!] + [\![\boldsymbol{\sigma}\left(\mathbf{R}_\Gamma^0, \mathbf{w}\right)]\!] + \\ \eta\mathbf{n}^0 \cdot [\![\nabla\boldsymbol{\sigma}\left(\mathbf{R}_\Gamma^0, \mathbf{u}^0\right)]\!]\Big) = \mathbf{0}.\end{aligned} \quad (2.41)$$

Taking into account that $\mathbf{n}^0 \cdot [\![\boldsymbol{\sigma}\left(\mathbf{R}_\Gamma^0, \mathbf{u}^0\right)]\!] = 0$, using the formula (2.33) for $\delta\mathbf{n}$ and neglecting second order terms we come to the final expression $(2.26)_2$ for the linearized traction continuity condition at the perturbed interface

$$\mathbf{n}^0 \cdot [\![\boldsymbol{\sigma}(\mathbf{w})]\!] = \widetilde{\nabla}\eta \cdot [\![\boldsymbol{\sigma}^0]\!] - \eta\mathbf{n}^0 \cdot [\![\nabla\boldsymbol{\sigma}^0]\!] \cdot \mathbf{n}^0, \quad (2.42)$$

where $\boldsymbol{\sigma}_\pm^0 = \boldsymbol{\sigma}_\pm\left(\mathbf{R}_\Gamma^0, \mathbf{u}^0\right)$ and $\boldsymbol{\sigma}_\pm(\mathbf{w}) = \boldsymbol{\sigma}_\pm\left(\mathbf{R}_\Gamma^0, \mathbf{w}\right)$.

2.2.3 Linearized kinetic equation for perturbed phase interfaces

By (2.18), the driving forces at the perturbed and unperturbed interface are

$$\begin{aligned}\chi|_\Gamma &= \gamma_* - \frac{1}{2}\left(\mathbf{q}_-^0 + \delta\mathbf{q}_-\right) : \left([\![\mathbf{C}]\!]^{-1} - \mathbf{K}_+(\mathbf{n}^0 + \delta\mathbf{n})\right) : \left(\mathbf{q}_-^0 + \delta\mathbf{q}_-\right), \\ \chi|_{\Gamma^0} &= \gamma_* - \frac{1}{2}\mathbf{q}_-^0 : \left([\![\mathbf{C}]\!]^{-1} - \mathbf{K}_+(\mathbf{n}^0)\right) : \mathbf{q}_-^0,\end{aligned} \quad (2.43)$$

where $\mathbf{q}_-^0 = [\![\mathbf{C}]\!] : \boldsymbol{\varepsilon}_-^0 - \mathbf{C}_+ : \boldsymbol{\varepsilon}^{\mathrm{ch}}$, $\delta\mathbf{q}_-$ is calculated by Eq. (2.37):

$$\delta\mathbf{q}_- = \delta_u\mathbf{q}_-^0 + \eta\mathbf{n}^0 \cdot \nabla\mathbf{q}_-^0 = [\![\mathbf{C}]\!] : \nabla\mathbf{w}_- + \eta\mathbf{n}^0 \cdot \left(\nabla\boldsymbol{\varepsilon}_-^0 : [\![\mathbf{C}]\!]\right). \quad (2.44)$$

Then, with $\mathbf{K}_+(\mathbf{n}^0 + \delta\mathbf{n}) = \mathbf{K}(\mathbf{n}^0) + \delta\mathbf{K}(\mathbf{n}_0)$, the expression of the driving force variation takes the form

$$\delta\chi = -\mathbf{q}_-^0 : \left([\![\mathbf{C}]\!]^{-1} - \mathbf{K}_+(\mathbf{n}^0)\right) : \delta\mathbf{q}_- + \frac{1}{2}\mathbf{q}_-^0 : \delta\mathbf{K}(\mathbf{n}^0) : \mathbf{q}_-^0. \quad (2.45)$$

In the case when the normal $\mathbf{n}^0$ is an eigenvector of $\mathbf{q}_-^0$ and material "+" is isotropic, the last term in (2.45) is equal to zero. Indeed, the fourth rank tensor $\mathbf{K}_+(\mathbf{n})$ in the case of an isotropic material can be presented with the

use of in special tensorial basis (see Kunin [1983]) as

$$\mathbf{K}_+(\mathbf{n}) = \frac{1}{\mu_+}\left(\mathbf{E}^5 - \varkappa_+\mathbf{E}^6\right), \tag{2.46}$$

where

$$\mathbf{E}^5 = (\mathbf{n}\mathbf{e}_k\mathbf{e}_k\mathbf{n})^s = \frac{1}{4}\left(\mathbf{n}\mathbf{e}_k\mathbf{e}_k\mathbf{n} + \mathbf{e}_k\mathbf{n}\mathbf{e}_k\mathbf{n} + \mathbf{n}\mathbf{e}_k\mathbf{n}\mathbf{e}_k + \mathbf{e}_k\mathbf{n}\mathbf{n}\mathbf{e}_k\right),$$
$$\mathbf{E}^6 = \mathbf{nnnn},$$
$$\varkappa_+ = \frac{\lambda_+ + \mu_+}{\lambda_+ + 2\mu_+} = \frac{1}{2(1-\nu_+)},$$

upper script s denotes here the symmetrization of a fourth rank tensor with respect to permutation of indices within the first and second pairs, vectors $\mathbf{e}_k$ $(k = 1, 2, 3)$ form an orthonormal basis, and $\mathbf{e}_k\mathbf{e}_k$ is a second rank unit tensor. Note that $\mathbf{E}^5$ is also symmetric with respect to the permutation of the pairs of indices. The variation of $\mathbf{E}^5$ equals to

$$\delta\mathbf{E}^5 = \frac{1}{4}\left((\delta\mathbf{n})\mathbf{e}_k\mathbf{e}_k\mathbf{n} + \mathbf{n}\mathbf{e}_k\mathbf{e}_k\delta\mathbf{n} + \mathbf{e}_k(\delta\mathbf{n})\mathbf{e}_k\mathbf{n} + \mathbf{e}_k\mathbf{n}\mathbf{e}_k\delta\mathbf{n} + \right.$$
$$\left. + (\delta\mathbf{n})\mathbf{e}_k\mathbf{n}\mathbf{e}_k + \mathbf{n}\mathbf{e}_k(\delta\mathbf{n})\mathbf{e}_k + \mathbf{e}_k(\delta\mathbf{n})\mathbf{n}\mathbf{e}_k + \mathbf{e}_k\mathbf{n}(\delta\mathbf{n})\mathbf{e}_k\right)$$

Then, since $\mathbf{n}\cdot\delta\mathbf{n} = 0$, it is clear that if $\mathbf{n}$ is an eigenvector of $\mathbf{q}$,

$$\mathbf{q} : \delta\mathbf{E}^5 : \mathbf{q} = 0 \tag{2.47}$$

and, analogously, $\mathbf{q} : \delta\mathbf{E}^6 : \mathbf{q} = 0$, and finally

$$\mathbf{q} : \delta\mathbf{K} : \mathbf{q} = 0.$$

By (2.44) and (2.45), with this additional assumption about the eigenvector of $\mathbf{q}^0$, the expression for the variation of the driving force takes the form

$$\begin{aligned}\delta\chi = -\mathbf{q}^0_- : \left(\llbracket\mathbf{C}\rrbracket^{-1} - \mathbf{K}_+(\mathbf{n}_0)\right) : \llbracket\mathbf{C}\rrbracket : \boldsymbol{\varepsilon}_-(\mathbf{w}_-) - \\ \eta\,\mathbf{q}^0_- : \left(\llbracket\mathbf{C}\rrbracket^{-1} - \mathbf{K}_+(\mathbf{n}_0)\right) : \left(\mathbf{n}^0\cdot\left(\nabla\boldsymbol{\varepsilon}^0_- : \llbracket\mathbf{C}\rrbracket\right)\right).\end{aligned} \tag{2.48}$$

The variation can also be expressed in terms of strains on the "+" side of the interface:

$$\begin{aligned}\delta\chi = -\mathbf{q}^0_+ : \left(\llbracket\mathbf{C}\rrbracket^{-1} + \mathbf{K}_-(\mathbf{n}_0)\right) : \llbracket\mathbf{C}\rrbracket : \boldsymbol{\varepsilon}_+(\mathbf{w}_+) - \\ \eta\,\mathbf{q}^0_+ : \left(\llbracket\mathbf{C}\rrbracket^{-1} + \mathbf{K}_-(\mathbf{n}_0)\right) : \left(\mathbf{n}^0\cdot\left(\nabla\boldsymbol{\varepsilon}^0_+ : \llbracket\mathbf{C}\rrbracket\right)\right).\end{aligned} \tag{2.49}$$

Note that the last terms in Eqs. (2.48) and (2.49) are zero if the normal derivatives $\mathbf{n}^0 \cdot \nabla \boldsymbol{\varepsilon}^0_{\mp}$ of the strains $\boldsymbol{\varepsilon}^0_{\mp}$ are zero. This is, for example, the case of piece-wise homogeneous two phase deformations with plane interfaces, or in the case of spherically or axially symmetric two-phase deformations in a solid cylinder or sphere when the strain is uniform in the inner domain. In the last case one can take representation (2.48) or (2.49), depending on what the phase, "$-$" or "$+$", occupies the inner domain.

The normal components V_n and V_n^0 of the velocities $\mathbf{V}$ and $\mathbf{V}^0$ of the perturbed and unperturbed interfaces with an accuracy of the second order of smallness are related as

$$V_n = \frac{\partial \mathbf{R}_\Gamma}{\partial t} \cdot \mathbf{n} = \frac{\partial \left(\mathbf{R}^0_\Gamma + \eta \mathbf{n}^0\right)}{\partial t} \cdot (\mathbf{n}^0 + \delta \mathbf{n}) = V_n^0 + \mathbf{V}^0 \cdot \delta \mathbf{n} + \frac{\partial \eta}{\partial t}. \tag{2.50}$$

Since only normal component of the interface velocity is essential, one may accept $\mathbf{V}^0 = V_n^0 \mathbf{n}^0$. Then

$$\delta V_n = V_n - V_n^0 = \frac{\mathrm{d}\eta}{\mathrm{d}t}. \tag{2.51}$$

The kinetic equation for the phase transformation front is $V_n^{\mathrm{ph}} = \kappa_{\mathrm{ph}} \chi$. Then from (2.48), (2.49) and (2.51) it follows that perturbations evolve according to the kinetic equation that can be presented in the following forms:

$$\begin{aligned} \frac{1}{\kappa_{\mathrm{ph}}} \frac{\mathrm{d}\eta}{\mathrm{d}t} = &-\mathbf{q}^0_- : \Big([\![\mathbf{C}]\!]^{-1} - \mathbf{K}_+(\mathbf{n}_0) \Big) : [\![\mathbf{C}]\!] : \boldsymbol{\varepsilon}_-(\mathbf{w}_-) - \\ &\eta\, \mathbf{q}^0_- : \Big([\![\mathbf{C}]\!]^{-1} - \mathbf{K}_+(\mathbf{n}_0) \Big) : \Big(\mathbf{n}^0 \cdot \Big(\nabla \boldsymbol{\varepsilon}^0_- : [\![\mathbf{C}]\!] \Big) \Big) \\ = &\ \mathbf{q}^0_+ : \Big([\![\mathbf{C}]\!]^{-1} + \mathbf{K}_-(\mathbf{n}_0) \Big) : [\![\mathbf{C}]\!] : \boldsymbol{\varepsilon}_+(\mathbf{w}_+) \\ &-\eta\, \mathbf{q}^0_+ : \Big([\![\mathbf{C}]\!]^{-1} + \mathbf{K}_-(\mathbf{n}_0) \Big) : \Big(\mathbf{n}^0 \cdot \Big(\nabla \boldsymbol{\varepsilon}^0_+ : [\![\mathbf{C}]\!] \Big) \Big). \end{aligned} \tag{2.52}$$

2.2.4 Linearized kinetic equation for perturbed chemical interfaces

The variation of thr reaction rate $\delta\omega$ in (2.28) depends on the displacements perturbation vector $\mathbf{w}$ and the diffusion perturbation s. Keeping in mind that $A_{nn} \approx 0$ and $c_* = c^0 = c_{\mathrm{eq}}$ near equilibrium (for the details we refer to Freidin, Vilchevskaya, and Korolev [2014]), the reaction rate can be expressed by using

Eq. (2.5):

$$\begin{aligned}\omega(\mathbf{w},s) &= k_* c\left(1-\exp\left(-\frac{A_{nn}(\mathbf{w},s)}{RT}\right)\right) = k_*(c^0+s)\frac{A_{nn}(\mathbf{w},s)}{RT}\\ &= \frac{k_* c^0}{RT}\left(\frac{n_- M_-}{\rho_-}\delta\chi + RT\ln\left(\frac{c^0+s}{c_*}\right)\right)+\cdots\\ &= \frac{k_* c^0}{RT}\left(\frac{n_- M_-}{\rho_-}\delta\chi + RT\frac{s}{c_*}\right)+\cdots,\end{aligned} \tag{2.53}$$

where $\delta\chi$ is a variation of the mechanical part of the chemical affinity tensor, which has the same form as the variation of the driving force in the case of phase transformations (2.48). The variation of the diffusion related logarithmic term in the expression for A_{nn} can be obtained as follows

$$\delta\left(\ln\frac{c(\mathbf{R})}{c_*}\right) = \ln\frac{c}{c_*}\bigg|_{\mathbf{R}^0} + \frac{\delta c}{c}\bigg|_{\mathbf{R}^0} + \eta\mathbf{n}^0\cdot\nabla\ln\frac{c}{c_*}\bigg|_{\mathbf{R}^0}+\cdots. \tag{2.54}$$

At the thermodynamical equilibrium the concentration of the diffusing component in the reactant material is constant (as can be seen from the solution in Freidin, Vilchevskaya, and Korolev [2014]) and equal to c_*. That means that the first and the last terms in Eq (2.54) are equal to zero. According to the notation in Eq (2.27), the variation of the concentration at the interface is equal to s. Hence,

$$\delta\left(\ln\frac{c(\mathbf{r})}{c_*}\right) = \frac{s}{c_*}. \tag{2.55}$$

Finally, the linearized kinetic equation is obtained by substituting the linearized reaction rate (2.53) into the kinetic equation (2.6):

$$\begin{aligned}\frac{1}{\kappa_{\text{ch}}}\frac{\mathrm{d}\eta}{\mathrm{d}t} =& \frac{n_- M_-}{\rho_-}\Big[-\mathbf{q}^0_-:\Big([\![\mathbf{C}]\!]^{-1}-\mathbf{K}_+(\mathbf{n}_0)\Big):[\![\mathbf{C}]\!]:\boldsymbol{\varepsilon}_-(\mathbf{w}_-)-\\ &\eta\,\mathbf{q}^0_-:\Big([\![\mathbf{C}]\!]^{-1}-\mathbf{K}_+(\mathbf{n}_0)\Big):\Big(\mathbf{n}^0\cdot\Big(\nabla\boldsymbol{\varepsilon}^0_-:[\![\mathbf{C}]\!]\Big)\Big)\Big]+RT\frac{s}{c_*}\end{aligned} \tag{2.56}$$

where κ_{ch} is a positive constant.

2.3 Stability of a planar chemical interface

As a first example, a stability of the planar interface is analyzed using the aforementioned procedure. A chemical reaction in the layer of thickness H is considered, as illustrated in Fig. 2.3. Lower boundary is fixed and displacement u_0 in y-direction is applied at the upper boundary. This external load is further considered as a parameter for controlling the resulting equilibrium position.

Diffusing constituent is supplied through the lower boundary and the reaction takes place at $y = h$. This gives the following boundary condition for the mechanical equilibrium equation, (2.19):

$$\begin{aligned} &\mathbf{u}|_{y=0} = \mathbf{0}, \qquad \mathbf{u}|_{y=H} = u_0 \mathbf{e}_y, \\ &u_x = 0, \qquad\qquad \sigma_{xy} = 0, \qquad \text{at } x = 0 \text{ and } x = L. \end{aligned} \tag{2.57}$$

and for the diffusion equation, (2.21):

$$\begin{aligned} D\mathbf{n} \cdot \nabla c + \alpha (c - c_*) = 0, \qquad &\text{at } y = 0, \\ \mathbf{n} \cdot \nabla c = 0, \qquad &\text{at } x = 0 \text{ and } x = L. \end{aligned} \tag{2.58}$$

Linear elastic solid reactants are considered with the constitutive equations (2.7) and elasticity tensors taken in a form

$$\mathbf{C}_\pm = \lambda_\pm \mathbf{II} + 2\mu_\pm {}^4\mathbf{I}, \tag{2.59}$$

where $\lambda_\pm$ and $\mu_\pm$ are Lamé parameters and ${}^4\mathbf{I}$ is the forth rank unit tensor. For the sake of simplicity of further derivations, the chemical transformation strains assumed to be planar, namely $\boldsymbol{\varepsilon}^{\text{tr}} = \varepsilon^{\text{tr}}(\mathbf{e}_x\mathbf{e}_x + \mathbf{e}_y\mathbf{e}_y)$. One should note that the chosen boundary conditions (for both mechanical equilibrium and diffusion problem) on left and right boundaries of the layer may be considered as a way to model an infinite layer.

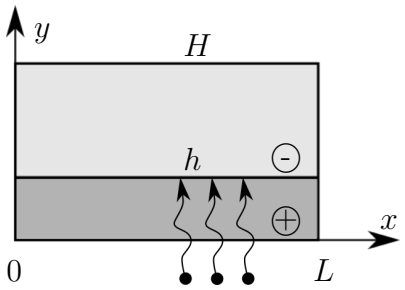

Fig. 2.3: A schematic representation of the planar chemical reaction front.

Assuming that the parameters of the problem are such that there exists an equilibrium configuration of the reaction front inside the layer, the mathematical problem is to determine whether this configuration is physically stable or unstable. Furthermore, only planar equilibrium configurations of the front are considered, i.e., all points of the front belong to the line $y = h$, where h is a constant. At this state, the solution of the balance equation and the diffusion equation are displacements $\mathbf{u}^0$ and concentration $c^0 = c_*$, the stresses emerging in the body are denoted as $\boldsymbol{\sigma}^0$. The closed form expressions for these quantities

are shown in Appendix A.1. From this point, the superscript "0" refers to the variable taken from the solution of the unperturbed BVP.

According to the utilized approach, as described in Section 2.2, the equilibrium configuration of the front is perturbed,

$$\mathbf{R} = \mathbf{R}^0 + \eta\,(x,t)\,\mathbf{n}^0, \tag{2.60}$$

where $\mathbf{R}$ and $\mathbf{R}^0$ are positions of the points of the front at the perturbed and the unperturbed states, respectively, $\mathbf{n}^0 = \mathbf{e}_y$ at the equilibrium, $\eta\,(x,t)$ is the amplitude of the perturbation. The perturbation of the front necessary leads to the perturbation of the solutions of the PDEs:

$$\begin{aligned} \mathbf{u}\,(x,y,t) &= \mathbf{u}^0\,(y) + \mathbf{w}\,(x,y,t)\,, \\ \mathbf{w}\,(x,y,t) &= u\,(x,y,t)\,\mathbf{e}_x + v\,(x,y,t)\,\mathbf{e}_y, \\ c\,(x,y,t) &= c^0\,(y) + s\,(x,y,t)\,, \end{aligned} \tag{2.61}$$

where $\mathbf{w}$ and s are the perturbation functions for the displacements and concentration respectively. From this point, the superscript "0" refers to the variable taken from the solution of the unperturbed BVP. Linearization of the balance equation gives

$$\nabla \cdot \boldsymbol{\sigma}_{\pm}\,(\mathbf{w}) = \mathbf{0}, \qquad \boldsymbol{\sigma}_{\pm}\,(\mathbf{w}) = \mathbf{C}_{\pm} : \nabla\mathbf{w}. \tag{2.62}$$

The boundary conditions from (2.57) are:

$$\begin{aligned} &\mathbf{w} = \mathbf{0}, && \text{at } y = 0 \text{ and } y = H, \\ &\mathbf{w}\cdot\mathbf{e}_x = 0, \qquad \boldsymbol{\sigma}_{\pm}\,(\mathbf{w}) : \mathbf{e}_x\mathbf{e}_y = 0, && \text{at } x = 0 \text{ and } x = L, \end{aligned} \tag{2.63}$$

and interface conditions at $y = h$ are defined in (2.26).

The linearized diffusion equation reads:

$$\Delta s = 0, \tag{2.64}$$

and the linearized boundary conditions (2.58) are

$$\begin{aligned} D\mathbf{n}\cdot\nabla s + \alpha s &= 0, && \text{at } y = 0, \\ D\mathbf{n}^0\cdot\nabla s + \omega\,(\mathbf{w}, s) &= 0, && \text{at } y = h, \\ \mathbf{n}\cdot\nabla s &= 0, && \text{at } x = 0 \text{ and } x = L. \end{aligned} \tag{2.65}$$

Variations of energy $\delta\chi(\mathbf{w})$ and the reaction rate $\delta\omega\,(\mathbf{w}, s)$ have form (2.48) and (2.53), respectively.

Solution of the perturbed system of equations (2.62) and (2.64) defines the dependency of displacements $\mathbf{u}$ and concentration c (and therefore the reaction

front velocity) on the amplitude of the perturbation η. For the case of the planar interface, these dependencies can be obtained analytically in a series form. To satisfy the boundary conditions at $x = 0$ and $x = L$, the solution is found as series

$$u(x,y,t) = \sum_{n=1}^{\infty} U_n(y,t)\sin(k_n x), \quad v(x,y,t) = \sum_{n=1}^{\infty} V_n(y,t)\cos(k_n x),$$
$$\eta(x,t) = \sum_{n=1}^{\infty} \xi_n(t)\cos(k_n x), \quad s(x,y,t) = \sum_{n=1}^{\infty} S_n(y,t)\cos(k_n x), \quad k_n = \frac{n\pi}{L}.$$

One can show that functions $U_n(y,t)$ and $V_n(y,t)$ which satisfy equation (2.62) are

$$\begin{aligned} U_n(y,t) = {} & A_n(t)\exp(k_n y) + B_n(t)\, y\exp(k_n y) + \\ & C_n(t)\exp(-k_n y) + D_n(t)\, y\exp(-k_n y), \\ V_n(y,t) = {} & \left(-A_n(t) + B_n(t)\frac{\lambda+\mu+2}{\lambda+\mu}\frac{1}{k_n}\right)\exp(k_n y) - B_n(t)\, y\exp(k_n y) + \\ & \left(C_n(t) + D_n(t)\frac{\lambda+\mu+2}{\lambda+\mu}\frac{1}{k_n}\right)\exp(-k_n y) + D_n(t)\, y\exp(-k_n y). \end{aligned}$$

Since the material properties are different for domains Ω_+ and Ω_-, there are two functions U_n. The first is defined in Ω_+ with Lamé parameters λ_+ and μ_+, the second is defined in Ω_- with Lamé parameters λ_- and μ_-. Analogously, there are two functions V_n. Functions A_n, B_n, C_n, D_n are then found from the boundary conditions (2.63). Time dependency in these functions comes from dependency of the boundary conditions on $\eta(x,t)$. It is easy to see from the boundary conditions that each function A_n, B_n, C_n, D_n is proportional to $\xi_n(t)$, e.g., $A_n(t) = a_n\xi_n(t)$, where a_n is some constant. This allows expressing variation $\delta\chi$ as a function of ξ_n:

$$\delta\chi(t) = \sum_{n=1}^{\infty} L_n^{\mathrm{ph}}\xi_n(t)\cos(k_n x), \tag{2.66}$$

where L_n^{ph} is a constant. Here the superscript "ph" refers to the phase transformation, since the expression (2.66) is to be used in the kinetic equation (2.52) if the phase transformation interface stability is considered.

Further, the perturbed diffusion equation (2.64) has to be solved. Function $S_n(y,t)$ can be found in a form

$$S_n(y,t) = E_n(t)\exp(k_n y) + F_n(t)\exp(-k_n y), \tag{2.67}$$

where functions E_n, F_n are found from the boundary conditions. Furthermore,

as seen from the boundary conditions, each function E_n, F_n is proportional to $\xi_n(t)$, e.g., $F_n(t) = f_n L_n^{\text{ph}} \xi_n(t)$, where f_n is a constant. Thus, from the boundary conditions, it is easy to show that

$$E_n(t) = L_n^{\text{ph}} \xi_n(t) \frac{-\kappa}{\phi_n}, \qquad F_n(t) = L_n^{\text{ph}} \xi_n(t) \frac{-\kappa}{\phi_n} \frac{Dk_n - \alpha}{Dk_n + \alpha}, \tag{2.68}$$

where the following notation is introduced:

$$\begin{aligned} \phi_n = {} & Dk_n \exp(k_n h) - Dk_n \frac{Dk_n - \alpha}{Dk_n + \alpha} \exp(-k_n h) + \\ & k_* \exp(k_n h) + k_* \frac{Dk_n - \alpha}{Dk_n + \alpha} \exp(-k_n h), \\ \kappa = {} & k_* c_* \frac{1}{RT} \frac{n_- M_-}{\rho_-}. \end{aligned}$$

When all the constants are found, and the corresponding perturbed functions $\mathbf{w}$ and s are obtained, one can substitute them into the kinetic equation (2.56). Then the following equation for the evolution of the perturbation ξ_n is obtained:

$$\frac{1}{\kappa} \frac{\rho_-}{n_- M_-} \frac{\mathrm{d}\xi_n}{\mathrm{d}t} = L_n^{\text{ch}} \xi_n,$$

where

$$L_n^{\text{ch}} = L_n^{\text{ph}} \left(1 - \frac{k_* \exp(k_n h) + k_* \dfrac{Dk_n - \alpha}{Dk_n + \alpha} \exp(-k_n h)}{\phi_n} \right). \tag{2.69}$$

Sign of L_n^{ch} defines the behavior of the solution: when the sign is negative for each n, the perturbation decays in time, and the reaction front moves back to its equilibrium position. If at least one L_n is positive, than the perturbation with this wave number grows exponentially, which leads to the instability of the interface.

The specific form of the obtained expression for L_n^{ch} is very useful. One can show that the expression in parentheses in (2.69) is always positive. This means that sings of L_n^{ch} and L_n^{ph} always coincide. If a stress-induced phase transformation problem is considered, for which the velocity is defined by equation (2.52), similar analysis of a perturbed boundary gives

$$\frac{1}{k_{\text{ph}}} \frac{\mathrm{d}\xi_n}{\mathrm{d}t} = L_n^{\text{ph}} \xi_n.$$

Since L_n^{ch} and L_n^{ph} have identical signs, the physical stability of a phase boundary

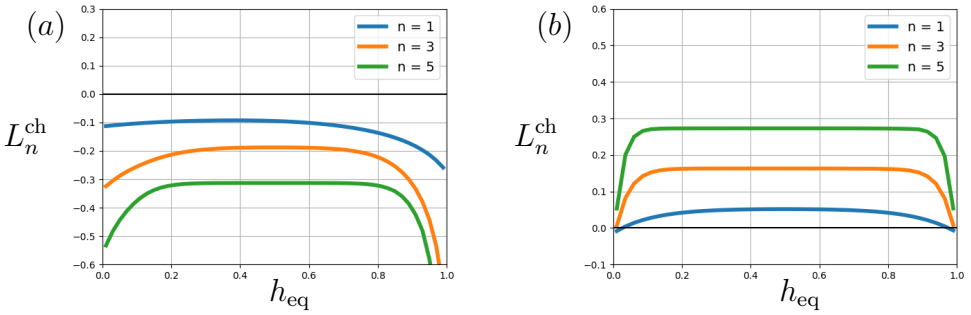

Fig. 2.4: L_n-lines for the stability analysis of the planar chemical reaction front for stable (a) and unstable (b) sets of elastic parameters.

in the phase-transformation problem necessarily results in the physical stability of a chemical reaction front in the chemo-mechanical problem. Therefore, the diffusing reactant does not influence stability of the front. The diffusion process cannot stabilize the physically unstable front and also otherwise.

In Fig. 2.4 different possible scenarios are shown. The plots (a) and (b) correspond to stable and unstable sets of material parameters for the planar interface, respectively. For the stable configuration L_n^{ch} is negative for each n and all possible positions of the equilibrium position (which, as mentioned earlier, is controlled by the external load u_0). For the unstable configuration the solution shows positive values of the L_n^{ch}'s .

It should be noted that negative values of the L_n's is only a necessary but not a sufficient stability condition. For the problem of phase transformation, which is mathematically pretty similar to the problem of chemical transformation, there is another necessary stability criteria which is based on the analysis of so called phase transition zones (PTZ). It was proved in Grabovsky and Truskinovsky [2011]; Grabovsky and Truskinovsky [2013] that if strains at the equilibrium interface belong to the boundaries of the phase transition zones, then this configuration is stable. This approach cannot be explicitly extrapolated to the case of the chemical reaction, therefore PTZ and perturbation approaches are later compared for the phase transformation problem.

Another weakness of the perturbation method is as follows. Assuming the aforementioned configuration with the planar chemical interface with the given material properties, one can obtain values for L_n^{ch} for each positive integer n. However, with growing n, system of equations for functions A_n, B_n, C_n, D_n becomes ill-conditioned. It means, that for higher wave numbers one cannot guarantee an accurate solution. However, for several observed cases, the absolute value of L_n^{ch} increases with n for both stable and unstable configurations, as shown in Fig. 2.4.

One should note, that the material parameters for the following problems are chosen to be dimensionless because of the following reasons. The purpose of Sections 2.3–2.5 is the qualitative analysis of the stability behavior, that is validated by the numerical results in the following Chapter 3. When considering stability analysis, the material parameters are varied to consider different physical scenarios, therefore, there is no reference to the real engineering problem. Also, during the development of the numerical procedures, it is a common practice to use dimensionless units. The units are taken into account in the last Chapter 4, where the real engineering application is considered.

Having all this in mind, the following procedure was utilized in order to obtain a stability regions in the material parametric space. It was shown, that diffusion parameters of the model do not influence the stability behavior, so they are kept fixed. In addition the Poisson's ratios are fixed so that $\nu_+ = \nu_- = 0.25$, the elasticity modulus for one of the materials is selected to be $E_- = 60$, external load was set to $u_0 = 0.02$. With this, the parametric space for the following study is defined by ratio E_+/E_-, the value of the chemical transformation ε^{tr} and the energy parameter γ. In this work for the sake of convenience, the chemical energy parameter γ was adjusted in order to get the equilibrium position at the middle ($h_{eq} = 0.5$) of the layer. From physical point of view, variation of γ may correspond to the variation of temperature.

Varying the selected parameters, one can obtain the areas, where the values for L_1 are positive or negative, Fig. 2.5.

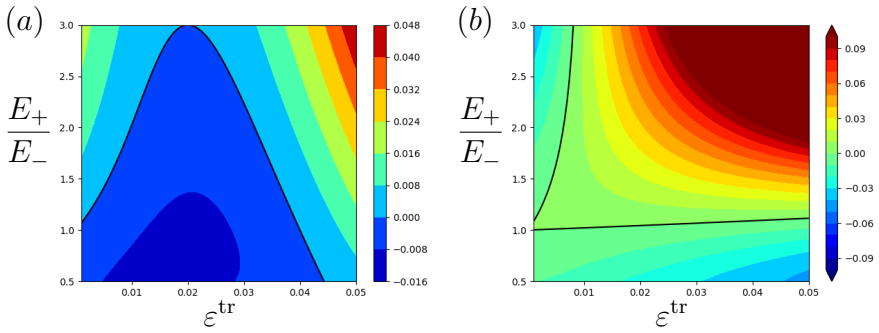

Fig. 2.5: The contour plots of: (a) – γ for given external load in material parameter space; (b) – L_1 for given external load in material parameter space at corresponding γ from figure (a). Black solid lines in (b) represent the $L_1 = 0$ level.

The stability regions in Fig. 2.5 prescribe only a necessary condition, meaning that if the region says "unstable" ($L_1 > 0$) then the system is physically unstable. However, if the region states "stable" ($L_1 < 0$), an additional check for $n \geq 2$ is required. Using these plots the stable (with the additional check) and unstable configurations are selected for further study. The sets of elasticity parameters at which the equilibrium planar chemical reaction front with a normal parallel

	λ_+	λ_-	μ_+	μ_-	$\varepsilon^{\mathrm{tr}}$
Stable	40	10	34	26	0.005
Unstable	66	34	50	66	

Tab. 2.1: Stable and unstable sets of material properties and parameters used in analytical study and numerical simulation for the planar interface problem.

to the tensile or compressive deformation is stable or unstable are listed in the Tab. 2.1. Later in the text set of parameters for which the equilibrium position of the interface is stable or unstable is reffered to as "stable set of parameters" or "unstable set of parameters", respectively.

It has been shown that chemical and diffusion parameters do not affect the stability of the planar interface in the equilibrium position. Therefore only one set of the following chemical and diffusion parameters are used and they are listed in Tab. 2.2.

Parameter	$\frac{n_- M_-}{\rho_-}$	RT	c_*	D	k_*	α
Value	43.2	2434.8	0.1	0.1	0.01	0.2

Tab. 2.2: Diffusion parameters used in analytical study and numerical simulation for the planar interface problem.

These parameters are used in the following Chapter 3 as a reference values to validate numerical procedures.

2.4 Stability of a cylindrical chemical interface

Consider a hollow cylinder undergoing a a chemical reaction, Fig. 2.6. Due to symmetry only a quarter of the cylindrical cross-section will be shown in all further figures.

The problem is axially symmetric, which means that $\mathbf{u} = u(r)\mathbf{e}_r$. As it was done in the case of planar interface, the transformation strains are assumed to be planar:

$$\boldsymbol{\varepsilon}^{\mathrm{tr}} = \varepsilon^{\mathrm{tr}}(\mathbf{e}_r\mathbf{e}_r + \mathbf{e}_\phi\mathbf{e}_\phi), \tag{2.70}$$

where $\mathbf{e}_r$ and $\mathbf{e}_\phi$ are unit vectors of a cylindrical coordinate system. The boundary conditions refer to the quantities shown in Fig. 2.6, where ρ is an interface radius, a and b are inner and outer radii of the cylinder, respectively, can be written as

$$\begin{aligned} \sigma_r(a) = 0, \quad u(b) = u_0, \\ [\![u(\rho)]\!] = 0, \quad [\![\sigma_r(\rho)]\!] = 0. \end{aligned}$$

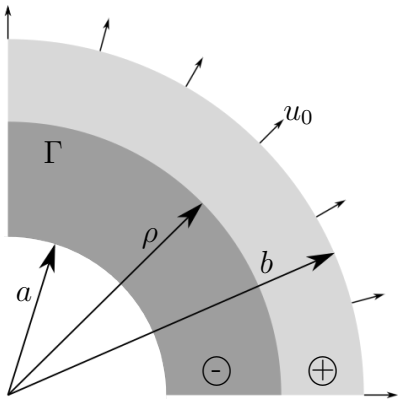

Fig. 2.6: A hollow cylinder undergoing a phase transformation.

Diffusing reactant for the chemical reaction is supplied through the outer surface of the cylinder. As it was done in previous sections a stationary diffusion is considered. The corresponding diffusion equation in the case of axial symmetry becomes:

$$\frac{\mathrm{d}}{\mathrm{d}r}\left(\frac{1}{r}\frac{\mathrm{d}c}{\mathrm{d}r}\right) = 0, \quad r \in [\rho, b]. \tag{2.71}$$

Boundary and interface conditions according to the notation of Figure 2.6 can be written as follows (as described in Section 2.1):

$$D\frac{\mathrm{d}c}{\mathrm{d}r}\Big|_{r=b} - \alpha(c_* - c(b)) = 0, \quad D\frac{\mathrm{d}c}{\mathrm{d}r}\Big|_{r=\rho} - k_*\left(c(\rho) - c_{\mathrm{eq}}(\rho)\right) = 0. \tag{2.72}$$

The solution to this particular problem can be found analytically as it was shown in details, e.g., in Vilchevskaya and Freidin [2007] for the phase transformation front kinetics problem. This solution and its extension for the chemical reaction front propagation are given in the Appendix A.2.

If a cylinder undergoing a phase transformation,the phase transition front velocity is given by the following expression (see Freidin [2007])

$$V_n^{\mathrm{ph}} = -\dot{\rho} = \kappa_{\mathrm{ph}}\chi(\rho), \qquad \kappa_{\mathrm{ph}} > 0, \tag{2.73}$$

where χ is the same as in the expression of the chemical affinity tensor A_{nn}, (2.14), but without the chemical energy term in the expression for the energy parameter γ, (2.15). Parameter κ_{ph} is a positive constant. One should note that in current problem formulation $\mathbf{n} = -\mathbf{e}_r$. For a given load u_0 and choice of material parameters the dependence of the driving force χ on the interface radius can be plotted. This driving force may have a zero value for

a certain radius as shown in Fig. 2.7. For this radius the normal component of the velocity of the interface is zero, so this radius is then referred to as an equilibrium position.

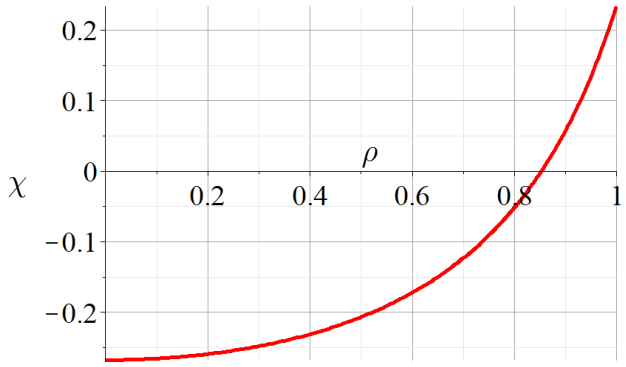

Fig. 2.7: Dependence of the driving force on the interface radius.

Note that if the initial radius of the interface is greater than the equilibrium one, the sign of the driving force χ is positive. Then according to (2.73) the normal component of the velocity is positive. Keeping in mind that $\mathbf{n} = -\mathbf{e}_r$, the phase transformation front is forced to move toward the equilibrium position. The same happens if the initial radius of the interface is less then equilibrium radius. This means that the solution is stable at the equilibrium radius with respect to the radial perturbations.

The external load u_0 can be considered as a parameter for controlling the resulting equilibrium radius. Examples of the dependencies of the position of the equilibrium radius on the external load are shown in Fig. 2.8 (a) and (b) for a solid and for a hollow cylinder, respectively. Note that an equilibrium radius may not exist within the range between internal and external radii of the cylinder for some values of u_0. In the case of a hollow sphere or a hollow cylinder two equilibrium radii may correspond to one external load. A more detailed discussion of this phenomenon for the spherical problem can be found in Eremeev, Freidin, and Sharipova [2007]. Moreover, the case of an external load at which there is only one equilibrium radius and the interface is stable with respect to radial perturbations is considered in that reference.

As mentioned above, the equilibrium position of the interface is reached when the thermodynamic force is equal to zero in all points of the interface. Linear stability analysis considers small perturbations of the displacements and position of the interface. Consequently, similarly to the planar interface problem in Section 2.3, the displacement, concentration and the interface

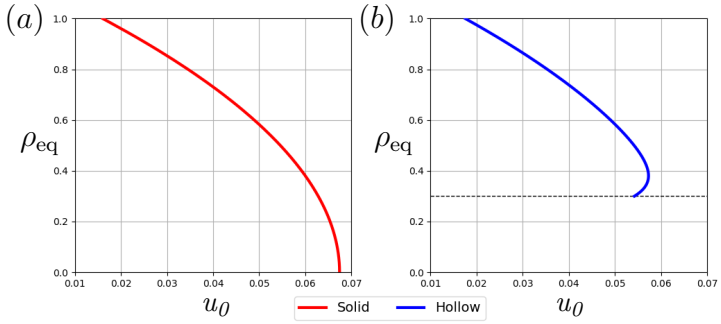

Fig. 2.8: Dependence of thermodynamically equilibrium interface radius on the external load for (a) – solid and (b) – hollow cylinders. Dashed line in (b) corresponds to the inner radius of the hollow cylinder.

position in a cylindrical coordinate can be written as

$$\begin{gathered}\mathbf{u} = \mathbf{u}^0(r) + \mathbf{w}(r,\phi), \quad \mathbf{R} = \mathbf{R}^0 + \eta(\phi)\mathbf{n}^0, \\ \mathbf{w}(r,\phi) = u(r,\phi)\mathbf{e}_r + v(r,\phi)\mathbf{e}_\phi, \\ c = c^0(r) + s(r,\phi).\end{gathered} \tag{2.74}$$

For the case of the hollow cylinder equilibrium equation (2.25) can be rewritten as shown in Vilchevskaya and Freidin [2007]:

$$(\lambda+2\mu)\frac{\partial\psi}{\partial r} - \frac{2\mu}{r}\frac{\partial\omega}{\partial\phi} = 0, \qquad (\lambda+2\mu)\frac{1}{r}\frac{\partial\psi}{\partial\phi} - 2\mu\frac{\partial\omega}{\partial r} = 0, \tag{2.75}$$

where

$$\psi = \frac{\partial u}{\partial r} + \frac{1}{r}\left(u + \frac{\partial v}{\partial\phi}\right), \qquad \omega = \frac{\partial v}{\partial r} + \frac{1}{r}\left(v - \frac{\partial u}{\partial\phi}\right).$$

Then the boundary conditions on the free inner surface ($r = a$) are

$$\lambda\psi + 2\mu\frac{\partial u}{\partial r} = 0, \quad \frac{\partial v}{\partial r} = 0.$$

On the outer surface ($r = b$), where Dirichlet boundary conditions are applied, the perturbation function has to vanish. Therefore

$$u = 0, \quad v = 0.$$

The interface conditions at $r = \rho$ from (2.26) can be written for the new

variables u and v as

$$\begin{aligned} [\![u]\!] &= -\eta \left[\!\!\left[\frac{\mathrm{d}u^0}{\mathrm{d}r} \right]\!\!\right], \qquad [\![v]\!] = 0, \\ \left[\!\!\left[\lambda\psi + 2\mu \frac{\partial u}{\partial r} \right]\!\!\right] &= -\eta \left[\!\!\left[\frac{\mathrm{d}\sigma_r^0}{\mathrm{d}r} \right]\!\!\right], \qquad \left[\!\!\left[2\mu \frac{\partial v}{\partial r} \right]\!\!\right] = \frac{\mathrm{d}\eta}{\mathrm{d}\phi} [\![\sigma_\phi^0]\!]. \end{aligned} \tag{2.76}$$

Linearized diffusion equation (2.28) for the perturbed concentration in cylindrical coordinates takes the form

$$\Delta s(r,\phi) = \frac{\partial^2 s}{\partial r^2} + \frac{1}{r}\frac{\partial s}{\partial r} + \frac{1}{r^2}\frac{\partial^2 s}{\partial \phi^2} = 0 \tag{2.77}$$

with boundary conditions

$$\begin{aligned} -D\frac{\partial s}{\partial r} + k_* \left(s + c_* \frac{n_- M_-}{\rho_-} \frac{\delta\chi}{RT} \right) = 0 \quad &\text{at the reaction front,} \\ D\frac{\partial s}{\partial r} + \alpha s = 0 \quad &\text{at the outer surface.} \end{aligned} \tag{2.78}$$

Together with Eq. (2.75) and its boundary conditions, which are related to the perturbed mechanical problem, equations (2.77) and (2.78) form a set of equations for u, v and s. The aforementioned system of equations with the boundary and interface conditions can be uniquely solved with respect to the unknown functions. To do so, one has to follow the method proposed in Eremeev, Freidin, and Sharipova [2007] and the solution proposed by Vilchevskaya and Freidin [2007] for the phase transformation problem. One can seek the solution in a series form:

$$\begin{gathered} u(r,\phi) = \sum_{n=2}^{\infty} U_n(r)\cos(n\phi), \quad v(r,\phi) = \sum_{n=2}^{\infty} V_n(r)\sin(n\phi), \\ \eta(\phi) = \sum_{n=2}^{\infty} \xi_n \cos(n\phi). \end{gathered} \tag{2.79}$$

Then it is natural to seek the solution for s also as a series:

$$s(r,\phi) = \sum_{n=2}^{\infty} S_n(r)\cos(n\phi). \tag{2.80}$$

Substitution of these series into the BVP provides a set of equations for the amplitude functions $S_n(r)$, $U_n(r)$ and $V_n(r)$ for each integer number $n \geq 2$,

which can be found uniquely. This means, that they can be expressed as

$$U_n(r) = A_n^U(r)\xi_n, \quad V_n(r) = A_n^V(r)\xi_n, \quad S_n(r) = A_n^S(r)\xi_n \tag{2.81}$$

where A_n^U, A_n^V and A_n^S are certain linear operators. After the solution of these equations is obtained and substituted into the kinetic equation (2.56), the latter takes the following form:

$$\frac{1}{\kappa_{\text{ch}}}\frac{\mathrm{d}\xi_n}{\mathrm{d}t} = L_n^{\text{ch}}\xi_n, \tag{2.82}$$

where L_n^{ch} is a linear integro-differential operator. Similarly to the planar interface solution given in Section 2.3, the solution of this equation is an exponential one, and its power is defined by L_n^{ch}. The character of the solution is then governed by the sign of L_n^{ch}. If the sign for each n is negative then the power of the exponent is also negative and the coefficients ξ_n tend to zero in time. This means that the function η, $(2.79)_3$, vanishes in time and it can be concluded that the perturbed interface moves toward its original equilibrium position. If for at least one value of n the sign of the L_n^{ch} is positive, then the amplitude ξ_n will grow exponentially in time. Then the solution will be unstable and the lowest number n for which L_n^{ch} is positive will define the mode of the stability loss.

Analogously, if the stability analysis is performed for a cylinder undergoing a phase transformation, one can obtain values for L_n^{ph} from the solution of the perturbed BVP (2.75)–(2.76) and the variation of the kinetic equation (2.52). As a result for each number n an equation for the amplitude of perturbation ξ_n can be written as

$$\frac{1}{\kappa_{\text{ph}}}\frac{\mathrm{d}\xi_n}{\mathrm{d}t} = L_n^{\text{ph}}\xi_n, \tag{2.83}$$

where L_n^{ph} is a linear integro-differential operator. As in the problem with chemical interface, the character of the solution is governed by the sign of the L_n^{ph}. If the sign for each n is negative, then the power of the exponent is also negative and the coefficients ξ_n tend to zero in time. This means that the function η, which describes the divergence from the equilibrium position of the transformation front, vanishes in time and one can conclude that the solution is stable. If at least for one n the sign of the L_n^{ph} is positive, then the amplitude ξ_n will grow exponentially in time, the solution will be unstable.

In the case of cylindrical problem, the expressions for the L_n's are very long, which makes it impossible to relate L_n^{ch} and L_n^{ph} as it was done for the planar interface in (2.69). Therefore for selected number of material parameters both stability analyses are done: for phase transformation and for chemical reaction. This is done to check whether the diffusion can impact the stability.

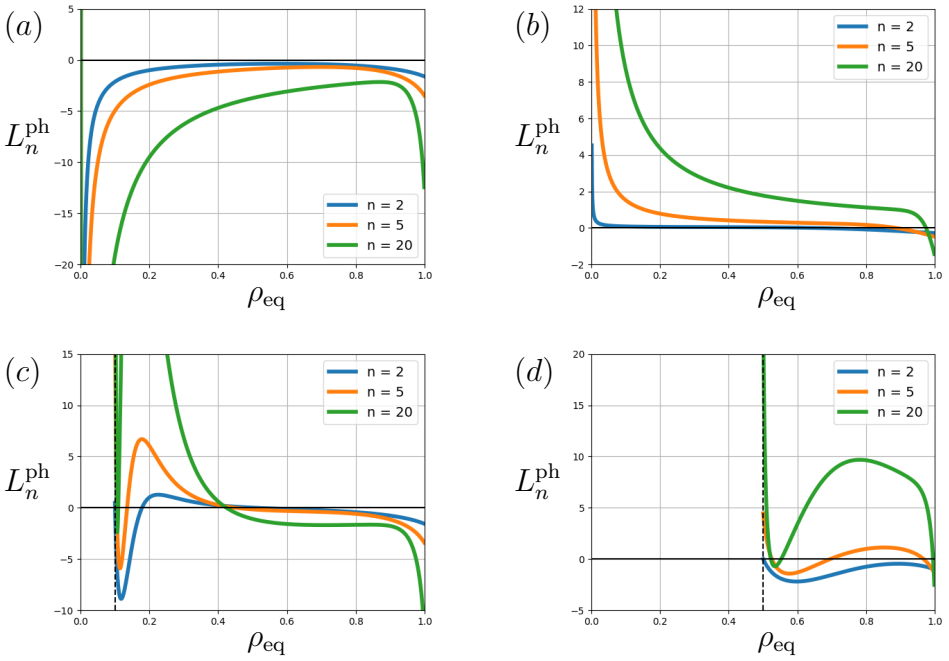

Fig. 2.9: L_n-lines for the stability analysis of the cylindrical phase interface for: (a) - stable set of elastic parameters for the solid cylinder, (b) - unstable set of elastic parameters for the solid cylinder, (c) - stable set of elastic parameters for the hollow cylinder with internal radius $r = 0.1R$, (d) - stable set of elastic parameters for the hollow cylinder with internal radius $r = 0.5R$.

Since expressions for L_n's do not add any value to the results they are omitted in the manuscript. However, these complicated equations still can be solved analytically without numerical methods. To handle them the symbolic mathematics software Mathematica was used.

In Fig. 2.9 different possible phase transformation front stability scenarios are shown. The plots (a) and (b) correspond to stable and unstable sets of material parameters for the solid cylinder, respectively. For a stable configuration L_n^{ph} is negative for each $n \geq 2$ and all possible positions of the equilibrium radius. For the unstable configuration the solution shows positive L_n^{ph}'s. Plots (c) and (d) were calculated only for "stable" material parameters and show the influence of the inner diameter of the hollow cylinder on the stability of the interface. Small holes, Fig. 2.9(c), lead to an unstable solution only for the configuration where the equilibrium radius is close to the hole. The limit case, when the hole diameter tends to zero, gives the solution for the solid cylinder, as expected. Fig. 2.9(d) shows that for large inner diameters of the cylinder the solution is unstable even for a stable set of parameters.

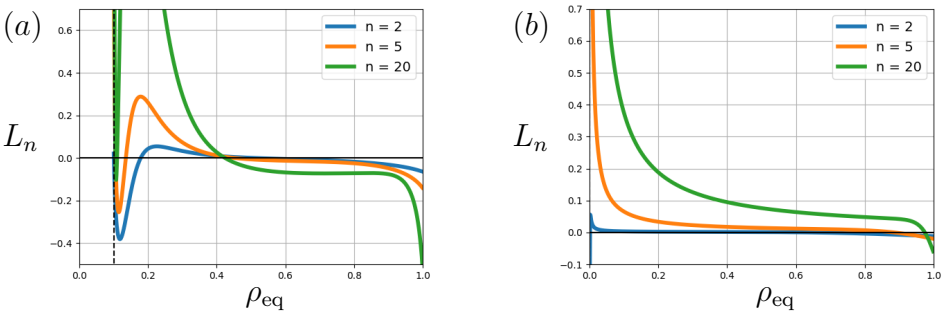

Fig. 2.10: L_n-lines for the stability analysis of the cylindrical chemical reaction front for: (a) – stable set of elastic parameters for the hollow cylinder with internal radius $r = 0.1R$, (b) – unstable set of elastic parameters for the solid cylinder.

	λ_+	λ_-	μ_+	μ_-
Stable configuration	25	45	10	25
Unstable configuration	45	25	25	10

Tab. 2.3: Material properties and parameters used in analytical and numerical simulation. Material "+" refers to the outer, material "−" to the inner region, respectively.

In Fig. (2.10) results are shown for the stable configuration of material properties from Tab. 2.3, diffusion properties from Tab. 2.2 and energy parameter $\gamma = 0.15$ for solid (a) and hollow (b) cylinders. For all configurations, the presence of the diffusion in the model does not change the system behavior compared to the phase transformation problem. The presence of inner hole has the same effect on the stability behavior as in the phase transformation: a small inner diameter affects only configurations where the equilibrium radius is close to inner surface and in the limit of a vanishing radius results in the solution for the solid cylinder. Large holes make the system unstable.

Using these results, the stable and unstable configuration is selected for further studies. These values are listed in the Tab. 2.3. These parameters are used in the following Chapter 3 as a reference values to validate numerical procedures.

2.5 Remark on phase transition zones

For the problem of phase transformation, which is mathematically pretty similar to the problem of chemical transformation, there is another necessary stability criteria. The latter is based on the analysis of so called phase transition zones. It was proved in Grabovsky and Truskinovsky [2011]; Grabovsky and Truskinovsky [2013] that if strains at the equilibrium interface belong to the

boundaries of the phase transition zones, then this configuration is stable. However, this approach cannot be explicitly extrapolated to the case of the chemical reaction.

The procedure of obtaining the process zones was discussed in many papers, starting from Freidin and Chiskis [1994a]; Freidin and Chiskis [1994b] (more general nonlinear elastic cases), Morozov and Freidin [1998] (linear elastic case) and recent works about microstructures and optimal composites Antimonov, Cherkaev, and Freidin [2016]; Freidin and Sharipova [2019]. In this section, a short overview of this procedure is presented. Then, the PTZ approach is utilized in order to validate results obtained with the perturbation method.

For the phase transformation problems, to construct the PTZs one has to analyze the driving force χ given in a form (2.23). With this expression, only the last term depends on the normal vector $\mathbf{n}$. For the case of linear isotropic material, this term is a quadratic form and reads

$$\mathcal{K}_-(\mathbf{n}) = \mathbf{q}_+ : \mathbf{K}_-(\mathbf{n}) : \mathbf{q}_+ = \frac{1}{\mu_-}\left(N_2 - \frac{\lambda_- + \mu_-}{\lambda_- + 2\mu_-} N_1^2\right), \tag{2.84}$$

where

$$N_1 = \mathbf{n} \cdot \mathbf{q}_+ \cdot \mathbf{n}, \qquad N_2 = \mathbf{n} \cdot \mathbf{q}_+^2 \cdot \mathbf{n} \tag{2.85}$$

are so-called orientation invariants. It was shown that minimization of energy with respect to the microstructure geometry (i.e., normal $\mathbf{n}$ direction) leads to extrema condition of (2.84) at given $\mathbf{q}_+$. The maximum of $\mathcal{K}_-(\mathbf{n})$ corresponds to minimum of energy.

For the case of two phase configuration with only one inter-phase boundary, the direction of the maximizing normal $\mathbf{n}^*(\mathbf{q}_+)$ can be expressed through the principal values of tensor $\mathbf{q}_+$. Let q_{max}, q_{mid} and q_{min} be the maximum, intermediate and minimum eigenvalue of $\mathbf{q}_+$ respectively with corresponding eigenvectors $\mathbf{e}_{max}$, $\mathbf{e}_{mid}$ and $\mathbf{e}_{min}$; $|q|_{max}$ and $|q|_{min}$ be the maximum and minimum absolute value of $\mathbf{q}_+$ eigenvalues. Then if

$$q_{min}q_{max} < 0, \quad \text{or} \quad \begin{cases} q_{min}q_{max} > 0 \\ (1-\nu_-)|q|_{min} < \nu_-|q|_{max} \end{cases} \tag{2.86}$$

the maximizing normal $\mathbf{n}^* = n_{max}\mathbf{e}_{max} + n_{min}\mathbf{e}_{min}$ and

$$n_{max}^2 = \frac{(1-\nu_-)q_{max} - \nu_- q_{min}}{q_{max} - q_{min}}, \quad n_{min}^2 = \frac{\nu_- q_{max} - (1-\nu_-)q_{min}}{q_{max} - q_{min}}. \tag{2.87}$$

Otherwise, namely

$$\begin{cases} q_{min} q_{max} > 0 \\ (1-\nu_-)|q|_{min} > \nu_- |q|_{max}, \end{cases} \tag{2.88}$$

the maximizing normal has only one component the basis of eigenvectors of $\mathbf{q}_+$ and $\mathbf{n}^* = n_{max}\mathbf{e}_{max}$.

Recalling the case of planar interface described in Section 2.3, the equilibrium configuration is a horizontal interface with the normal $\mathbf{n} = \mathbf{e}_y$. In this problem, the eigenvectors of $\mathbf{q}_+$ correspond to the Cartesian basis vectors, and $\mathbf{q}_+ = q_x^+ \mathbf{e}_x\mathbf{e}_x + q_y^+ \mathbf{e}_y\mathbf{e}_y + q_z^+ \mathbf{e}_z\mathbf{e}_z$. With this, the horizontal interface at the equilibrium position is stable only if the condition (2.88) is satisfied and q_y is the maximum eigenvalue of $\mathbf{q}_+$. Analogously, for the cylindrical interface from Section 2.4, only condition (2.88) leads to the stable equilibrium interface with the normal $\mathbf{n} = \mathbf{e}_r$.

Phase transition zones built with the use of (2.86) and (2.88) are shown in Figs. 2.11 and 2.12 for the planar and cylindrical problems, respectively. These plots are built for the stable cases of phase transformation equilibrium, and material parameters are given in Tabs. 2.1 and 2.3. Solid dots in both figures represent the actual strains at the interface in the equilibrium position. Dashed lines correspond to the condition (2.86) and solid lines – to condition (2.88).

For selected material parameters strains at the interface belong to the phase transition zones in the case of planar interface and the minimizing normal vector has only one component $\mathbf{e}_y$, so the configuration is stable. It is shown earlier in the discussions about (2.69) that the diffusion does not affect the stability of planar interface. Therefore, one can conclude that the chemical interface is also stable.

For selected material parameters strains at the interface belong to the phase transition zones in the case of cylindrical interface and the minimizing normal vector has only one component $\mathbf{e}_r$, so the configuration is stable. It is not possible to study analytically the influence of the diffusion on the stability of the cylindrical interface (see Section 2.4), therefore stability of the cylindrical chemical interface cannot be proved.

2.6 Conclusions

Problem of a chemical interface propagation in linear elastic solids is formulated based on the concept of chemical affinity tensor from works by Freidin [2013]; Freidin, Vilchevskaya, and Korolev [2014]; Freidin [2015]; Freidin *et al.* [2016].

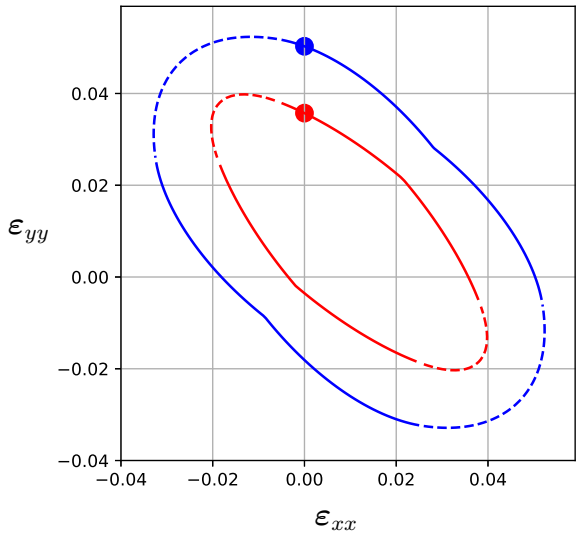

Fig. 2.11: Phase transition zones for the stable set of material parameters from Tab. 2.1. Blue and red dots correspond to the strain state for planar interface configuration. Dashed lines correspond to the condition (2.86), solid lines – to condition (2.88).

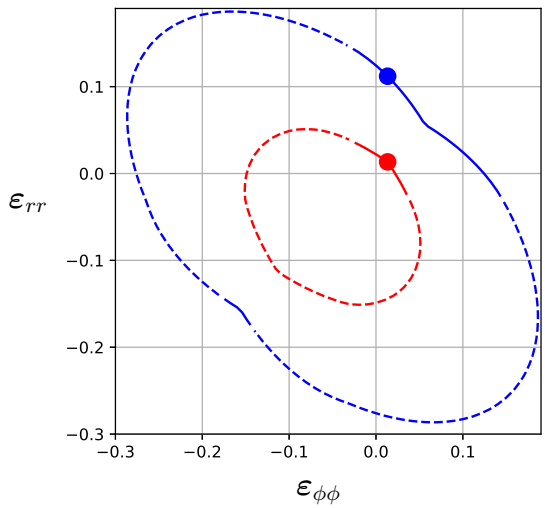

Fig. 2.12: Phase transition zones for the stable set of material parameters from Table 2.3. Blue and red dots correspond to the strain state for cylindrical interface configuration. Dashed lines correspond to the condition (2.86), solid lines – to condition (2.88).

An estimation for the total deformation J^{tr} due to the chemical transformation and the diffusion model is proposed.

A linear stability analysis problem is formulated for the phase transformation interface in the equilibrium position (based on works by Eremeev, Freidin, and Sharipova [2003]; Eremeev, Freidin, and Sharipova [2007]) and extended to the case of the chemical interface. A detailed derivation for of the boundary and interface conditions, as well as the kinetic equation, is given for the perturbed phase transformation front and chemical interface.

In this work, the stability problems of a planar and cylindrical chemical interface were considered analytically using the perturbed kinetic equation approach. For the planar interface, it was shown that the diffusion does not affect the stability of the interface. Stability regions were constructed in material parametric space for that problem. For a cylindrical chemical interface, two cases were studied: hollow and solid cylinders undergoing a chemical reaction. It was shown that a small inner diameter does not affect the stability behavior of the interface when the equilibrium position is far enough from the hole, while large inner diameters with prescribed boundary conditions on them make the system always unstable. Due to the complexity of the perturbed kinetic equation, it was not possible to prove analytically the influence of the diffusion parameters on the stability of the interface, when compared to the mathematically similar problem for the phase transformation. However, the results of the analyses show that for the selected choice of material parameters diffusion did not change the stability behavior.

Even for the simple geometries and linear elastic materials, the perturbed stability analysis is quite complicated and cumbersome. Therefore, in the next chapter, it is studied whether the developed numerical approach for simulating the chemical reaction (and the phase transformation) front propagation can reveal stability or instability of the chemical interface.

Based on the results of the stability analysis, two sets of material parameters are selected for further numerical studies of planar and cylindrical interfaces. These sets are further referred as “stable” and “unstable” for stable and unstable interface equilibrium position, respectively. An additional check was done for the stable set of parameters using the PTZ approach. The latter, however, is only relevant for the phase transformation problem. Its extension to the case of the chemical reaction is not straightforward and was out of the scope of this work. The PTZ criteria confirmed the stability of the phase transformation front for the selected material parameters. As mentioned earlier, for all studied cases the diffusion did not affect the stability behavior, therefore, it is assumed that considered stable configurations are stable indeed.

All methods in this chapter considered the stability of the chemical reaction front at the equilibrium position. The next chapter considers numerical studies

of the chemical interface approaching this equilibrium position for both: stable and unstable configurations.

3 Numerical simulation and study of the chemical reaction front kinetics

There is a large variety of numerical approaches that can handle problems with moving interfaces. All of them can be divided into two groups relying on a smooth and a sharp representation of the interface. A typical example of the smooth-interface approach is the phase-field method, see e.g. Svendsen, Shanthraj, and Raabe [2018]; Weinberg, Werner, and Anders [2018] in application to chemo-mechanics and Schneider *et al.* [2017]; Schneider *et al.* [2018] in application to the phase transformations. These methods require an additional equation which governs the evolution of the phase field variable. Since the kinetic equation for the interface is already chosen in the previous chapter, it might be not convenient to utilize the phase field method to solve considered type of problems. Moreover, given kinetic equation based on chemical affinity tensor concept uses jump conditions across the interface. They are much easier to satisfy for the sharp interface methods, where the thickness of the interface is neglected. Therefore, the latter was chosen to be implemented using the finite element method.

All sharp-interface finite-element based methods can be divided into three subcategories. The first subcategory is when the interface coincides with the element edges (or faces in 3D case) and the geometry is completely remeshed each time the interface moves, e.g., Mueller and Gross [1998]; Mueller and Gross [1999]; Gross, Mueller, and Kolling [2002]; Mueller, Gross, and Lupascu [2006] for the case of phase transformations and, e.g., Freidin *et al.* [2016] in application to chemo-mechanics. The second subcategory also relies on the interface coinciding with the element edges/faces, however, the mesh in only distorted as the interface moves, i.e., the nodes are moved, without changing neither the number of the nodes nor the mesh connectivity, e.g., Morozov *et al.* [2018a] in application to chemo-mechanics where such approach has been implemented using the isogeometric method. The third subcategory unites approaches where the interface cuts through the finite-element mesh in an arbitrary way and moves independently of the mesh, which is unchanged from one time increment to another. Typical examples of such approaches are the level set method (e.g., Duddu *et al.* [2011]; Zhao, Bordas, and Qu [2015]; Moghadam and Voorhees [2016]) and the CutFEM, e.g., Hansbo, Larson, and Larsson [2017]; Burman *et al.* [2018]; Poluektov and Figiel [2019]. In current

work, the remeshing method is utilized for solving problems of moving chemical interfaces. The used procedure is compared with the isogeometric analysis and with the CutFEM method, therefore all free sharp-interface finite-element based methods are covered in this study.

3.1 Description of the numerical procedure

Numerical procedure in the case of small strains and linear elastic materials explicitly follows the analytical procedure showed in the Section 2.1. All the assumptions from the previous chapter still hold:

- A plain strain formulation is considered;
- Both materials are assumed to be linear elastic;
- Diffusion of the particles does not introduce additional stresses (the solid skeleton approach);
- Diffusion process is assumed to be much faster than the chemical reaction front propagation;
- Some initial position of the chemical interface is introduced in the geometry.

Necessity of existence of some thin initial layer of the new material is one of the weaknesses of this procedure. In order to obtain the solution for stresses, strains and concentration, one have to get at least one layer of finite elements for each material domain. This issue is much less strict in the meshless methods like aforementioned CutFEM. However it has its own challenges, which will be discussed later in this chapter.

With the given geometry, interface position and boundary conditions, one can obtain all the required values to calculate the normal component of the affinity tensor, A_{nn}. Indeed, since in the considered class of problems (as described in Chapter 2) the mechanical and diffusion problems are decoupled, one can solve them separately one after another. Solution of the first problem gives the stresses and strains at the reaction front. These values are then substituted into the boundary condition at the moving interface for the diffusion problem. Solution of the latter gives the concentration of the diffusing constituent at the chemical reaction front. Now, the A_{nn} can be calculated, and substituted into the kinetic equation, providing the normal component of the reaction front velocity. This kinetic equation is solved with the explicit Euler scheme and with the given time increment one can calculate the normal displacement for each point of the interface. With the new position of the chemical reaction front,

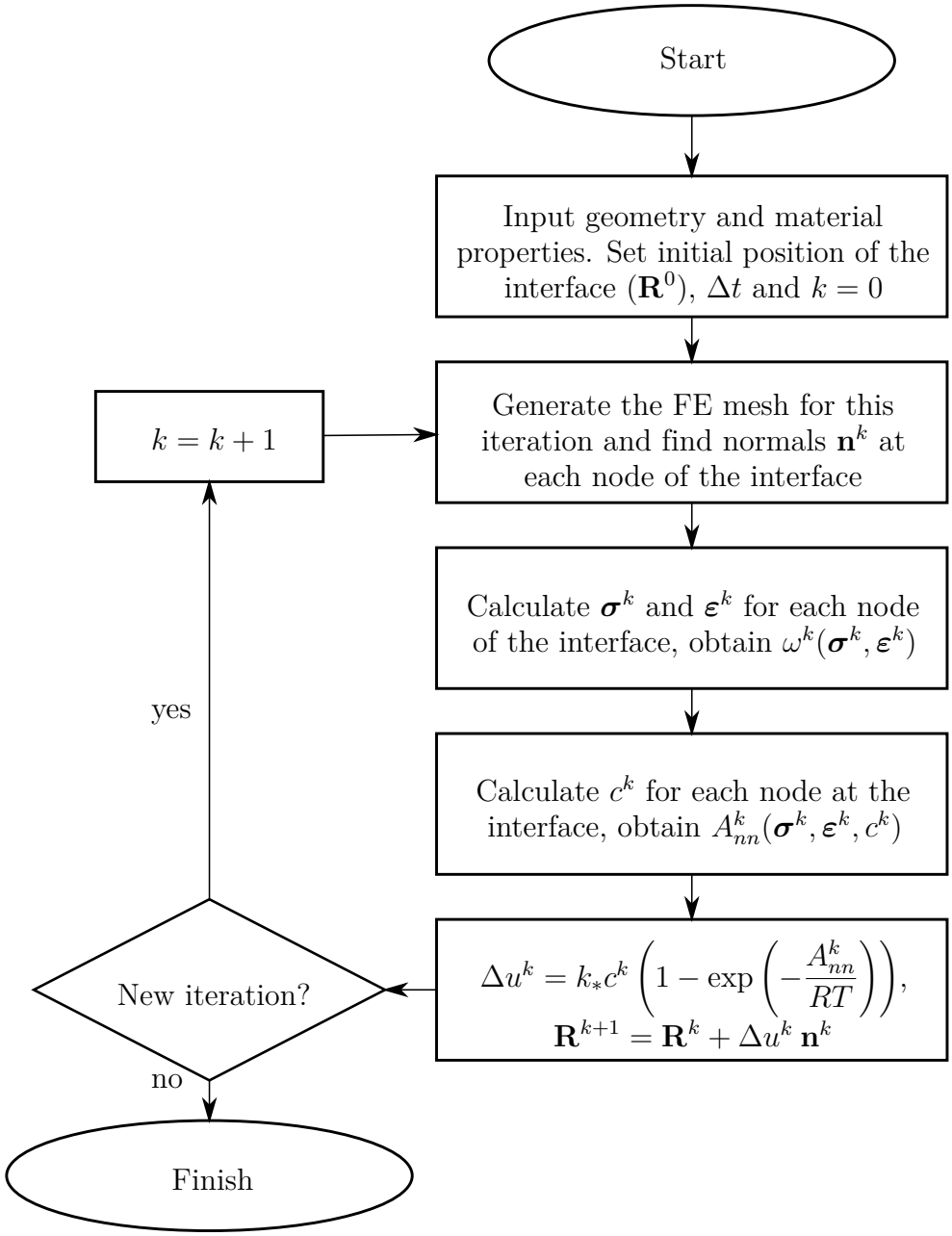

Fig. 3.1: The flowchart for the numerical algorithm.

the procedure starts over with the next iteration. This process is summarized in the flowchart shown in Fig. 3.1.

Since the used mathematical model provides the expression for the normal

component of the reaction front velocity, one has to accurately calculate the normal vector **n** to the reaction front. This is one of the main reasons why on the first stages of this research, the isogeometric FEM procedures (Hughes, Cottrell, and Bazilevs [2005]) were utilized. Problem formulation and main results can be found in Morozov *et al.* [2018a]. By using Non-Uniform Rational B-Splines (NURBS) as basis functions, one can calculate with high accuracy the direction of the normal vector for any external or internal edge (curve) of a geometrical domain, and particularly for the chemical reaction front. In addition, IGA is more accurate with less computational effort compared to standard FEA, cf. Morganti *et al.* [2015]. Comparison of the IGA and classical FE models for the cylinder problem is shown in Fig. 3.2.

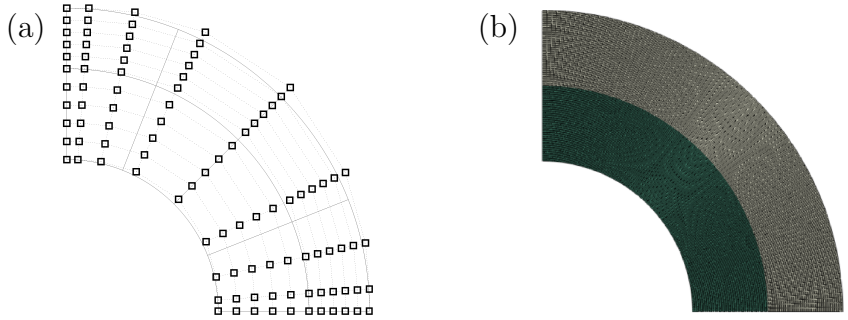

Fig. 3.2: Geometry described by NURBS curves which is directly used for the numerical simulation (a). Classical FE model for the numerical simulation (b).

Since IGA uses displacements of control points as degrees of freedom which are not interpolative inside a domain, one cannot move the internal front directly in general case (not for simple translation and rotation). Therefore, a special procedure should be introduced to apply the displacement to the interface and "re-mesh" the domain appropriately. To do so, an additional elasticity problem is solved with Δu applied at the interface boundary as non-homogeneous Dirichlet boundary conditions. Nitsche's method is used for imposing such kind of boundary conditions weakly (Hansbo [2005], see also Juntunen and Stenberg [2009] and references therein). Doing that, the elements are simply distorted without changing the topology or mesh connectivity. This new distorted mesh defines the new position of all the nodes (the whole isogeometric model) and can be used as an input to the next iteration. Number of elements remain the same during all analysis. This can be handled without loss of the numerical accuracy because higher distortion of the elements is allowed in the isogeometric method when compared to the standard FEM.

Despite all advantages, iterative update of the interface position may become very complicated when the geometry is defined by NURBS, especially when the interface between the domains has to be extrapolated or trimmed after the

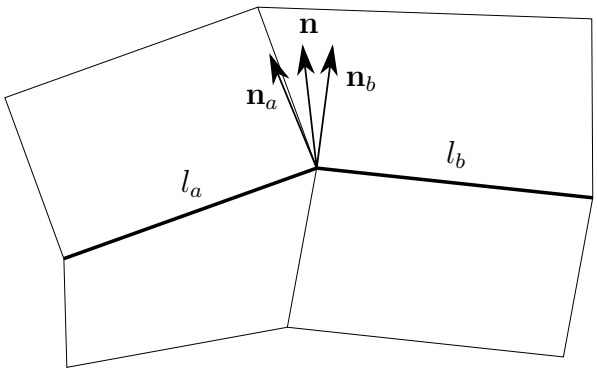

Fig. 3.3: Definition of the normal vector to the piecewise linear interface on the FE mesh

movement. It was decided that working with more complex geometries and loading scenarios is more important than computational time, therefore, for the later studies the classical FEM procedure was utilized.

Traditional finite elements defines the interface as a piecewise linear curve which makes it impossible to determine the normal uniquely. Usually, the normal vector at a node is defined as a weighted sum of normal vectors to the element edges, Fig. 3.3,

$$\mathbf{n} = \frac{1}{\sqrt{l_a^2 + l_b^2 + 2 l_a l_b \mathbf{n}_a \cdot \mathbf{n}_b}} \left(l_a \mathbf{n}_a + l_b \mathbf{n}_b \right), \tag{3.1}$$

where $\mathbf{n}_a$ and $\mathbf{n}_b$ are the normal vectors to the element edges, l_a and l_b are the lengths of these edges.

As mentioned earlier, in some configurations when moving the interface it has to be adjusted, as shown in Fig. 3.4. The interface (the blue curve) may move inside (left boundary) or outside (right boundary) the body domain. The movement in normal direction is shown by black arrows and the new position of the interface is indicated by a black dashed line.

In order to avoid this unphysical configuration, where the start and end of the reaction front do not belong to the boundary of the body domain, a special procedure was created. It cuts and linearly extrapolates the interface to adjust the boundaries as shown by red curve in Fig. 3.4. In the analysis, this adjusted curve is considered as a new position of the interface.

The numerical analysis was performed with the commercial finite element program Abaqus. The problem was solved quasi-statically as described in Freidin *et al.* [2016]; Morozov *et al.* [2018a]; Morozov *et al.* [2018b], where the position of the interface defines the time dependence. A special Python script

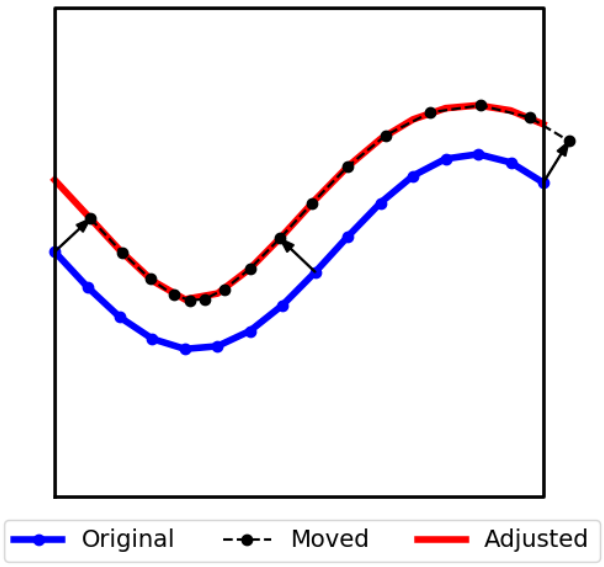

Fig. 3.4: Automated adjustment of the interface position during its propagation.

for Abaqus was developed to automate the process flow and postprocess the results.

3.2 Kinetics of the cylindrical chemical reaction front approaching the blocking state

A cylinder undergoing the chemical reaction is considered, as described in Section 2.4 and in Fig. 2.6. Due to symmetry, only a quarter of the cylinder is modeled. A thin layer of transformed material was assumed in the initial state for the analysis. Material parameters for stable and unstable configurations were chosen for the finite element model in accordance with Tab. 2.3. In order to compare the kinetics near the thermodynamic equilibrium, the external boundary conditions u_0 were adjusted so that the equilibrium radii are the same for both problems.

Fig. 3.5 (b) shows how the radius of the interface changes in time. The stable configuration converges smoothly to the analytically predicted equilibrium radius. For the unstable configuration, the blue line, change of radial coordinates are plotted for twenty equally spaced reference points distributed along the interface (highlighted in Fig. 3.5 (a)). Note that during the first fifteen increments, the displacements of these points are equal and the phase transformation front keeps its originally circular shape. However, when the front approaches the equilibrium radius, it changes its smooth behavior and

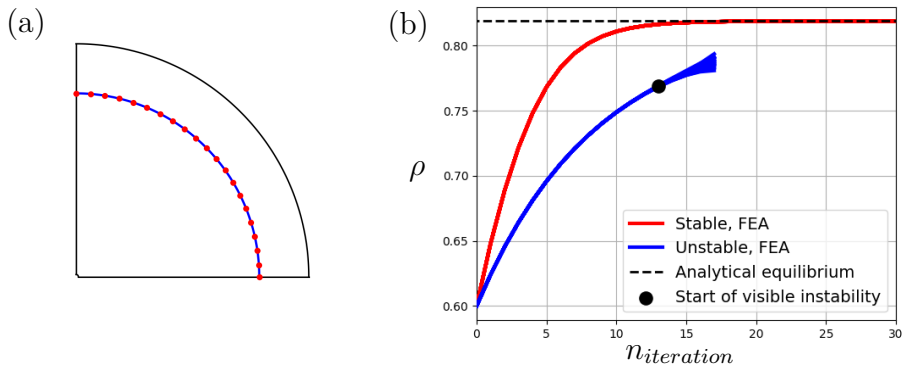

Fig. 3.5: (a) – set of reference points on the interface for the output. (b) – results of numerical simulations for stable (red curve) and unstable (blue curve) configurations for the phase transformation front propagation problem.

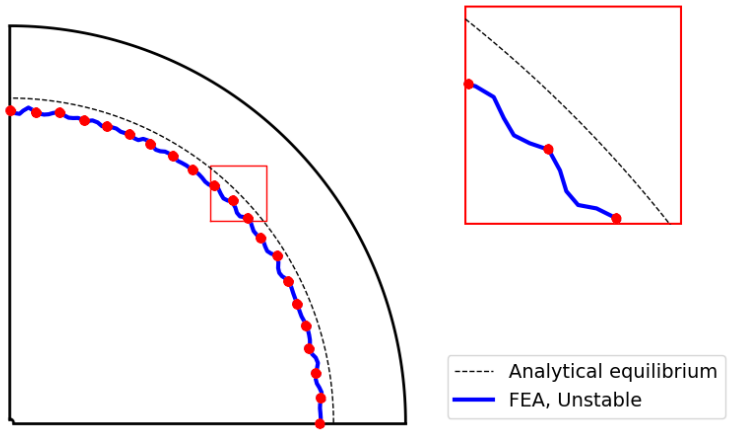

Fig. 3.6: Typical shape of the phase interface after losing stability near the equilibrium radius during numerical simulation.

the loss of stability is observed. The typical shape of the interface right after losing the stability is shown in Fig. 3.6. This mode of stability loss is governed by the numerical accuracy and, therefore, depends on the mesh discretization. The instability shape of the initially circular interface on the FE mesh is shown in Fig. 3.7.

The stable and unstable configurations behave in the same manner for phase and chemical transformation fronts. The interface approaches the equilibrium position similarly. Fig. 3.8 shows how the radius of the interface changes in time during the chemical reaction. For the unstable configuration, the blue line, the

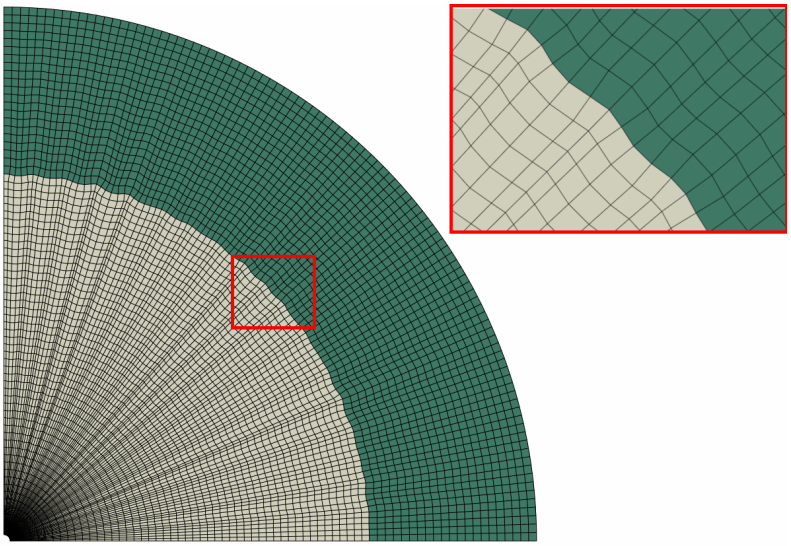

Fig. 3.7: Shape of initially circular interface after the loss of stability on the FE mesh.

change of radial coordinates are plotted for twenty points equally distributed along the interface. During the first twenty increments, the displacements of these points are equal and the chemical reaction front keeps its originally circular shape. As it approaches the predicted equilibrium radius, it changes the smooth behavior and stability loss occurs. If the initial shape of the reaction front is circular, the shape of the unstable interface is governed by the numerical inaccuracy as it was in the case of phase transformations. One can predefine the mode of the instability by introducing wave-type perturbations with small amplitude and different frequency into the initial configuration.

In order to present kinetics of the interface approaching the equilibrium radius from inside and from outside, the artificial case of so-called "backward reaction" is analyzed. The reverse reaction mechanism might differ from the direct reaction, but here it is assumed to be the same, just to test the numerical procedure. Therefore, the initial chemical interface radius is set closer to the center of the cross-section then the analytically predicted equilibrium radius. For simplicity, it is assumed that during the simulation the gaseous constituent diffuses from the chemical interface to the outer boundary of the body and the material "+" transforms back to the material "−".

Kinetics of the back and direct reactions with initially perturbed front is shown in Fig. 3.9 for unstable configuration. Top row corresponds to the back reaction and bottom - to the direct reaction. Left and right columns have different frequency of the initial perturbation. In the case of stable material parameters, the perturbations, as well as the ones introduced by numerical

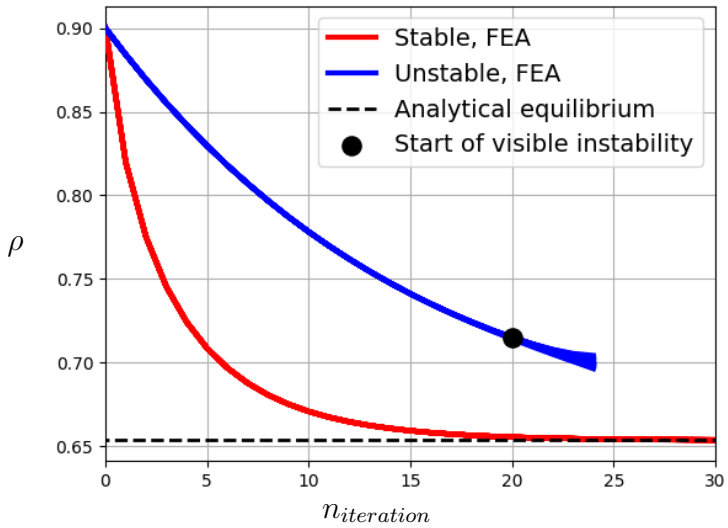

Fig. 3.8: Results of numerical simulations for stable (red curve) and unstable (blue curve) configurations for the chemical reaction front propagation.

inaccuracy, vanish and stability occurs at the equilibrium radius. But for another set of parameters, the perturbations amplify when the reaction front comes to the equilibrium position, so that one can see the predefined mode of the instability as shown in Fig. 3.9. This effect appears when the amplitude of the initial perturbation is greater then the accuracy of the numerical scheme.

3.3 A note about stresses caused by the interface instability

The growing perturbations in the case of unstable configuration result in the redistribution of the stress fields. Examples of the von Mises stress fields for circular and perturbed interfaces are shown in Fig. 3.10. For given example, stresses at the perturbed interface are much higher than on circular interface and, therefore, may lead to the plasticity or to some failure scenarios, like delamination or fracture.

Stresses caused by the instability amplitude growth were analyzed in Morozov, Freidin, and Müller [2019]. In this section, a static configuration is considered, in which the chemical interface has a predefined sinusoidal-type shape near the blocking state, as shown in Fig. 3.11. This position of the interface is similar to the one shown in Fig. 3.9, e.g., top right. The unstable set of parameters from Tab. 2.3 is used for the numerical analysis.

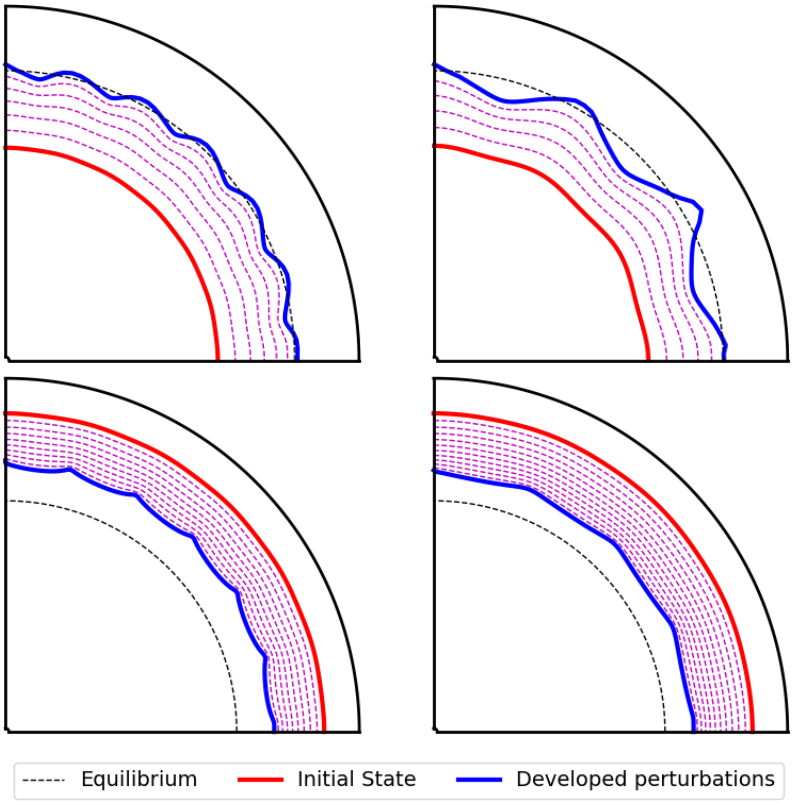

Fig. 3.9: Kinetics of the initially perturbed interface with different predefined modes of instability for the unstable set of material parameters. Top row - "backward reaction", bottom row - direct reaction.

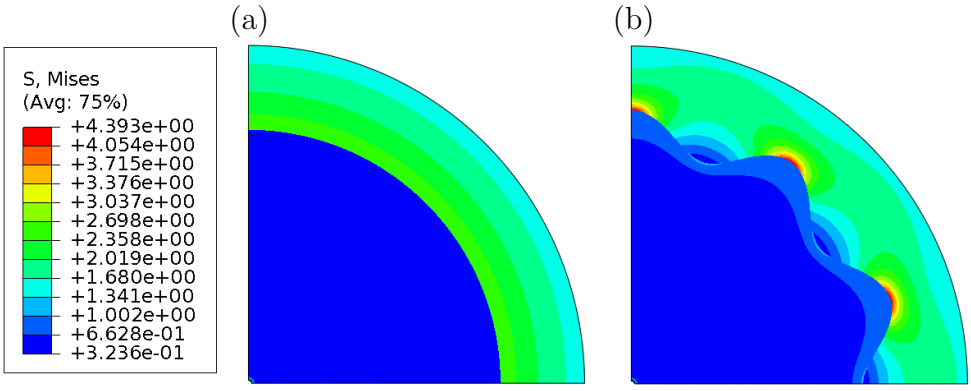

Fig. 3.10: The von Mises stress distribution for stable (a) and unstable (a) configurations.

Various amplitudes and frequencies for the interface shape were analyzed.

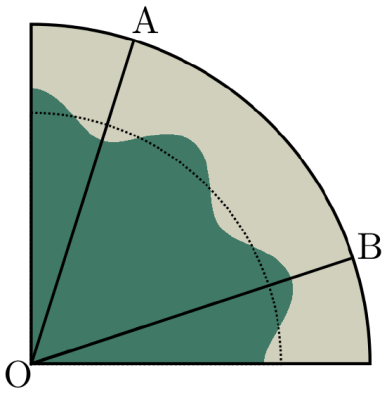

Fig. 3.11: Unstable configuration of a solid cylinder with predefined shape of the interface. Stress distributions are analyzed along radial lines OA and OB.

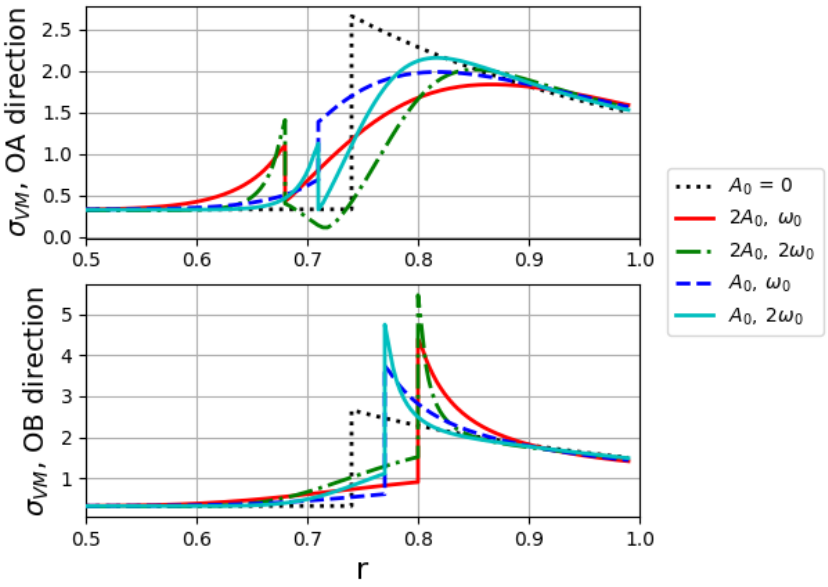

Fig. 3.12: Distributions of von Mises stress along corresponding directions

Stress distributions along the radial lines OA and OB (Fig. 3.11) are shown in Figs. 3.12–3.14.

The maximum von Mises stress in OB direction increases with the amplitude and frequency of the interface shape. As shown in the previous section, the amplitude grows with the propagation of the front in the unstable configuration. This may lead to intensive plastic deformations.

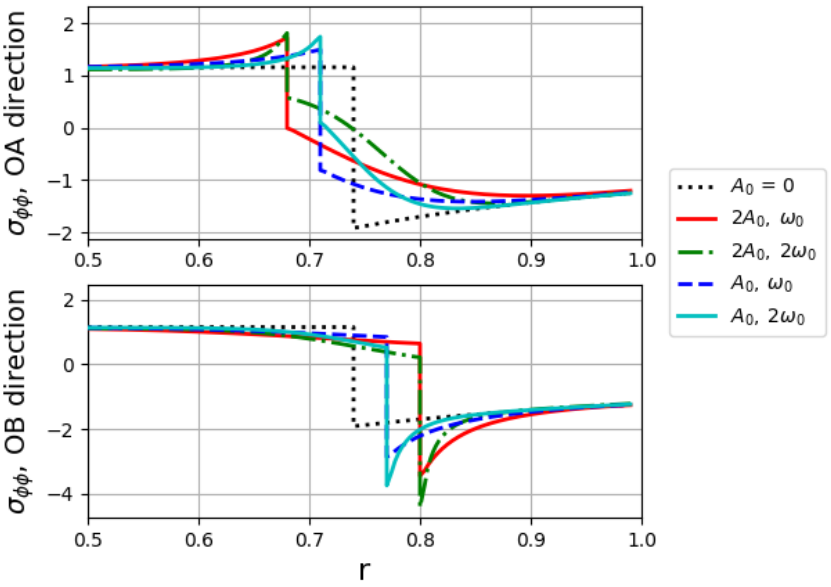

Fig. 3.13: Distributions of the hoop stress along corresponding directions

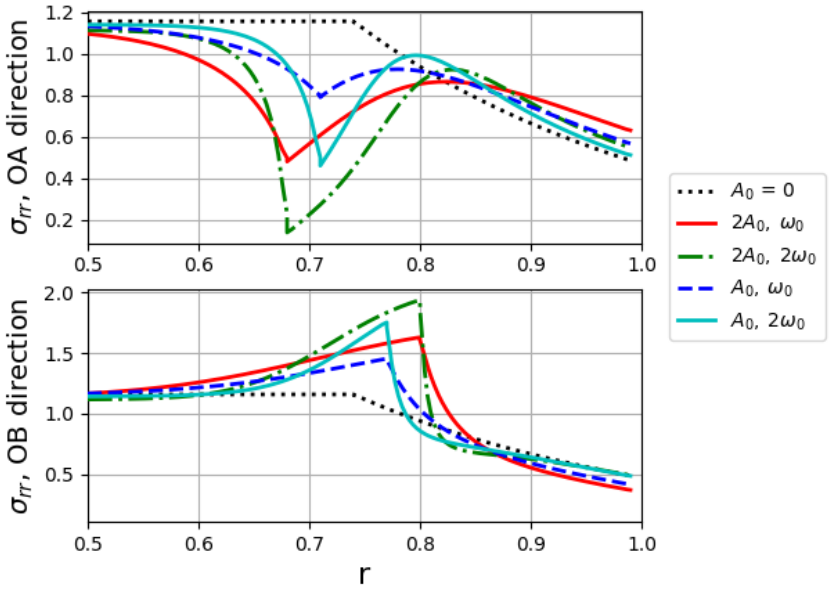

Fig. 3.14: Distributions of the radial stress along corresponding directions

One should note that negative hoop stress (Fig. 3.13) in both OA and OB directions do not change their sign in the vicinity of the stress concentration due to the amplitude growth of the reaction front perturbation. However, an increasing magnitude of the radial stress in the OB direction (Fig. 3.14) may lead to delamination. In this case, not only the stress distribution but also the conditions for the chemical reaction will change.

3.4 Comparison of the CutFEM and remeshing results

3.4.1 CutFEM overview

CutFEM belongs to subcategory of the numerical approaches where the interface cuts through the finite-element mesh in an arbitrary way and moves independently of the mesh. The mesh remains unchanged from one time increment to another. Similar numerical approaches based on the same ideas are the combination of the extended finite-element method (XFEM) to solve the PDEs and the level-set method to move the interface, e.g., Zhao, Bordas, and Qu [2013]; Zhao *et al.* [2013] in application to the phase transformations and Duddu *et al.* [2011]; Zhao, Bordas, and Qu [2015] in application to chemo-mechanics. Recently, the CutFEM method has been adapted for problems of mechanochemistry by Poluektov and Figiel [2019], where the numerical method has been formulated for the most general finite-strain mechanochemical setting, i.e., involving non-linear PDEs. The CutFEM method has been originally formulated for linear problems Burman and Hansbo [2012] and later adapted specifically to linear elasticity Burman *et al.* [2018]; Burman *et al.* [2019a]; Burman *et al.* [2019b].

The CutFEM method relies on two main features: enforcement of the interface conditions weakly using the Nitsche method, which allows solving the discretized PDEs with the interface cutting through the elements, and introduction of an inter-element stabilization, which addresses the ill-conditionality of the discrete problem related to the interface partitioning the elements into highly unequal spatial fractions. In Poluektov and Figiel [2019], the weak form for the finite-strain coupled mechanochemical problem has been derived from the variational principle, where problem-specific interface conditions (e.g., the force equilibrium and the displacement continuity for mechanics) and inter-element stabilization terms have been used.

In this section the comparison of CutFEM and remeshing methods is performed for linear elasticity. Therefore, the CutFEM-based method of Poluektov and Figiel [2019] has been simplified to a linear elastic setting. This step is out of scope of this work, therefore, the details are omitted.

The CutFEM-based and the remeshing methods are compared in three different examples, which are considered in the following sections. The first example

is the propagation of a planar reaction front, with an initially introduced perturbation. Two scenarios are considered: physically stable and physically unstable behavior. The second example simulates the interface kinetics in the specimen under shear load. The third example focuses on a different topology of the reaction front, namely a closed curve. All mentioned examples are solved on a 2D geometry with a plane-strain formulation, as it was done in previous sections.

3.4.2 Stable and unstable configurations for planar chemical interface

As mentioned above, to investigate the performance of the methods, physically stable and physically unstable scenarios are considered. Geometry of the problem is similar to one described in Section 2.3 and shown in Fig. 2.3. However in this simulation the planar reaction front has an initial cos-type perturbation.

For the mechanical problem, the following boundary conditions are used: clamped bottom boundary, symmetry conditions on left and right boundaries, prescribed displacements on top boundary (vertical displacement is u_0, horizontal displacement is zero). For the diffusion problem, the following boundary conditions are used: mixed boundary conditions on bottom boundary and interface (according to (2.22)), zero flux at left and right boundaries.

For the geometry dimensions $H = L = 1$ are used. The initial position of the perturbed interface is taken to be curve $y = 0.1 + 0.002\cos(6\pi x)$. For the physically stable case, Lamé parameters of the materials and transformation strain are given in Tab. 2.1. External displacement was set to $u_0 = 0.0453$. For the physically unstable case, the parameters are also taken from Tab. 2.1, but the applied displacement is $u_0 = -0.0381$. One should note, that external loads are different to adjust the equilibrium position to be in the middle of the layer at $h = 0.5$. As it was shown in Section 2.3, diffusion parameters do not influence the stability of the interface. Therefore, only one set of the chemical and diffusion parameters were used and they are listed in Tab. 2.2. Energy parameter is taken $\gamma = 0.05$.

In Fig. 3.15, for the physically stable case, the time-evolution of the reaction front is shown by plotting the y-coordinate of three different points of the interface, with coordinates $x = 1/3$, $x = 1/2$, $x = 2/3$, for both CutFEM and remeshing solutions. It can be seen that for the most part of the simulation time, all six curves are indistinguishable. At that stage, the absolute difference between y-coordinates of the points resulting from two methods is in the range of 10^{-4} to 10^{-6}. However, when the velocity of the front becomes slow, near the equilibrium position, the CutFEM-based approach produces an artifact: the front rapidly aligns with the nearest element edges. This happens due

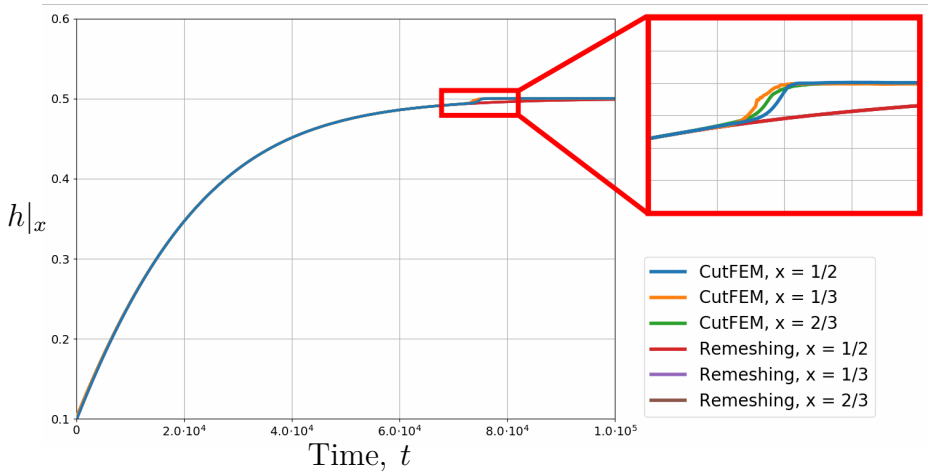

Fig. 3.15: Results of numerical simulations by CutFEM and by the remeshing procedures. Propagation of a planar chemical reaction front for stable configuration is illustrated by the evolution of y-coordinate of three points of the front.

to numerical error of the stresses becoming dominant in the reaction front driving force at slow front velocities and is the major disadvantage of using this method for modeling an approach to the equilibrium. This issue arises from the use of linear triangular elements and the calculation of the finite-element stresses, which are constant within such elements. Therefore, to correct this artifact in th CutFEM procedure, either a higher-order elements must be used, or improved stress-calculation procedures must be involved.

In Fig. 3.16, for the physically unstable case, the time-evolution of the reaction front is shown by snapshots of the front configuration at four different moments of time. It can be seen that the discrepancy between the results obtained by numerical methods accumulates with time and is mostly revealed at the boundaries of the domain. The accumulation in time is related to physical instability of the interface: as any perturbation of the front should grow in time, a numerical perturbation (i.e. a numerical error) also grows. The discrepancy at the edges of the domain is related to slightly different extrapolation procedures in both approaches, the edge points of the interface are allowed to move inside the domain (as shown in Fig. 3.4). In this case the extrapolation is used to find new intersection points of the interface and the boundary of the domain. For the CutFEM-based method, this has been described in Poluektov and Figiel [2019] and for the remeshing it is shown in Section 3.1.

For CutFEM, the mesh consists of linear elements in the form of isosceles right triangle with the side of Δx. In the remeshing procedure, linear quads with full integration were used, while the size of an element was approximately

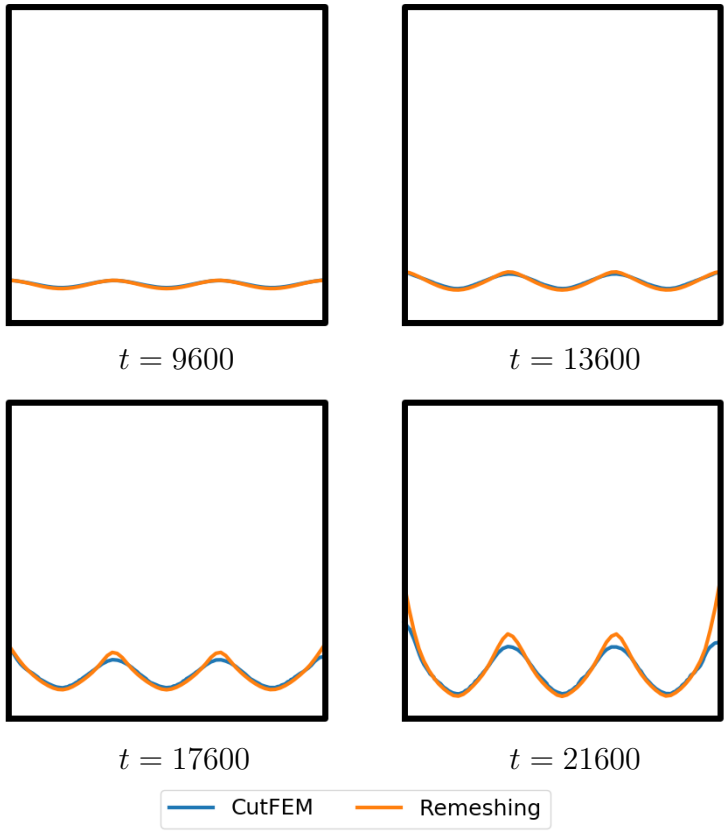

Fig. 3.16: Results of numerical simulations by CutFEM and by the remeshing procedures. Kinetics of the initially perturbed interface for the unstable configuration is illustrated by four snapshots of the reaction front at different times.

equal to Δx. For this example $\Delta x = 1/64$ was taken. Time steps of $\Delta t = 80$ and $\Delta t = 160$ were taken for the physically stable and unstable cases respectively. For CutFEM, numerical parameters, which were denoted as λ and κ in Poluektov and Figiel [2019], were taken 10^4 and 10 respectively. Examples of the meshes are shown in Fig. 3.17.

As shown in Fig. 3.15, in the case of stable equilibrium position of the interface, the perturbation diminishes as the front approaches the equilibrium position. When the selected elastic material constants correspond to equilibrium being physically unstable, Fig. 3.16, the amplitude of the perturbation rapidly (exponentially, as shown analytically in Section 2.3) grows, even before the front approaches the equilibrium position. From this, one can conclude that both methods reveal the instability effect and adequately simulate stable scenarios.

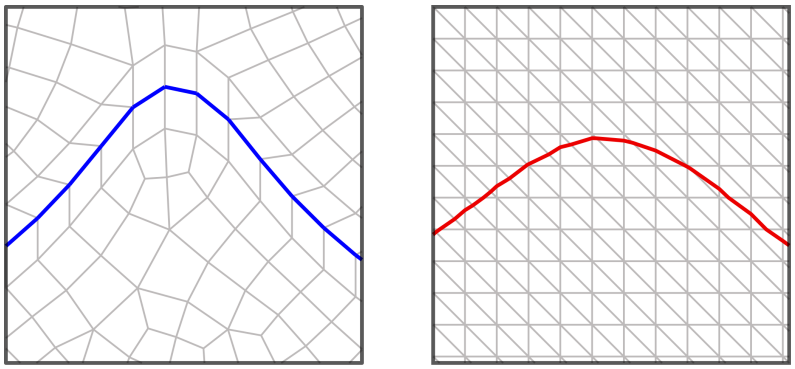

Fig. 3.17: Cropped examples of the finite-element meshes used in CutFEM and remeshing procedures are shown for the snapshot at $t = 17600$ in Fig. 3.16.

Therefore, both of them can be used for modeling the reaction front kinetics approaching stable and unstable equilibrium position.

3.4.3 Stable configuration for the chemical interface under shear

The second considered case is similar to the first example, however, an additional shear displacements are applied at the top boundary. Therefore, the model setup and the boundary conditions are same, except prescribed displacements on top boundary: $\mathbf{u} = u_0\mathbf{e}_y + 0.01\mathbf{e}_x$. This creates a shear stress state, therefore, if the initial position of the interface is horizontal the interface should rotate, as it approaches the stable equilibrium position. Exactly this is observed in the results of numerical simulations shown in Fig. 3.18, where snapshots of the front configuration at four different moments of time are plotted.

The time-evolution of the reaction front is shown in Fig. 3.19 by plotting the y-coordinate of three different points of the interface with coordinates $x = 1/5$, $x = 1/2$, $x = 4/5$, for both CutFEM-based and remeshing approaches.

Since the reaction front rotates, point $x = 1/5$ moves slower and lags behind point $x = 1/2$, while point $x = 4/5$ overtakes point $x = 1/2$. Also, as in the previous example, during most of the simulation time, when the velocity of the front is relatively large, both numerical approaches give indistinguishable curves. However, as the velocity drops with the front approaching the equilibrium position, the CutFEM-based method results in the front aligning with the nearest element edges. As the equilibrium position of the front is an inclined curve, while element edges are either vertical, horizontal or inclined by 45, the front acquires a stair-like shape. The remeshing procedure gives a smooth enough piecewise-linear representation of the equilibrium position. Although this is a noticeable drawback of the existing CutFEM-based approach, it can

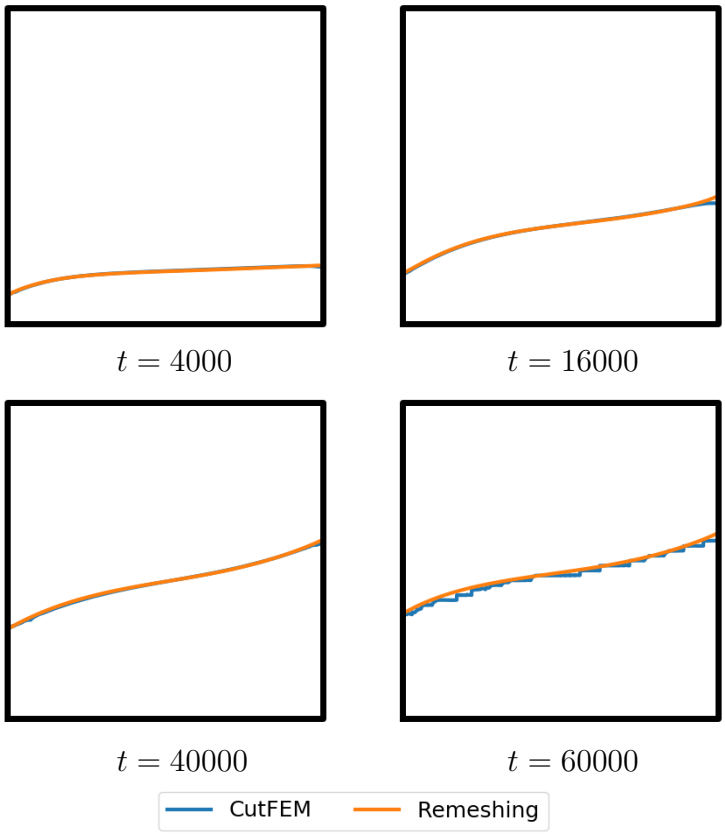

Fig. 3.18: Propagation of the initially planar chemical reaction front in a body under shear loading. The kinetics is illustrated by four snapshots of the reaction front at different times.

be clearly seen that the front position numerical error close to the equilibrium position has an order of an element size.

3.4.4 Closed interface in the square domain

The third example focuses on a different topology of the reaction front, namely a closed curve. In Section 2.4 cylindrical geometries were considered and a set of parameters leading to stable configuration of the circular reaction front have been established. In this section, the geometry is changed to a square, which creates inhomogeneous stress distributions (with respect to the polar angle in the polar coordinate system), and, therefore, leads to a more complex equilibrium configuration. Diffusing reactant is supplied trough the external boundaries and the initial position of the interface was a circle in the

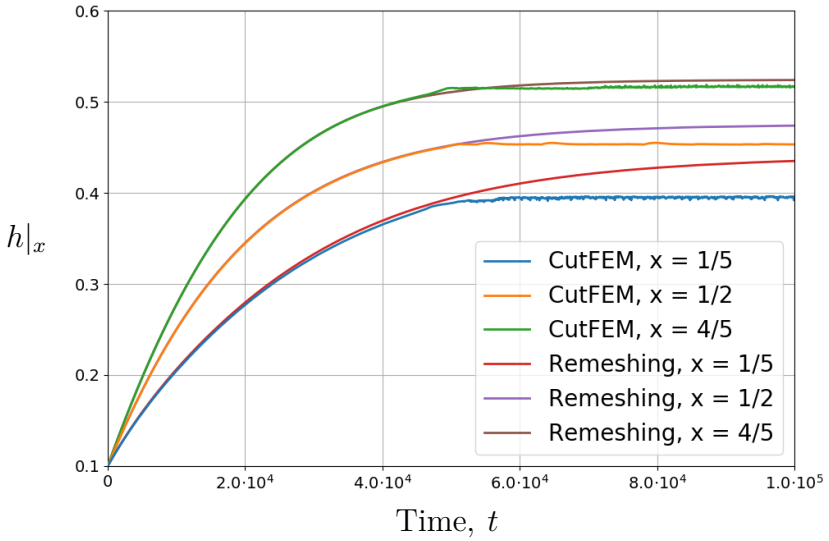

Fig. 3.19: Propagation of the initially planar chemical reaction front in a body under shear loading. The kinetics is illustrated by the evolution of y-coordinate of three points of the front.

center of this square. To highlight the effect of stresses on the equilibrium configuration of the reaction front, two different loading cases are considered: biaxial stretching and piece-wise linear prescribed displacement. The last one is chosen in a form

$$\begin{aligned} \mathbf{u}_0 &= a_0 \frac{2x}{L}\mathbf{e}_x + a_0 \frac{2y}{H}\left(1 + \left|\frac{2x}{L}\right|\right)\mathbf{e}_y, \quad \text{at } y = \pm\frac{H}{2}, \\ \mathbf{u}_0 &= \frac{2x}{H} a_0 \left(2 - \left|\frac{2y}{H}\right|\right)\mathbf{e}_x + 2a_0 \frac{2y}{H}\mathbf{e}_y, \quad \text{at } x = \pm\frac{L}{2}, \end{aligned} \tag{3.2}$$

where the origin of the coordinate system is assumed to be in the center of the square. Graphical interpretation of the loading scenarios is shown in Fig. 3.20.

Before the analysis it was assumed that change of the main domain from circular to square (to be precise, the solution domains are a square and circle, but the entities they are modeling are a prism and cylinder) would not change drastically neither position of the equilibrium interface nor its stability. Therefore, for material parameters, a stable set for cylindrical problem from Tab. 2.3 was used. The transformation strain was taken to be $\varepsilon = 0.05$. The same chemical and diffusion parameters were used as in the first example (Tab. 2.2), but with another value for the energy parameter $\gamma = 0.15$. For the diffusion problem, the mixed boundary conditions were prescribed on all

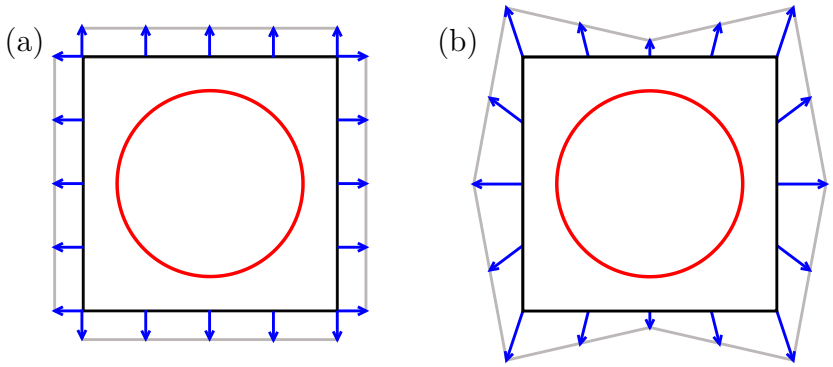

Fig. 3.20: Considered loading cases: biaxial stretching (a) and piecewise-linear prescribed displacement (b).

boundaries. For this example height and width of the square $H = L = 2$ are taken. The radius of the interface initial position is set to 0.73. External loading for biaxial stretching is applied to all the exterior edges and the amplitude is set to $u_0 = 0.076$. For the second loading case, the loading parameter a_0 in (3.2) is set to 0.025.

The initially circular configuration of the front evolves then into two different shapes for these two loading scenarios, which are Shown in Figs. 3.21 - 3.22.

As in the previous examples, during initial stage (fast kinetics) both methods produced indistinguishable results, therefore, the evolution of the reaction front is not shown. At the final stage, i.e. close to equilibrium configuration, the CutFEM-based method aligns with the element edges. Here, again, it is clearly seen that the discrepancy in the front position has an order of an element size.

For solving these problems time step of $\Delta t = 50$ is taken. For the CutFEM-based approach, spatial step of $\Delta x = 1/32$ was taken, for the remeshing approach the average size of element on the interface $\Delta x = 0.0116$ is taken for the biaxial stretching case and $\Delta x = 0.0077$ – for the second loading scenario. Cropped examples of the finite-element meshes are shown in Fig. 3.23 for the second loading case at time $t = 6100$ (Fig. 3.22).

All the three simulated examples reveal that both numerical procedures show qualitatively similar results. For the planar interface numerical simulations correlate with the analytical predictions. Moreover, both CutFEM and remeshing simulations shows same kinetic features for stable and unstable configurations.

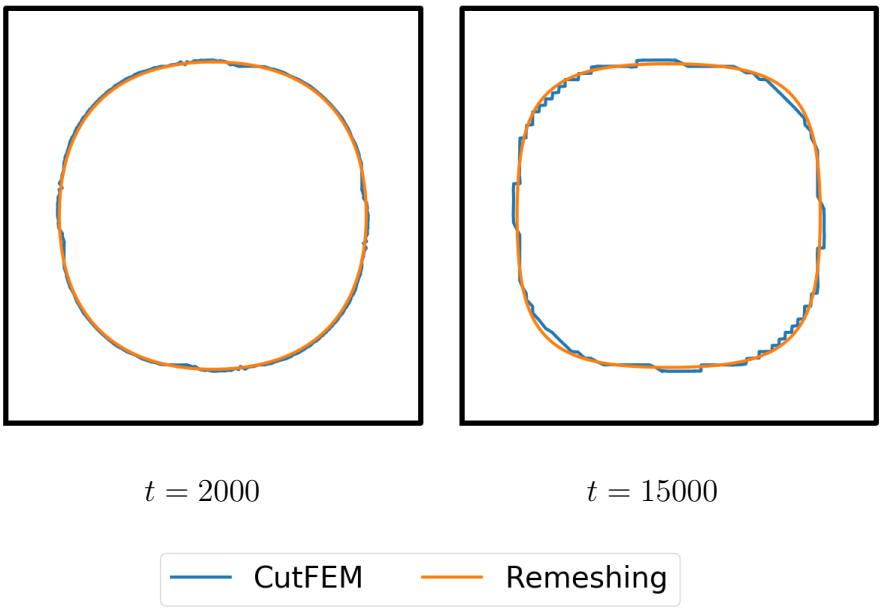

Fig. 3.21: Intermediate and final configurations of a closed-curve reaction front in a 2D body under biaxial stretching.

3.5 Kinetics of a chemical reaction front in a body with a pore or an inclusion

Another example where the influence of the mechanical stresses on the kinetics of the chemical interface can be clearly seen is a problem with the interface approaching some inclusion. In the current section, a chemical reaction in a finite layer with a cylindrical pore (or void) and with a cylindrical rigid inclusion is considered, Fig. 3.24.

The reactant is supplied through the lower boundary. Left and right edges are traction free. External displacements $\mathbf{u} = u_0 \mathbf{e}_y$ are applied to the upper boundary, and lower boundary is fixed. The material parameters used in the following numerical simulation are given in Tab. 2.1, the stable configuration is considered. Diffusion parameters are the same as in Section 3.4.2. For this particular problem $H = 1$, $L = 2$, the radius of the pore (or of the inclusion) is $r = 1$ and the initial thickness of the transformed layer is $h = 0.1$. An external displacement is set to $u_0 = 0.0453$.

Due to symmetry, only half of the model is considered. For both problems time step of $\Delta t = 80$ and spatial step of $\Delta x = 1/64$ are taken. The kinetics of the initially planar interface approaching the circular pore and solid inclusion

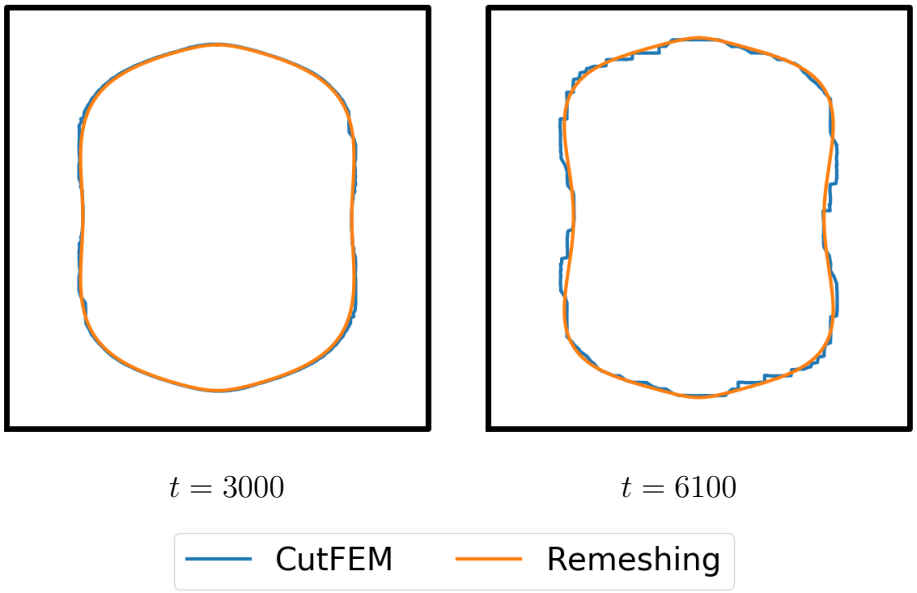

Fig. 3.22: Intermediate and final configurations of a closed-curve reaction front in a 2D body under complex loading.

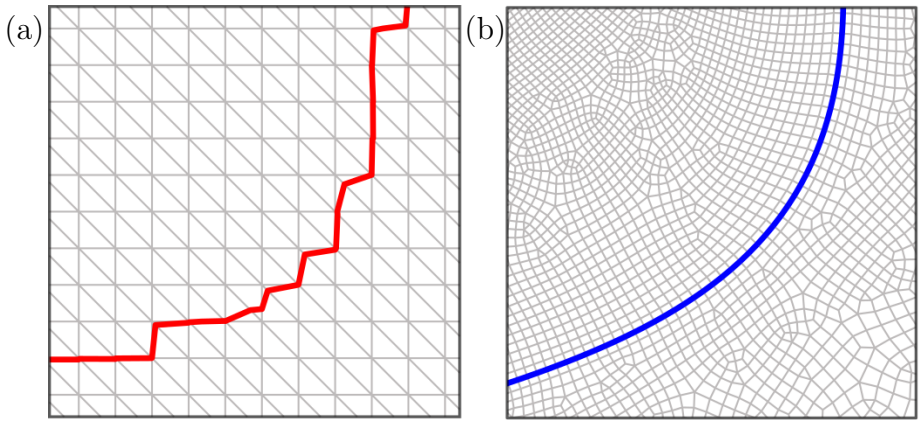

Fig. 3.23: Cropped examples of the finite-element meshes for final configuration of a of a closed-curve reaction front in a 2D body under complex loading. (a) – CutFEM results, (b) – remeshing results.

is shown in Fig. 3.25, (a) and (b), respectively. Similar setup for a uniform layer (without the pore and inclusion) is shown in Fig. 3.25 (c). Dashed lines correspond to intermediate positions of the interface at regular time intervals,

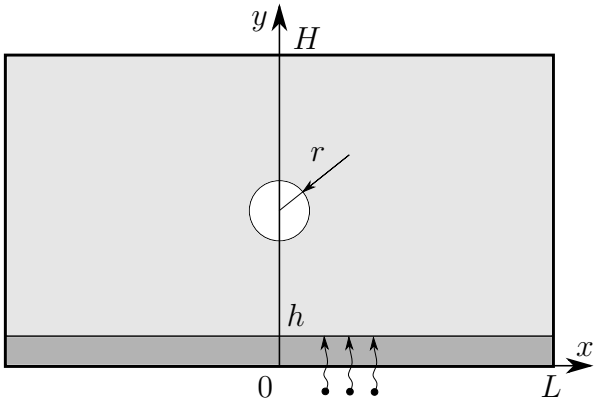

Fig. 3.24: Model for the finite layer with circular pore or inclusion.

which are equal to $20\Delta t$ for all plots. One can see that the void accelerates the front propagation, and the inclusion retards it.

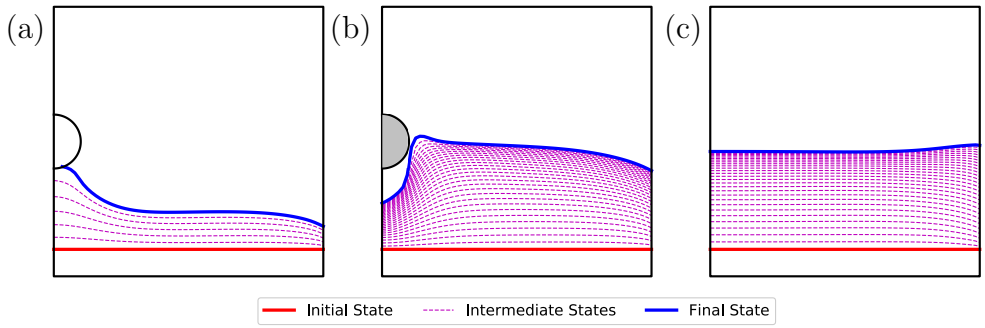

Fig. 3.25: Kinetics of the initially planar chemical interface in the vicinity of a cylindrical pore (a), a rigid inclusion (b), and in a uniform layer (c).

The distributions of the von Mises stress in the layer with a pore and with a rigid inclusion are shown in Figs. 3.26 and 3.27, respectively.

The experiments show that pores (or voids) or another material insertions may significantly influence the kinetics of the chemical reaction front propagation. As an outlook for further study of the interface passing through the region with inclusions, an additional procedure for adjusting the moved interface might be developed, similar to one described in Fig. 3.4.

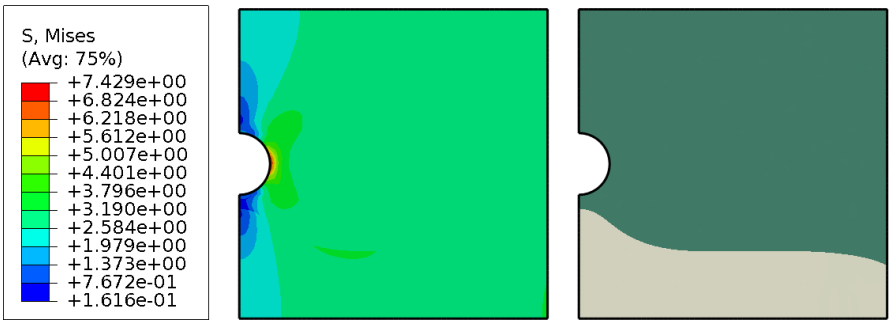

Fig. 3.26: The von Mises stress distribution in the vicinity of a pore for the reaction front position shown in the right inset.

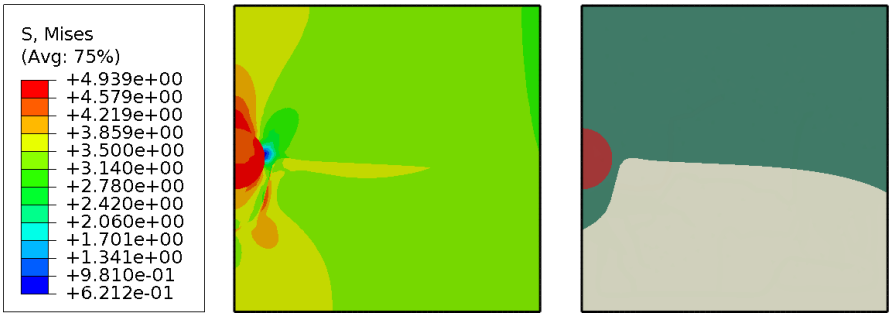

Fig. 3.27: The von Mises stress distribution in the vicinity of a solid inclusion for the reaction front position shown in the right inset.

3.6 Conclusions

An approach to study the influence of mechanical stresses on the chemical reaction front propagation based on the chemical affinity tensor concept was implemented in a numerical procedure.

From the correspondence of the analytical predictions and the results of finite element simulations, it becomes evident that the numerical procedure can be reliably used for the simulation of reaction and phase transformation front propagation and a stability check of the interface in thermodynamic equilibrium. The instability of the reaction front propagating towards the unstable equilibrium was simulated and analyzed for initial states with a not perfectly circular (or planar) interface by using the proposed numerical procedure. Also, it was shown numerically that growing perturbations in the case of unstable configuration may lead to plasticity and failure.

For the cylindrical interface, numerical simulations show that for the stable set of material parameters both round and perturbed initial interface smoothly

converge to the circular equilibrium position. For the unstable set of parameters two scenarios are realized:

(i). An initially round interface keeps its shape while propagating toward thermodynamic equilibrium. It can be concluded that the global kinetics of the reaction front interface suppresses the process of stability loss. When the interface approaches equilibrium, its velocity decreases, so that it becomes comparable with the growth speed of the instability amplitude. At this point, the shape of the unstable front becomes visible.

(ii). The amplitude of the initial perturbations of the interface grows with the front propagation toward equilibrium. Numerical simulations show that this process accelerates while the interface approaches equilibrium. Note that for the studied parameters of the initial front perturbations, the interface keeps the frequency of the predefined perturbations during its propagation.

The proposed procedure was compared with the CutFEM approach to model numerically the reaction front propagation. Both CutFEM and remeshing methods show the same kinetics of the reaction front when it is far from the equilibrium position. However, when the interface approaches the reaction blocking state, the CutFEM approach produces an artifact solution, in which the energy minimizing configuration forces the interface to align with the nearest element boundary. This issue can be resolved by introducing a more accurate procedure of calculating stresses at the interface, or by using the second-order finite elements. When compared with CutFEM, the remeshing procedure requires tracking the position of the interface, writing additional scripts to handle geometry- and self-intersections of the front. Nevertheless, both studied methods can be used to model the chemical reaction front kinetics.

A possible outlook for the remeshing procedure might be upgrading the method to the case of large deformations and non-linear material constitutive relations. This is already realized in CutFEM (Poluektov and Figiel [2019]), while the remeshing procedure is rather limited by the Abaqus software capabilities.

Having the remeshing procedure approbated and validated, it can be used to solve a real engineering problem.

4 Experimental and theoretical studies of Cu-Sn intermetallic phase growth

In this Chapter the growth of Inter-Metallic Compound (IMC) layers is considered: after soldering an IMC layer appears and establishes a mechanical contact between eutectic tin-silver solder bumps and Cu interconnects in microelectronic components. Intermetallics are relatively brittle in comparison with copper and tin. In addition, IMC formation is typically based on multi-component diffusion, which may include vacancy migration leading to Kirkendall voiding. Consequently, the rate of IMC growth has a strong implication on solder joint reliability. Experiments show that the intermetallic layers grow considerably when the structure is exposed to heat. Mechanical stresses may also affect intermetallic growth behavior. These stresses arise not only from external loadings but also from thermal mismatch of the materials constituting the joint, and from the mismatch produced by the change in shape and volume due to the chemical reactions of IMC formation. This explains why in this work special attention is being paid to the influence of stresses on the kinetics of the IMC growth.

This chapter starts with a report of experimental findings regarding the IMC growth at the interface between copper pads and tin based solder alloys in different microchips during a high temperature storage test. Then the growth kinetics is analyzed by means of a continuum model. By combining experiment, theory, and a comparison of experimental data and theoretical predictions the values of the diffusion coefficient and an estimate for the chemical reaction constant are found. A comparison with literature data is also performed. This chapter contains an overview of the results obtained in Morozov *et al.* [2018b]; Morozov *et al.* [2018a]; Morozov *et al.* [2020].

4.1 Overview on intermetallic compound growth

The main technological process for creating an electrical contact between components in a (micro-) electric circuit is soldering. Different eutectic tin-based alloys containing various metallic chemical elements (Zn, Bi, Pb, Ag, Cu, etc.) are used for this process. One of the most common lead free solder alloys in microelectronics is eutectic SnAg3.7 (or ternary SnAg3.6Cu0.8). This

alloy is also used in Ball-Grid Array (BGA) components in the microelectronic industry for solder bumps and paste (Lee and Mohamad [2013]).

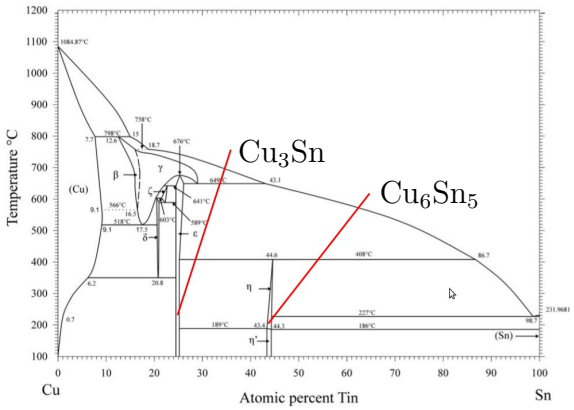

Fig. 4.1: Cu-Sn phase diagram, reprinted from Fürtauer *et al.* [2013].

An intermetallic, also known as an intermetallic compound, intermetallic alloy, ordered intermetallic alloy, and a long-range-ordered alloy is a type of metallic alloy that forms a solid-state compound exhibiting defined stoichiometry and ordered crystal structure, see, e.g., Callister Jr. and Rethwisch [2010]. In electric circuits Cu is used as a conductive material for contacting the surfaces of the electronic components. During soldering the solder material melts and gets in contact with the copper substrate so that a thin layer of a particular IMC forms at the interface between the Cu and the tin-based solder. In the absence of an IMC layer the bond between the solder and the substrate is weak, since there is hardly no interaction between the metals at the boundary. In Sn-Cu and Sn-Ag-Cu eutectic alloys the electrical and mechanical contact is established by one (Cu_6Sn_5) or two (Cu_6Sn_5 and Cu_3Sn) intermetallic phases, respectively (e.g., Liashenko, Gusak, and Hodaj [2014]). Their formation is determined by the temperature regime, according to the phase diagram shown in Fig. 4.1. It involves three stages: dissolving of Cu in liquid Sn, a chemical reaction between the components, and further crystallization. Further growth of the IMC layer takes place in the solid state. The formation of IMCs occurs according to the following chemical reactions between copper and tin

$$\begin{aligned} 6\,\mathrm{Cu} + 5\,\mathrm{Sn} &\rightarrow \mathrm{Cu_6Sn_5}, \\ 3\,\mathrm{Cu} + \mathrm{Sn} &\rightarrow \mathrm{Cu_3Sn}. \end{aligned} \tag{4.1}$$

Phase Cu_6Sn_5 is also referred to as the η and Cu_3Sn as the ε-phase.

As mentioned earlier, the existence of the IMC is a necessary condition for the electro-mechanical contact. However, when compared to pure copper or tin

the IMC is more brittle. This may lead to a decrease of the reliability of the joint. In addition, intense diffusion of Cu (from the pad) or Sn atoms through the IMC may lead to void formation due to the Kirkendall effect, see, e.g., Paul [2004]; Dybkov [2010].

There are many experimental studies of the IMC growth in solders of the aforementioned two and other phases of more complex stoichiometry (Kim, Huh, and Suganuma [2003]; Yu *et al.* [2005]; Min-Suk, Chan-Jin, and Hyuk-Sang [2008]), such as microrelief mapping of the interface, the determination of the chemical composition of the phases, or the influence of the soldering time on the kinetics of the IMC formation, *etc.* In these systems the growth velocities of the IMC interfaces are much higher than in homogeneously phased solders.

A typical empirical kinetic equation for the IMC phase growth is based on fitting the experimentally observed data and has the form (Cogan *et al.* [1984]; Dariavach *et al.* [2006]):

$$h = h_0 + kt^{1/n}, \tag{4.2}$$

where h and h_0 are the current and initial new phase thicknesses, t is the time, k and n are growth constants. Under the assumption that the major contribution to IMC growth is bulk diffusion, the power law (4.2) takes the form of a square root dependency (see, e.g., Gao *et al.* [2006]; Gao *et al.* [2019]). In other words, any deviation from the square root behavior indicates that not only bulk diffusion is governing the growth kinetics (Cogan *et al.* [1984]). In this case the growth constant k may be expressed through the diffusion coefficients, D, (Mei, Sunwoo, and Morris [1992]). The temperature dependence of the latter can be expressed by an Arrhenius equation,

$$D = D_0 \exp\left(-\frac{Q}{RT}\right), \tag{4.3}$$

where D_0 is a pre-exponential factor, Q is the reaction activation energy, R is the gas constant, and T is the absolute temperature in K, see, e.g., Ross, Vuorinen, and Paulasto-Kröckel [2016] and the references therein. Based on these ideas a model for intermetallic growth in thin Sn joints between Cu substrates was proposed in Arafat *et al.* [2020] with application to solder microjoints.

An understanding of the IMC formation process and predicting its kinetics in various range of temperatures is essential for evaluating the structural integrity of solder interconnects. The electrical current during operation of the microelectronic device can heat up a solder bump to 100°C - 150°C. This heat stimulates IMC growth and as a result reduces the lifetime of the joint.

4.2 Experiment overview

4.2.1 Specimen preparation

Two different types of microchips (referred to as Series I and II in Fig. 4.2 and in what follows) with BGA packages were available. The solder balls were approximately of the same diameter, 500μm. The frames of the microchips were made of plastic or metal for Series I or II, respectively.

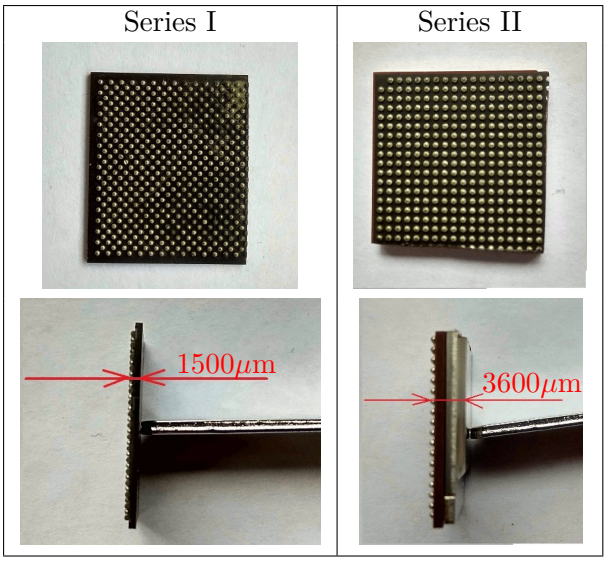

Fig. 4.2: Photos of the microprocessor boards.

For the commercially obtained packages the exact information about the solder material, the package substrate material, and its surface finish materials, as well the ball attachment process was not available. Clearly, all of this affects the initial IMC formation, as well as the diffusion processes during its growth. Therefore, in order to obtain a somewhat clearer picture, the following was assumed. According to performed EDXS (Energy-Dispersive X-ray Spectroscopy) analysis, no other elements were found in the IMC region apart from Cu and Sn. Hence it is fair to assume that the solder material was eutectic tin silver (AgSn), and the substrate had an OSP (Organic Surface Protection) coating. Moreover, note that the experimental work was carried out in order to validate the analytical model of IMC growth but not of its formation. The thickness of the IMC layers was measured before the heat treatment and used as an initial condition for the theoretical model.

In order to reduce the number of tests and still get a reliable statistical data, the experimental procedure to determine the kinetics of the IMC phase growth was organized as follows. Before the experiment each of two types of

microchips was dissected through an array of balls, as shown schematically in Fig. 4.3, (a). The cross-section was polished with 3 μm diamond polishing suspension. In order to track the interface propagation, two micro-indenter marks (Vickers method) were applied to each ball by a Buehler MicroMet 5103 microindentation hardness tester. These marks served as reference for tracking the IMC growth interfaces in the neighborhood, Fig. 4.3, (b). After the heat treatment and the EDXS analysis, the specimens were returned to the oven. The same cross-sections of the same solder balls were examined during the experiment. Note that only three balls per series were continuously monitored during the heat treatment, which was already quite time-consuming and operationally elaborate. In the curves below showing thickness of IMC over time an average of the observed growth for the three balls per series is displayed.

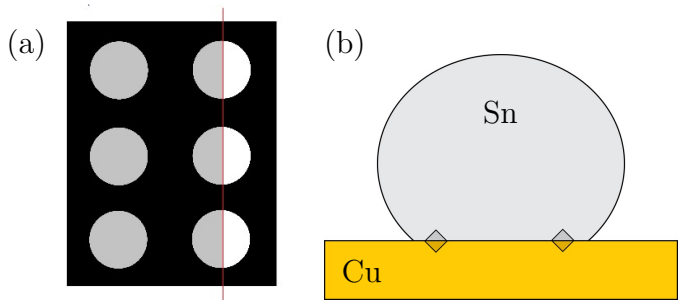

Fig. 4.3: Cutting scheme applied to the microprocessor.

The experimental procedure does not allow to fix the specimen in an epoxy casing. Indeed, the melting temperature of the plastic is higher than melting temperature of the solder material. However, the epoxy curing temperature is close to the experimental temperature of 150°C. Therefore, all polishing was performed "by hand," which resulted in a relatively rough polished surface. Nevertheless, the quality is fair enough to obtain the chemical interface kinetics data, which is the aim of this study. Figure 4.4 shows the initial cross-section of a solder ball. Differences in contrast correspond to different chemical composition.

4.2.2 Experimental procedure

In the current study the process of IMC growth is analyzed in microprocessors with BGA packages during a high temperature storage test. According to the JESD22-A103 specification this experiment was performed at 150°C in a vacuum oven over 1100 hours. The Series I ball was examined after 0, 120, 240, 360, 680, and 1000 h, and the Series II ball at 0, 120, 240, 360, 480, 800, and 1120 h, respectively. The chemical compositions were obtained from EDXS

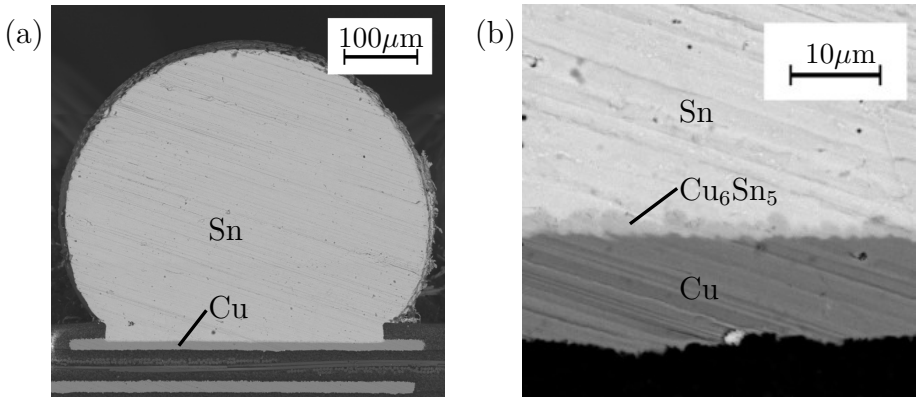

Fig. 4.4: Cross-sections of a solder ball from Series I before heat treatment, general view (a) and interface zone (b).

analysis performed on an Oxford Instruments INCA X-Max detector fitted on a MIRA 3 (TESCAN) microscope at voltage of 20 kV. The thickness evaluation was based on postprocessing of micrographs with Python scripts.

4.3 Experimental results

The results for the two series are qualitatively different even though the corresponding samples were heated and cooled under the same conditions. It is suspected that this is due to the different casings and the associated heat conduction properties: the thickness of the microprocessor case for Series I (plastic casing) was about 150 μm, and for series II (metal casing) about 360 μm. Due to differences in the case materials and their thicknesses for samples of series I and II, the true cooling rate down to room temperature could differ. Both series of specimens contain a plastic circuit board and BGA in their assembly. However, specimens from Series II have a additional metal framed microchip. Therefore, the cooling time for Series II specimens is longer than for specimens from Series I. The formation of IMC phases is a function of two competing processes, namely growth and dissolution, which in turn depend on the cooling rate. This could lead to the formation of various phases in microprocessors of various designs.

Fig. 4.4 (b) shows that an IMC layer forms at the copper-solder interface right after the attachment of solder balls on the microprocessor board copper substrates. A spectroscopic analysis showed that its composition corresponds to the compound Cu_6Sn_5. Note that the shape of the Cu_6Sn_5 layer has a comb-like structure (also referred to as scallops in the literature, e.g., Kim and Tu [1996]) for all of the studied samples. Its relief is governed by the

roughness of the copper substrate, and the initial average height in the samples was in the range 1.9 - 3.3 μm. In addition, the tetragonal crystal structure of Sn will result in an anisotropy of the diffusivity of the Cu atoms (Han *et al.* [2017]; Wang *et al.* [2020]). It was also shown that the relief depends on the crystalline structure of the underlying copper pad (Sunwoo, Morris, and Lucey [1992]; Sang, Du, and Ye [2009]; Suganuma [2003]), which can be fine-grained polycrystalline or even single-crystal based.

4.3.1 Chemical composition of the compounds

An EDXS analysis was performed at each stage of the experiment in order to obtain the composition of the materials observed through the microscope. The set of examined points for specimens from Series I after 1000 h heating is shown in Fig. 4.5 and the corresponding compositions are listed in Tab. 4.1. All results are given in at% (atom percent). One should note that for the composition 54.5 at% Cu and 45.5 at% Sn corresponds to Cu_6Sn_5 and the composition 75 at% Cu and 25 at% Sn to Cu_3Sn, respectively. From the analyzed data it follows that during heat treatment (up to 1000 h) the chemical composition (stoichiometric ratio) of the IMC remained constant and no other intermetallic compounds (e.g., $Cu_{10}Sn_3$ or $Cu_{41}Sn_{11}$) were detected.

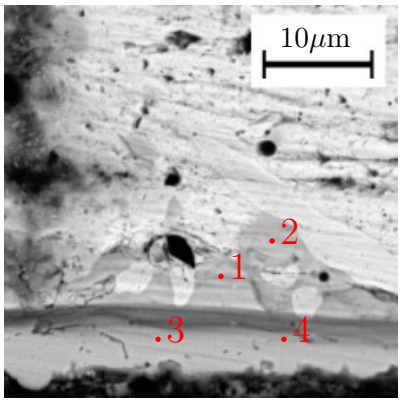

Fig. 4.5: First set of points from the interface region for EDXS analysis, a ball from Series I at $t = 1000$ h. The corresponding data is listed in Tab. 4.1.

Point	Cu	Sn
1	54.5	45.5
2	52.4	47.6
3	52.7	47.3
4	53.1	46.9
Average	53.2	46,8

Tab. 4.1: Data obtained from the EDXS analysis for the points in Fig. 4.5, values are given in at%.

The set of points for the EDXS analysis of the solder material and the Cu substrate of a specimen from Series I after 1000 h heating is shown in Fig. 4.6 and the results of the analysis are listed in Tab. 4.2. Points 1 and 2 in Fig. 4.6 are located in the copper substrate area. However, they contain 2.6 and 5.6 at% of Sn, respectively. Moreover, during separation of Sn atoms from Cu_6Sn_5

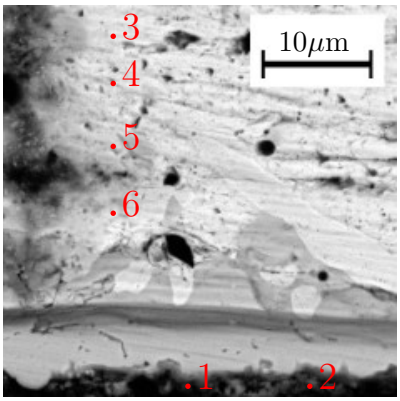

Fig. 4.6: Second set of points from the interface region for the EDXS analysis, a ball from Series I at $t = 1000$ h. The corresponding data is listed in Table 4.2.

Point	Cu	Sn
1	97.4	2.6
2	94.4	5.6
3	0.0	100.0
4	1.0	99.0
5	9.5	90.5
6	11.8	88.2

Tab. 4.2: Data obtained from the EDXS analysis for the points in Fig. 4.6, values are given in at%.

a reaction proceeds according to the following scheme:

$$Cu_6Sn_5 - 3\,Sn \rightarrow 2\,Cu_3Sn. \tag{4.4}$$

As a result of reaction (4.4) and according to the phase diagram in Fig. 4.1, a new Cu_3Sn IMC should then be formed at the Cu – Cu_6Sn_5 interface. However, in Series I this compound was not observed, possibly due to an extremely small thickness of the Cu_3Sn layer, which could not be detected.

The set of examined points for a specimen from Series II after 1120 hours heating is shown in Fig. 4.7 and the results of the chemical composition analysis are listed in Tab. 4.3.

It can be seen from Fig. 4.7 that, unlike Series I, there are no "islands" in the IMC layer and the boundaries of the layers show less roughness (comb-like structure). During heat treatment a composition of two IMC configurations was temporarily observed. However, at the later stages of the experiment (after 360 h) the Cu_3Sn phase vanished. The reason for this is unknown. In any case this phase is not so easy to detect. To quote from Ross, Vuorinen, and Paulasto-Kröckel [2016]: "However, it is well known that there is typically a thin layer of Cu_3Sn present between Cu and Cu_6Sn_5, which, immediately after reflow, is generally only measurable by transmission electron microscopy (TEM), although it can be resolved also by optical microscopy. Based on literature data, we estimate the thickness of the Cu_3Sn layer to be about 0.1 μm."

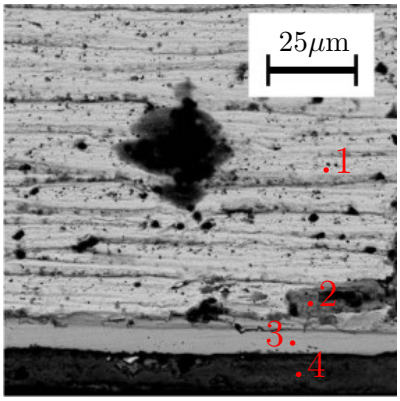

Fig. 4.7: Set of points from the interface region for the EDXS analysis a ball from Series II at $t = 1120$ h. The corresponding data is listed in Table 4.3.

Point	Cu	Sn
1	0.0	100.0
2	31.5	68.5
3	54.7	45.3
4	97.0	3.0

Tab. 4.3: Data obtained from the EDXS analysis for the points in Fig. 4.7, values are given in at%.

4.3.2 Thickness data for the IMC layers

In order to determine the characteristics of the growth kinetics of the intermetallic compounds a set of experiments was conducted using Series I and II BGAs when exposed to a constant temperature. For each series measurements were carried out as follows.

The heat treatment was performed at a constant temperature of 150 °C. Measurements of the thickness were done at the same location of 3 balls, namely near the micro-indenter mark. This procedure allows to track the thickness of the layers at certain points and to average between the balls obtained within each set of microprocessor BGAs.

As it was mentioned above, in the Series I balls only the Cu_6Sn_5 phase was detected. It is known from the literature that the formation of the Cu_6Sn_5 phase is largely determined by the diffusion processes of Cu, and the diffusion rate determines the thickness of the IMC layer (Schaefer, Fournelle, and Liang [1998]; Lee and Mohamad [2013]). Fig. 4.8 shows typical micrographs of a sample after 120 hours storage at a constant temperature of 150 °C.

By comparison of Figs. 4.4 (initial state) and 4.8 it follows that the thickness of the Cu_6Sn_5 layer significantly increased. The comb-structure of the IMC phase is preserved. Note that in one set of samples the thickness of Cu_6Sn_5 varies along the interface from 3.1 to 9.1 μm (in comparison, the initial layer thickness was 1.9-3.3 μm, i.e., it increased 2 - 3 times). A large dispersion of thickness, as well as a formation of IMC agglomerations, can be explained by uneven grain growth rate (Yu and Wang [2008]). Fig. 4.8 shows that there are

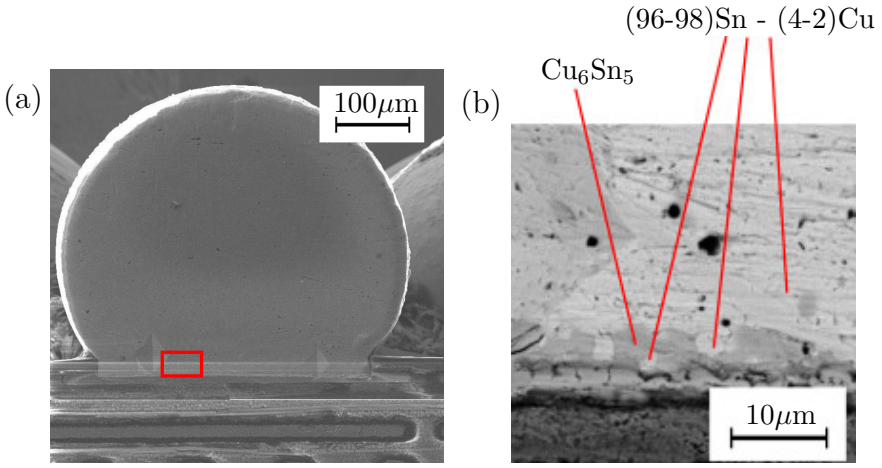

Fig. 4.8: Cross-section of a solder bump from Series I after $t = 120$ h heat treatment, general view (a) and enlarged region indicated by the red rectangle (b).

local border areas, "islands", in which the initial composition of the solder is preserved.

Intermetallic layers after 120 and 240 hours heat treatment are shown in Fig. 4.9 ((a) and (b), respectively). The approximate shape of the interfaces between the solder, IMC and the substrate is outlined by red color. One should note that the chemical composition of the IMC remains unchanged and the appearance of new crystalline phases was not detected. The intermetallic compound grows in both directions, toward the solder and toward the substrate. However, the growth rate of the latter is much less than the one on the solder side. From Fig. 4.9 it is also seen that the area of the "island" regions decreases with time, which indicates that the Cu_6Sn_5 grains grow in all directions and not only perpendicular to the copper interface.

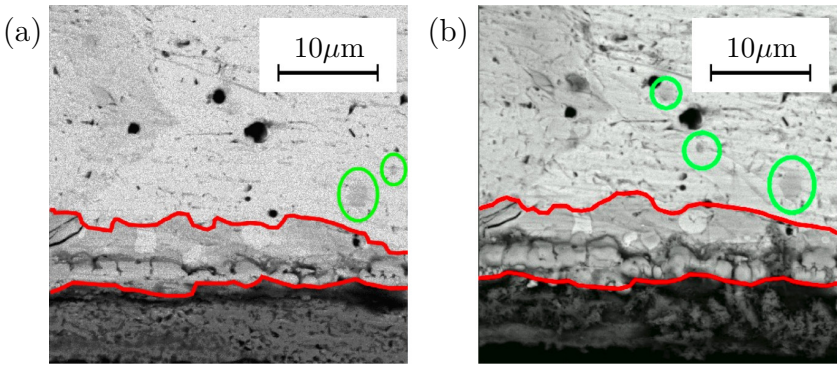

Fig. 4.9: IMC profiles in the solder bump from Series I after heat treatment: $t = 120$ h (a) and $t = 240$ h (b). Spheroids of Cu_6Sn_5 are marked with green.

The dark "island" in the solder area (marked by green color in Fig 4.9) are spheroids of Cu_6Sn_5 that formed by spalling from the IMC-solder interface (Liu *et al.* [1996]; Lee and Mohamad [2013]).

Both Sn and Cu_6Sn_5 islands are independent spheroids. It is most likely, that if more material is polished from the surface of the specimen, these spheroids will vanish. Therefore, since these areas do not really belong to the interface, they are not considered, i.e., neither added nor subtracted during further evaluation of the IMC phase thickness.

With further heat treatment a consistent increase in the thickness of the IMC layer is observed. Fig. 4.10 shows the interface profiles at treatment times 360, 680 and 1000 h. It can be seen that the formation of a locally thick intermetallic layer occurs. When comparing Fig. 4.10 (a) and (c), it follows that the areas of the solder "islands" slightly increased upon heat treatment. This could be explainable by surface effects after to the initial cut so that material might have moved out of plane and was then removed during polishing.

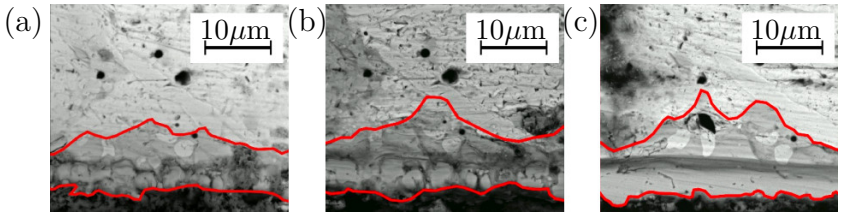

Fig. 4.10: IMC profiles in a solder bump from Series I after heat treatment: $t = 360$ h (a), $t = 680$ h (b) and $t = 1000$ h (c).

Microphotographs for the Series II specimen are shown in Fig. 4.11 for times from 0 h up to 120 h. One should note that for this series the thickness of the IMC layer was less planar than for Series I. The initial thickness of the Cu_6Sn_5 phase varied from 1.7 to 4.0 μm.

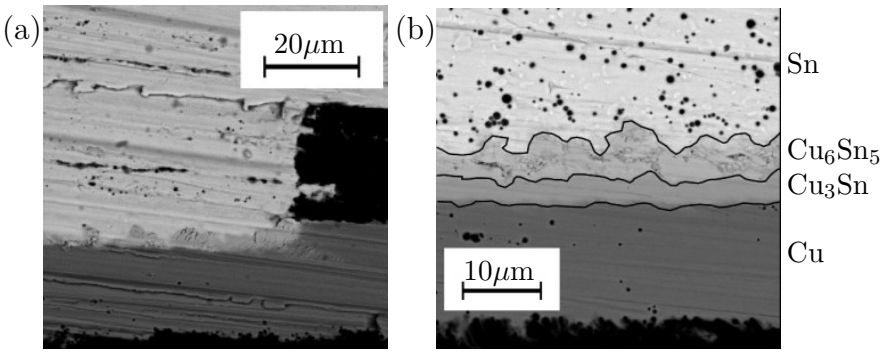

Fig. 4.11: Cross-section of a solder ball from Series II in the interface region before treatment at $t = 0$, (a), and after treatment, $t = 120$ h, (b).

As shown in Fig. 4.11 (b), two intermetallic phases formed after treatment: Cu_6Sn_5 and Cu_3Sn. This is different from the result obtained for balls of Series I. As it is known from the literature the formation of Cu_3Sn occurs on the interface between the copper substrate and the Cu_6Sn_5 compound. The following chemical reaction describes its formation (Hu and Ke [2014]):

$$Cu_6Sn_5 + 9\,Cu \rightarrow 5\,Cu_3Sn. \tag{4.5}$$

Despite storing in a vacuum oven, oxides and other compounds formed on the surface of the specimens cross-section. This made it hard to evaluate the exact thickness of the Cu_6Sn_5 layer for specimens of Series II at time $t = 480$ h, since part of the layer was covered with other materials ("oxidation dirt"), see Fig. 4.12.

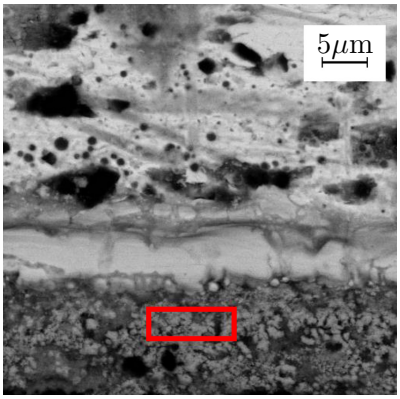

Fig. 4.12: Cross-section of the interface region in a ball from Series II after 480 h heat treatment. The chemical composition of the marked area obtained by the EDXS analysis is given in Tab. 4.4.

Element	Average, at %
C	20.57
O	4.62
Si	0.33
Cl	0.47
Cu	70.62
Sn	3.39

Tab. 4.4: Results of the EDXS analysis of the marked area in Fig. 4.12.

The EDXS analysis shows the presence of 4.62% oxygen in the region where only Cu is expected (see points 1 and 2 in Fig. 4.6, or point 4 in Fig. 4.7). To remove the dirt cover an additional polishing was carried out. In the following results, for this particular measurement, the thickness of the only visible IMC layer is presented. However, this measurement is excluded during the analysis for validation of the theoretical model. The thickness of the polished layer can be estimated from Fig. 4.13, which shows the IMC interface profiles of Series II microchips at the same spot at time $t = 800$ h (a) and $t = 1120$ h (b). Therefore the thickness of the removed layer is not greater than 10 μm.

In order to get statistical data about the thickness of the IMC all micrographs were postprocessed with Python scripts. The positions of one interface were

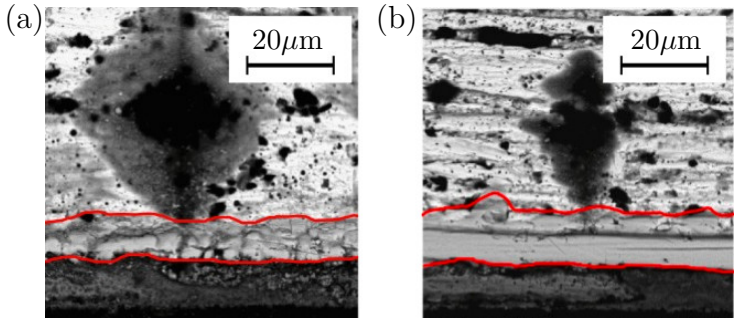

Fig. 4.13: Cross-section of the IMC profile in a solder bump from Series II after heat treatment: $t = 800$ h (a) and $t = 1120$ h after additional polishing (b).

subtracted from the other along the specimen. The mean value was chosen as the current thickness and the standard deviation was calculated in order to obtain an error estimate.

Results for Cu_6Sn_5 in Series I and II specimens are shown in Fig. 4.14. Due to the uneven growth of the IMC layer and its comb-like shape, the standard deviation from the mean value increases in time.

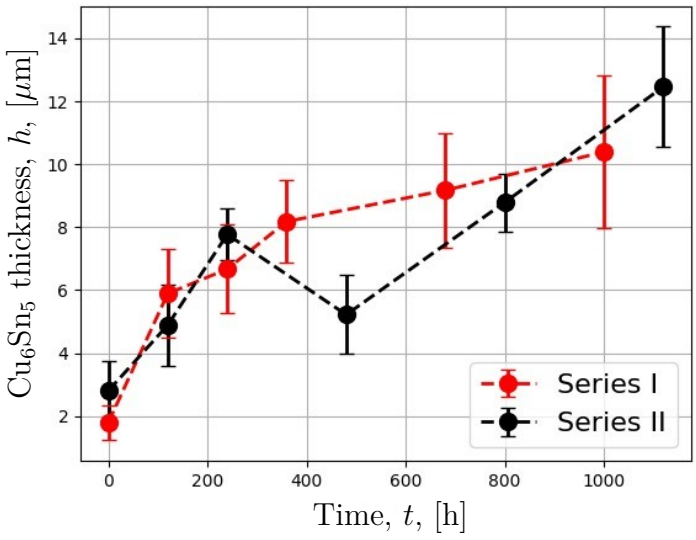

Fig. 4.14: Growth of the mean thickness of Cu_6Sn_5 phase for the specimen from Series I and II. Experimental points are connected by dashed lines for visual clarity only.

The IMC type Cu_3Sn was observed only in Series II specimens and even then only for a limited time period. The change of its thickness is shown in

Fig. 4.15. Thus, during annealing for more than 480 hours, the Cu_3Sn phase dissolved, but the mechanism of this process is not understood.

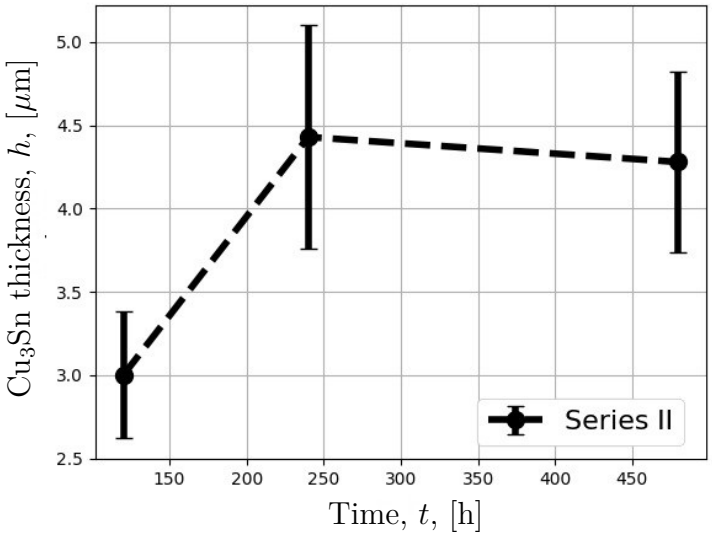

Fig. 4.15: Growth of the mean thickness of Cu_3Sn for the specimens from Series I and II. Experimental points are connected by dashed lines for visual clarity only.

4.4 Theoretical model

One of the aims of this work is to validate and quantify the model of reaction front kinetics described in Section 2.1 on the basis of the experimental results for the IMC growth.

4.4.1 Analytical solution of a model problem

As mentioned in the previous sections, only the Cu_6Sn_5 intermetallic phase was detected at all stages of the experiment. Therefore, for simplicity of the further analytical analysis, only this IMC is considered. It was pointed out that the interface between Cu_6Sn_5 and Sn moves much faster than one between Cu_6Sn_5 and Cu. Therefore, it is also assumed that only the interface between the IMC and the Sn is moving. The maximal thickness of the IMC layer observed in the experiment was about 15μm (Fig. 4.14) which is much less than the diameter of the solder ball (approx. 500μm, see Fig. 4.4). The above gives a reason to consider a simple boundary value problem of mechanochemistry with a planar chemical reaction front propagating in an infinite layer. Similar plane

problems for moving interfaces have been previously studied analytically and numerically, see, e.g., Freidin *et al.* [2016]; Morozov *et al.* [2018a]; Morozov *et al.* [2018b] and also in the previous chapters of this manuscript.

Due to the experimental setup, the cross-sections of the specimens were stress free surfaces during the whole experiment. The chemical reaction front propagation was observed at these stress free surfaces. Strictly speaking, one cannot use neither a plane strain nor a plane stress simplification in order to find the stresses at the reaction front. Nevertheless, since one can find a kinetic equation for the interface movement for both plane stress and plane strain formulations in a closed form, the model problem is solved in this work in both formulations, assuming that the real behavior may be somewhat "in-between." This gives the opportunity to fit the theoretical prediction with the experimental results, as described in the next Section 4.4.2. Based on the fitted data, an estimate is obtained for the diffusion coefficient and for the chemical reaction kinetic constant.

Consider an elastic layer with a cross-section in the xy-coordinate plane and the plane reaction front propagating in the y-direction from $y = 0$ to $y = H$ where H is the layer thickness and h is the current reaction front position (Fig. 4.16). The storage temperature in the oven is T and the reference temperature is T_0, $\theta = T - T_0$.

Assume that, by boundary conditions, the upper side of the layer is traction-free, then

$$\sigma_y^-|_{y=H} = 0, \tag{4.6}$$

and the lower side is fixed, then the displacement $\mathbf{u}_+|_{y=0} = 0$. Assume that the displacement is zero in x-direction: $u_x^\pm = 0$ and, thus,

$$\varepsilon_x^\pm = 0. \tag{4.7}$$

The displacement and traction continuity conditions at the reaction front will give, in particular, the continuity of y-components of the displacement vector and the stress tensor:

$$[\![u_y]\!]_{y=h} = 0, \quad [\![\sigma_y]\!]_{y=h} = 0. \tag{4.8}$$

The plane strain or the plane stress conditions are $\varepsilon_z^\pm = 0$ or $\sigma_z^\pm = 0$, respectively. The equilibrium equations and boundary and interface conditions in both plane statements will be satisfied for zero non-diagonal components of stress and strain tensors, that is why these components are not mentioned above. The displacement continuity condition at the reaction front also demands continuity of ε_z, which strictly speaking is not fulfilled in the plane stress formulation, but the input of this formal incompatibility is neglected.

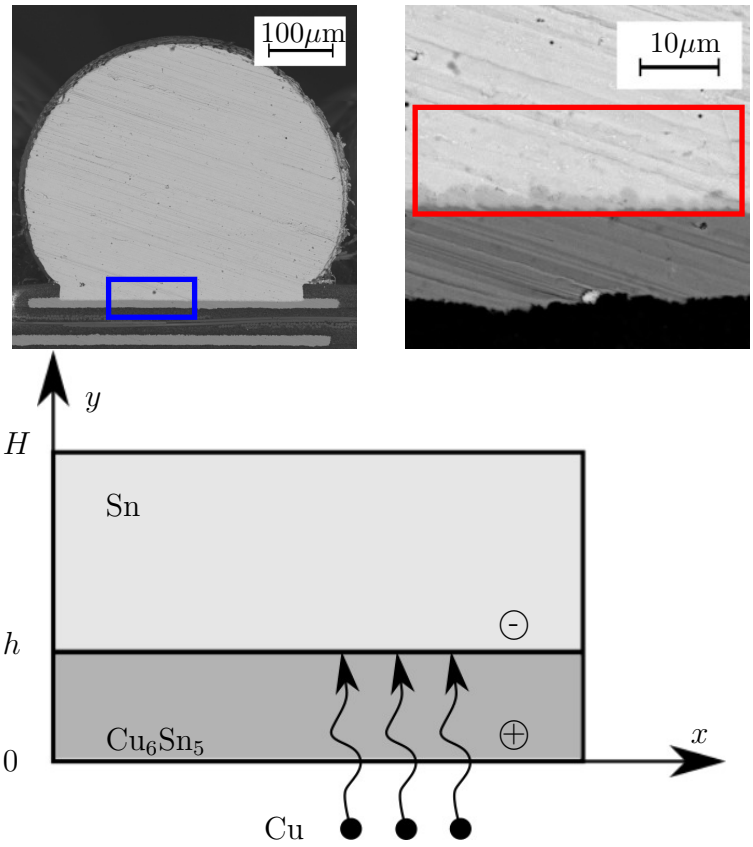

Fig. 4.16: Model description.

By constitutive equations (2.7),

$$\varepsilon_x^{\pm} - \alpha_{\pm}\theta - \varepsilon_{\pm}^{\mathrm{tr}} = \frac{1}{E_{\pm}}\left(\sigma_x^{\pm} - \nu_{\pm}(\sigma_y^{\pm} + \sigma_z^{\pm})\right), \tag{4.9}$$

where $E_{\pm}$ and $\nu_{\pm}$ are the Young's moduli and Poisson's ratios of the materials $B_{\pm}$, $\varepsilon_{-}^{\mathrm{tr}} = 0, \quad \varepsilon_{+}^{\mathrm{tr}} \equiv \varepsilon^{\mathrm{tr}}$. The formulas for $\varepsilon_y^{\pm}$ and $\varepsilon_z^{\pm}$ follow from (4.9) by cyclic permutations of x, y, and z.

Substituting strains and stresses found from (4.9) by using the conditions (4.6) – (4.8) and by taking into account all constraints regarding plane strain and plane stress formulations into (2.14), one can obtain that the contribution χ in A_{nn} does not depend on the front position, and

$$\chi = \begin{cases} \gamma + \dfrac{1}{2}E_{-}\alpha_{-}^2\theta^2 - \dfrac{1}{2}E_{+}(\alpha_{+}\theta + \varepsilon^{\mathrm{tr}})^2, & \text{plane stress,} \\ \gamma + \dfrac{E_{-}}{1-\nu_{-}}\alpha_{-}^2\theta^2 - \dfrac{E_{+}}{1-\nu_{+}}(\alpha_{+}\theta + \varepsilon^{\mathrm{tr}})^2, & \text{plane strain.} \end{cases} \tag{4.10}$$

Then, by (2.5), the reaction rate becomes equal to

$$\omega_n = k_*(c - \kappa c_*), \tag{4.11}$$

where the stoichiometric coefficient n_* is renormalized to one with respect to all other stoichiometric coefficients, as shown in Chapter 2.1, and κ is defined as

$$\kappa = \exp\left(-\frac{n_- M_-}{\rho_-}\,\frac{\chi}{RT}\right). \tag{4.12}$$

Diffusing Cu atoms are supplied through the lower side $y = 0$ and the formation of the intermetallic phase occurs at the interface between Cu_6Sn_5 and Sn at $y = h$. The diffusion equation takes the form

$$\frac{\mathrm{d}^2 c}{\mathrm{d}y^2} = 0, \quad y \in [0, h] \tag{4.13}$$

with the boundary conditions

$$\begin{aligned} D\frac{\mathrm{d}c}{\mathrm{d}y}\bigg|_{y=h} + \omega_n = 0, \\ D\frac{\mathrm{d}c}{\mathrm{d}y}\bigg|_{y=0} + a(c_* - c(0)) = 0, \end{aligned} \tag{4.14}$$

where ω_n is given by (2.5).

The solution of the diffusion problem finally gives the concentration at at the reaction front as a function of the reaction front positon

$$c|_{y=h} = c_* \frac{1 + \kappa\left(\dfrac{k_*}{a} + \dfrac{k_* h}{D}\right)}{1 + \dfrac{k_*}{a} + \dfrac{k_* h}{D}}. \tag{4.15}$$

Then the reaction rate takes a form of the dependence of the front position

$$\omega_n = \frac{k_* c_* (1 - \kappa)}{1 + \dfrac{k_*}{a} + \dfrac{k_* h}{D}}. \tag{4.16}$$

Substitution of the expression (4.16) of the reaction rate into the formula (2.6) for the interface velocity results in the explicit equation for the dependence of the front position on time:

$$\frac{\mathrm{d}h}{\mathrm{d}t} = \frac{n_- M_-}{\rho_-}\,\frac{k_* c_* (1 - \kappa)}{1 + \dfrac{k_*}{a} + \dfrac{k_* h}{D}}. \tag{4.17}$$

Integration yields an explicit dependence of time on the front position:

$$t(h) = \frac{\frac{1}{2}\frac{k_*}{D}(h^2 - h_0^2) + \left(1 + \frac{k_*}{a}\right)(h - h_0)}{\frac{n_- M_-}{\rho_-} k_* c_* (1 - \kappa)}, \tag{4.18}$$

where h_0 is the initial thickness of the IMC layer appeared just after the solder bump attachment.

The dependence (4.18) be rewritten in the standard form of the parabolic law

$$h(t) = \sqrt{C_1 t + C_2} + C_3, \tag{4.19}$$

where

$$\begin{aligned} C_1 &= 2D\frac{n_- M_-}{\rho_-} c_*(1 - \kappa), \\ C_2 &= \left(h_0 - D\left(\frac{1}{k_*} + \frac{1}{a}\right)\right)^2, \\ C_3 &= -D\left(\frac{1}{k_*} + \frac{1}{a}\right). \end{aligned} \tag{4.20}$$

Note that the parameters k_* and a occur in (4.20) only in a combination of the sum of the inverse values. Note also that the influence of mechanical actions is represented by the parameter κ, which is constant in the considered case. External mechanical loading may lead to the dependence κ on the front position, which would affect the front behavior.

The parabolic law (4.19) will be used in the next section for fitting parameters to experimental data.

4.4.2 Fitting the model parameters

The mechanical properties of Cu, Sn and corresponding IMCs can be found in the literature. Young's modulus, Poisson's ratio, and the coefficient of thermal expansion are listed in Tab. 4.5 (Yang *et al.* [2008]; Jiang *et al.* [1997]). Molar masses and densities are given in Tab. 4.6 (Sun and Yin [2009]).

Material	E, GPa	ν	α, K^{-1}
Sn	50	0.36	$22 \cdot 10^{-6}$
Cu_6Sn_5	118	0.31	$18 \cdot 10^{-6}$

Tab. 4.5: Mechanical material properties used in the model, Yang *et al.* [2008]; Jiang *et al.* [1997].

The solubility of Cu in the IMC is defined as the maximum achievable concentration of copper in a Cu_6Sn_5 lattice. According to the phase diagram in

	Sn	Cu	Cu_6Sn_5	Cu_3Sn
ρ, g/cm^3	7.280	8.960	8.280	9.140
M, g/mol	118.7	63.55	974.8	309.3

Tab. 4.6: Molar masses and densities used in the model, Sun and Yin [2009].

Fig. 4.1 two stable phases can appear in the IMC at $T = 150^{\circ}$C: Cu_6Sn_5 and Cu_3Sn. By the reaction (4.5) the phase Cu_3Sn forms when one mole of Cu_6Sn_5 reacts with nine moles of Cu. Therefore it is estimated that the maximum amount of copper which can be dissolved in Cu_6Sn_5 is nine moles of Cu per one mole of the IMC. In addition, here it is assumed that diffusing atoms of Cu do not change the volume of the IMC. Hence, with the aforementioned assumptions and based on the general definition of molar concentration, $c_* = 9\,\rho_{Cu_6Sn_5}/M_{Cu_6Sn_5} = 76 \times 10^{-6}$ mol/mm^3 was computed for the reference value.

As mentioned earlier, the chemical energy parameter γ in (4.10) is determined by the Cu_6Sn_5 formation energy. This energy is defined empirically. The dependence of this energy on temperature in operating temperature range can be approximated by (Huang *et al.* [2015])

$$\Delta G = -7747.65 - 0.371T \quad [\text{J/mol}], \tag{4.21}$$

where T is taken in K. In order to calculate γ, the formation energy has to be divided by the molar volume $V_{Cu_6Sn_5} = 11.28\,\text{cm}^3/\text{mol}$ (value from Sobiech *et al.* [2011]), since γ unit is an energy density per unit volume.

By (2.11), for the reaction (4.5) between Sn and Cu the ratio of volumes one can find $J_{\text{tr}} = 1.44$ (44% volume expansion) if $\xi = 0$ (solid skeleton approach) and $J_{\text{tr}} = 0.92$ (8% volume shrinkage) if $\xi = -1$. The question about the value of the transformation strain accompanying IMC formation remains open and estimates of the relative volume change are in the range from -10%, (e.g., Mei, Sunwoo, and Morris [1992]; Lee and Lee [1998]; Bordere *et al.* [2018]) up to $+44\%$, (e.g., Jadhav *et al.* [2010]; Chudnovsky [2017]). Further the model parameters are fitted for $\xi = -0.5$, which corresponds to volume ratio $J_{\text{tr}} = 1.18$. In particular, such a value of deformation may be consistent with a small strain approach used in the modeling.

Certain material and chemical parameters remain unknown, namely D, k_*, a. In order to get an estimate for these values one can try to fit the square root curve, Eq. (4.19), constraining the parameters such that physically acceptable values for D and k_* will result. The fitting process was performed by using the weighted least square method, where the weights of the points depended on their estimated error.

It should be noted that the equations proposed in Section 2.1 for the chemical

reaction front kinetics represent the velocity of the interface in the initial, undeformed configuration, while the micrographs track the position of the interface in the current, deformed configuration. Therefore, before fitting, the analytical curve and the experimental points were transferred to the initial configuration, by multiplying by the corresponding transformation strain value.

The fitting curves for Series I and II specimens are shown in Fig. 4.17 and Fig. 4.18, respectively.

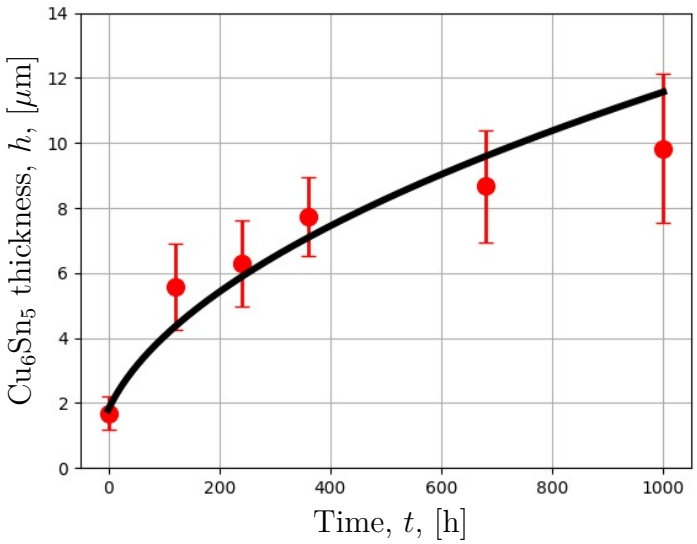

Fig. 4.17: Fitted square root dependence (4.19) for Series I specimens.

As it was noted in Section 4.2, the specimens of Series II were covered with oxides and other compounds at time $t = 480$ h so that a polishing procedure was required. Therefore it is not surprising that the measured thickness of the IMC layer at that data point departs from the general pattern, Fig. 4.18, and contains an error that is hard to assess. Because of that the data point was excluded from the fitting curve procedure.

Then the unknown material parameters D, k_*, a can be calculated from (4.20). As it was noted, the kinetic parameter k_* and the mass transfer coefficient a appear only in combination, so they cannot be resolved uniquely. Found values of D and the combination $(1/k_* + 1/a)$ are shown in Tab. 4.7.

In Yuan *et al.* [2015] diffusion coefficients of Cu in the IMCs were calculated based on the measured composition profiles of the diffusion zones within the temperature range of 130°C – 200°C. The authors showed that the diffusion coefficient depends highly on temperature, stating that $D = 0.38 \times 10^{-17}\mathrm{m}^2/\mathrm{s}$ at $T = 130°\mathrm{C}$, $D = 9.5 \times 10^{-17}\mathrm{m}^2/\mathrm{s}$ at $T = 150°\mathrm{C}$ and $D = 60 \times 10^{-17}\mathrm{m}^2/\mathrm{s}$ at

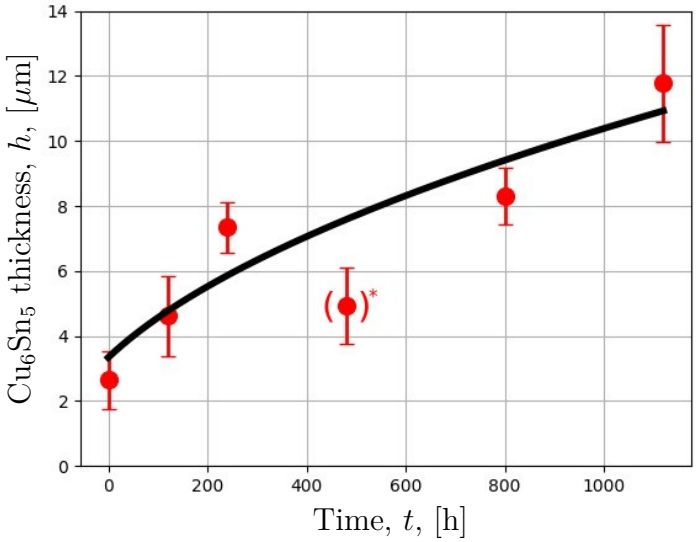

Fig. 4.18: Fitted square root dependence (4.19) for Series II specimens. The point marked with asterisk was excluded from the fitting procedure due to bad surface condition of the specimen.

Parameter	Formulation	Series I	Series II	Average
D, [m^2/s] $\times 10^{-17}$	plane stress	2.1	1.5	1.8
	plane strain	6.4	4.8	5.6
$1/k_* + 1/a$, [s/m] $\times 10^{-7}$	plane stress	89	57	73
	plane strain	28	18	23

Tab. 4.7: Estimated diffusion coefficient for two series of specimens.

$T = 170^{\circ}$C. Keeping this in mind, one can conclude that obtaining the result of the same order of magnitude can be considered as a good agreement. A comparison of the diffusion parameters, averaged from the two experimental results, with other works is shown in Tab. 4.8.

	[1]	[2]	[3]	[4]	This work	
					plane stress	plane strain
D [m^2/s] $\times 10^{-17}$	1.5	5.64	1.82	9.5	1.8	5.6

Tab. 4.8: Comparison of the obtained estimation of the diffusion coefficient with literature data. [1] - Onishi and Fujibuchi [1975], [2] - Paul, Ghosh, and Boettinger [2011], [3] - Kumar, Handwerker, and Dayanada [2011], [4] - Yuan *et al.* [2015].

Both values of diffusion coefficients obtained in this work (basing on plane stress and plane strain formulations) correlate with the data from various papers and can be used as a reference for more complicated models based on the chemical affinity tensor concept. These models can be extended since large strains are involved and non-linear anisotropic materials as well.

4.5 Conclusions

A high-temperature storage test was carried out for two groups of microchips with eutectic SnAg solder ball grid arrays. The specimens were cut and polished before the heat treatment. The growth of the intermetallic phase was examined by using the same set of solder balls through the entire experiment. The proposed experimental procedure allowed to determine IMC growth kinetics analyzing the small set of specimens. With the use of microindenter marks a relative movement of the IMC interfaces and change of layer thickness were obtained. This in turn lead to the evaluation and quantification of the kinetics of intermetallic growth.

The growth of the Cu_6Sn_5 intermetallic compound was modeled analytically based on the chemical affinity tensor concept and by taking a temperature dependence into account. The experimental results were used to determine the kinetic parameters in the chemical affinity tensor model for the first time. The simplest model of infinitely wide layers of linear elastic solids was analyzed and a theoretical prediction of the growth kinetics was obtained. The influence of mechanical stresses on IMC growth was taken into account. By comparison of the experimental data with the theoretical model the values of the diffusion coefficient and of the chemical reaction constant were estimated. The obtained diffusion coefficients correlate with the results from works of other researchers. The kinetic parameters of the model can now be used as reference values for more general cases with the kinetic equation based on the chemical affinity tensor.

In work Morozov *et al.* [2018b] the influence of the temperature regimes, in particular temperature cycling, is studied numerically. The change in temperature has a triplicate effect on the IMC growths kinetics: (i) as a source of the shear load, (ii) through thermal stresses in the solder bump, and (iii) through the chemical energy. Numerically it was shown that under all these conditions the IMC growth might go non-uniformly. However, the analysis was performed only with approximately estimated diffusion constants and reaction parameters, because the experiment from this chapter was carried out much later. An essential outlook for current work would be a recalculation of the old results with the new data given in this chapter.

5 Conclusions

In this work coupled problems of mechanochemistry were considered, namely the stress-affected kinetics of a chemical reaction front propagation in solids. A coupling of mechanical stresses, diffusion, and chemical reactions was comprehensively investigated: analytically, numerically, and experimentally. The main results of the thesis are as follows:

(i) A numerical procedure was developed and verified for simulating the chemical reaction front propagation in elastic solids;

(ii) The analytical procedure for a linear stability analysis of an equilibrium phase interface was extended to the case of a chemical reaction front. The stability of the propagating reaction front was studied numerically for cases of stable and unstable thermodynamic equilibrium interface positions;

(iii) The competition between the global kinetics of the interface propagation and the local kinetics of interface perturbations was demonstrated in the case of an unstable equilibrium interface position;

(iv) A high-temperature storage test was carried out for microchips with eutectic SnAg solder ball grid arrays. Based on the experimental results, diffusion and reaction kinetics parameters for the case of intermetallic growth in the context of the chemical affinity tensor concept were obtained for the first time.

The problem of chemical interface propagation was modeled based on the chemical affinity tensor concept. This concept allows studying the influence of mechanical stresses on the kinetics reaction front propagation based on fundamental thermodynamic principles. A number of problems were solved analytically and numerically. It was demonstrated that the stresses (which arise from external loading, due to the chemical transformation strains, etc.) could accelerate, retard, or even block the reaction front.

One of the main aims of the present work was developing a stability analysis procedure for chemical reaction fronts. This was motivated by the following reasons. The supply of the diffusing reactant governs the chemical reaction. Therefore, the reaction front may be forced to propagate towards the unstable equilibrium position. The growing instabilities may lead to plasticity and failure.

For the stability study a linearized perturbed boundary value problem was formulated and solved analytically for two cases, namely planar and cylindrical interfaces.

Even for these simple geometries the solution of the moving chemical interface problem and especially the stability analysis might be complicated. Therefore, a numerical procedure was developed using FEM for simulations of the chemical reaction front propagation. The implementation of the procedure was accomplished with the aid of the commercial FE software Abaqus. The used method was verified by the analytical solutions for various problems of chemical reaction front propagation. The proposed numerical procedure was verified by comparison with the analytical predictions and also compared and cross-verified with CutFEM and IGA-based procedures. It was shown that the used numerical procedure can adequately reveal physical stability and instability. The verified numerical procedure allowed to simulate the chemical reaction front kinetics when it approached stable or unstable equilibrium. Numerical simulations allowed to observe the competition between global and local kinetics of the chemical interface.

Many material, diffusion, and chemical reaction parameters have to be defined in order to model the reaction front propagation, even if the linear elastic materials and the simplest Fick's diffusion are considered. Some of the parameters (e.g., diffusion coefficients, the reaction rate constant and the solubility of the diffusing reactant in the solid phase of the reaction product) cannot be easily estimated. That is why one of the aims was to validate and quantify the model of reaction front kinetics on the basis of experimental results. To do this, a high-temperature storage test was carried out for microchips with eutectic SnAg solder ball grid arrays and the kinetics of intermetallic compound growth was evaluated. These experimental results were used then to determine the kinetic parameters of the model. Such an evaluation in the context of the chemical affinity tensor concept was done for the first time and naturally required a comparison with the data given in other sources. The obtained diffusion coefficients correlate with the results from works of other researchers. Therefore, one can conclude that the chemical affinity tensor approach can be used to model the reaction front kinetics and that the kinetic parameters of the model can now be used as reference values for more general cases.

Thus a model of the propagation of chemical reaction fronts in deformable solids was formulated and numerically implemented. A comprehensive analysis of the kinetics and stability of such fronts was performed for various conditions and various types of mechanical loading. A practical basis has been created for expanding this model and numerical procedures for subsequent studies. An outlook for future research motivated by the obtained results may include:

(i) In this work the correlation of the analytical predictions with numerical results is shown and the analytical model is quantitatively verified with the use of experimental results. To complete the cross-validation circle, the numerical procedure might be utilized to simulate existing engineering problems with the parameters obtained from the experiment.

(ii) The proposed numerical procedure may be extended to the general case of large deformations. This development is needed, e.g., for modeling the reaction of silicon lithiation, which is accompanied with 300% volumetric expansion due to the chemical transformation or the silicon oxidation reaction with 100% volumetric expansion.

(iii) In this work only stationary diffusion equation was considered. However, if the characteristic time of the reaction is much less than the relative time of the diffusion, then the chemical reaction is diffusion controlled. For this case a dynamic diffusion equation should be utilized.

(iv) The processes of initial accumulation of diffusing reactant before starting the reaction and separation of the reaction front from the boundary of the body require an additional study.

List of Figures

1.1 Cross section of a solder bump prior (a) and after (b) current stressing, reprinted from Chao *et al.* [2007] 2
1.2 SEM morphology of 250 nm a-Si film on Cu after 1 (a), and 30 cycles (b), reprinted from Kasavajjula, Wang, and Appleby [2007] 2

2.1 A schematic representation of a localized chemical reaction in solids. 10
2.2 Unperturbed and perturbed interfaces Γ^0 and Γ. 17
2.3 A schematic representation of the planar chemical reaction front. 24
2.4 L_n-lines for the stability analysis of the planar chemical reaction front for stable (a) and unstable (b) sets of elastic parameters. 28
2.5 The contour plots of: (a) – γ for given external load in material parameter space; (b) – L_1 for given external load in material parameter space at corresponding γ from figure (a). Black solid lines in (b) represent the $L_1 = 0$ level. 29
2.6 A hollow cylinder undergoing a phase transformation. 31
2.7 Dependence of the driving force on the interface radius. . . . 32
2.8 Dependence of thermodynamically equilibrium interface radius on the external load for (a) – solid and (b) – hollow cylinders. Dashed line in (b) corresponds to the inner radius of the hollow cylinder. 33
2.9 L_n-lines for the stability analysis of the cylindrical phase interface for: (a) - stable set of elastic parameters for the solid cylinder, (b) - unstable set of elastic parameters for the solid cylinder, (c) - stable set of elastic parameters for the hollow cylinder with internal radius $r = 0.1R$, (d) - stable set of elastic parameters for the hollow cylinder with internal radius $r = 0.5R$. 36
2.10 L_n-lines for the stability analysis of the cylindrical chemical reaction front for: (a) – stable set of elastic parameters for the hollow cylinder with internal radius $r = 0.1R$, (b) – unstable set of elastic parameters for the solid cylinder. 37

2.11 Phase transition zones for the stable set of material parameters from Tab. 2.1. Blue and red dots correspond to the strain state for planar interface configuration. Dashed lines correspond to the condition (2.86), solid lines – to condition (2.88). 40
2.12 Phase transition zones for the stable set of material parameters from Table 2.3. Blue and red dots correspond to the strain state for cylindrical interface configuration. Dashed lines correspond to the condition (2.86), solid lines – to condition (2.88). . . . 40

3.1 The flowchart for the numerical algorithm. 45
3.2 Geometry described by NURBS curves which is directly used for the numerical simulation (a). Classical FE model for the numerical simulation (b). 46
3.3 Definition of the normal vector to the piecewise linear interface on the FE mesh 47
3.4 Automated adjustment of the interface position during its propagation. 48
3.5 (a) – set of reference points on the interface for the output. (b) – results of numerical simulations for stable (red curve) and unstable (blue curve) configurations for the phase transformation front propagation problem. 49
3.6 Typical shape of the phase interface after losing stability near the equilibrium radius during numerical simulation. 49
3.7 Shape of initially circular interface after the loss of stability on the FE mesh. 50
3.8 Results of numerical simulations for stable (red curve) and unstable (blue curve) configurations for the chemical reaction front propagation. 51
3.9 Kinetics of the initially perturbed interface with different predefined modes of instability for the unstable set of material parameters. Top row - “backward reaction”, bottom row - direct reaction. 52
3.10 The von Mises stress distribution for stable (a) and unstable (a) configurations. 52
3.11 Unstable configuration of a solid cylinder with predefined shape of the interface. Stress distributions are analyzed along radial lines OA and OB. 53
3.12 Distributions of von Mises stress along corresponding directions 53
3.13 Distributions of the hoop stress along corresponding directions 54
3.14 Distributions of the radial stress along corresponding directions 54

3.15 Results of numerical simulations by CutFEM and by the remeshing procedures. Propagation of a planar chemical reaction front for stable configuration is illustrated by the evolution of y-coordinate of three points of the front. 57
3.16 Results of numerical simulations by CutFEM and by the remeshing procedures. Kinetics of the initially perturbed interface for the unstable configuration is illustrated by four snapshots of the reaction front at different times. 58
3.17 Cropped examples of the finite-element meshes used in CutFEM and remeshing procedures are shown for the snapshot at $t = 17600$ in Fig. 3.16. 59
3.18 Propagation of the initially planar chemical reaction front in a body under shear loading. The kinetics is illustrated by four snapshots of the reaction front at different times. 60
3.19 Propagation of the initially planar chemical reaction front in a body under shear loading. The kinetics is illustrated by the evolution of y-coordinate of three points of the front. 61
3.20 Considered loading cases: biaxial stretching (a) and piecewise-linear prescribed displacement (b). 62
3.21 Intermediate and final configurations of a closed-curve reaction front in a 2D body under biaxial stretching. 63
3.22 Intermediate and final configurations of a closed-curve reaction front in a 2D body under complex loading. 64
3.23 Cropped examples of the finite-element meshes for final configuration of a of a closed-curve reaction front in a 2D body under complex loading. (a) – CutFEM results, (b) – remeshing results. 64
3.24 Model for the finite layer with circular pore or inclusion. . . . 65
3.25 Kinetics of the initially planar chemical interface in the vicinity of a cylindrical pore (a), a rigid inclusion (b), and in a uniform layer (c). 65
3.26 The von Mises stress distribution in the vicinity of a pore for the reaction front position shown in the right inset. 66
3.27 The von Mises stress distribution in the vicinity of a solid inclusion for the reaction front position shown in the right inset. 66

4.1 Cu-Sn phase diagram, reprinted from Fürtauer *et al.* [2013]. . 70
4.2 Photos of the microprocessor boards. 72
4.3 Cutting scheme applied to the microprocessor. 73
4.4 Cross-sections of a solder ball from Series I before heat treatment, general view (a) and interface zone (b). 74

4.5 First set of points from the interface region for EDXS analysis, a ball from Series I at $t = 1000$ h. The corresponding data is listed in Tab. 4.1. 75
4.6 Second set of points from the interface region for the EDXS analysis, a ball from Series I at $t = 1000$ h. The corresponding data is listed in Table 4.2. 76
4.7 Set of points from the interface region for the EDXS analysis a ball from Series II at $t = 1120$ h. The corresponding data is listed in Table 4.3. 77
4.8 Cross-section of a solder bump from Series I after $t = 120$ h heat treatment, general view (a) and enlarged region indicated by the red rectangle (b). 78
4.9 IMC profiles in the solder bump from Series I after heat treatment: $t = 120$ h (a) and $t = 240$ h (b). Spheroids of Cu_6Sn_5 are marked with green. 78
4.10 IMC profiles in a solder bump from Series I after heat treatment: $t = 360$ h (a), $t = 680$ h (b) and $t = 1000$ h (c). 79
4.11 Cross-section of a solder ball from Series II in the interface region before treatment at $t = 0$, (a), and after treatment, $t = 120$ h, (b). 79
4.12 Cross-section of the interface region in a ball from Series II after 480 h heat treatment. The chemical composition of the marked area obtained by the EDXS analysis is given in Tab. 4.4. . . 80
4.13 Cross-section of the IMC profile in a solder bump from Series II after heat treatment: $t = 800$ h (a) and $t = 1120$ h after additional polishing (b). 81
4.14 Growth of the mean thickness of Cu_6Sn_5 phase for the specimen from Series I and II. Experimental points are connected by dashed lines for visual clarity only. 81
4.15 Growth of the mean thickness of Cu_3Sn for the specimens from Series I and II. Experimental points are connected by dashed lines for visual clarity only. 82
4.16 Model description. 84
4.17 Fitted square root dependence (4.19) for Series I specimens. . 88
4.18 Fitted square root dependence (4.19) for Series II specimens. The point marked with asterisk was excluded from the fitting procedure due to bad surface condition of the specimen. . . . 89

List of Tables

2.1 Stable and unstable sets of material properties and parameters used in analytical study and numerical simulation for the planar interface problem. 30
2.2 Diffusion parameters used in analytical study and numerical simulation for the planar interface problem. 30
2.3 Material properties and parameters used in analytical and numerical simulation. Material "+" refers to the outer, material "−" to the inner region, respectively. 37

4.1 Data obtained from the EDXS analysis for the points in Fig. 4.5, values are given in at%. 75
4.2 Data obtained from the EDXS analysis for the points in Fig. 4.6, values are given in at%. 76
4.3 Data obtained from the EDXS analysis for the points in Fig. 4.7, values are given in at%. 77
4.4 Results of the EDXS analysis of the marked area in Fig. 4.12. 80
4.5 Mechanical material properties used in the model, Yang *et al.* [2008]; Jiang *et al.* [1997]. 86
4.6 Molar masses and densities used in the model, Sun and Yin [2009]. 87
4.7 Estimated diffusion coefficient for two series of specimens. . . 89
4.8 Comparison of the obtained estimation of the diffusion coefficient with literature data. [1] - Onishi and Fujibuchi [1975], [2] - Paul, Ghosh, and Boettinger [2011], [3] - Kumar, Handwerker, and Dayanada [2011], [4] - Yuan *et al.* [2015]. 89

Bibliography

Abeyaratne, R. and Knowles, J. K. (2006). *Evolution of Phase Transitions: A Continuum Theory*. Cambridge University Press.

Ahmad, Z. and Viswanathan, V. (2017). "Stability of electrodeposition at solid-solid interfaces and implications for metal anodes". In: *Physical Review Letters* 119 (5), p. 056003. DOI: 10.1103/PhysRevLett.119.056003. URL: https://link.aps.org/doi/10.1103/PhysRevLett.119.056003.

Antimonov, M. A., Cherkaev, A., and Freidin, A.B. (2016). "Phase transformations surfaces and exact energy lower bounds". In: *International Journal of Engineering Science* 98. Special Issue Dedicated to Sergey Kanaun´s 70th Birthday, pp. 153–182.

Arafat, Y. *et al.* (2020). "A Model for Intermetallic Growth in Thin Sn Joints Between Cu Substrates: Application to Solder Microjoints". In: *Journal of Electronic Materials*, pp. 1–16.

Baggetto, L., Danilov, D., and Notten, P. H. L. (2011). "Honeycomb-structured silicon: remarkable morphological changes induced by electrochemical (de)lithiation". In: *Advanced Materials* 23, pp. 1563–1566.

Ball, J. M. and James, R. D. (1987). "Fine phase mixtures as minimizers of energy". In: *Archive for Rational Mechanics and Analysis* 100, pp. 13–52.

Barvosa-Carter, W. and Aziz, M. J. (2004). "Interfacial roughening during solid phase epitaxy: Interaction of dopant, stress, and anisotropy effects". In: *Journal of Applied Physics* 96.10, pp. 5462–5468.

Barvosa-Carter, W. *et al.* (1998). "Kinetically Driven Growth Instability in Stressed Solids". In: *Physical Review Letters* 81.7, pp. 1445–1448.

Bordere, S. *et al.* (2018). "Understanding of Void Formation in Cu/Sn-Sn/Cu System During Transient Liquid Phase Bonding Process Through Diffusion Modeling". In: *Metallurgical and Materials Transactions B* 49, pp. 3343–3356.

Bourderau, S., Brousse, T., and Schleich, D. M. (1999). "Amorphous silicon as a possible anode material for Li-ion batteries". In: *Journal of Power Sources* 81–82, pp. 233–236.

Bowen, R. M. (1967). "Toward a thermodynamics and mechanics of mixtures". In: *Archive for Rational Mechanics and Analysis* 24.5, pp. 370–403.

Bower, A. F. and Guduru, P. R. (2012). "A simple finite element model of diffusion, finite deformation, plasticity and fracture in lithium ion insertion electrode materials". In: *Modelling and Simulation in Materials Science and Engineering* 20.4, p. 045004.

Brassart, L. and Suo, Z. (2013). "Reactive flow in solids". In: *Journal of the Mechanics and Physics of Solids* 61.1, pp. 61–77.

Burman, E. and Hansbo, P. (Apr. 2012). "Fictitious domain finite element methods using cut elements: II. A stabilized Nitsche method". In: *Applied Numerical Mathematics* 62.4, pp. 328–341. DOI: 10.1016/j.apnum.2011.01.008.

Burman, E. *et al.* (Jan. 2018). "Shape optimization using the cut finite element method". In: *Computer Methods In Applied Mechanics and Engineering* 328, pp. 242–261. DOI: 10.1016/j.cma.2017.09.005.

— (June 2019a). "Cut topology optimization for linear elasticity with coupling to parametric nondesign domain regions". In: *Computer Methods In Applied Mechanics and Engineering* 350, pp. 462–479. DOI: 10.1016/j.cma.2019.03.016.

— (2019b). "Hybridized CutFEM for elliptic interface problems". In: *SIAM Journal On Scientific Computing* 41.5, A3354–A3380. DOI: 10.1137/18M1223836.

Buttner, C. C. and Zacharias, M. (2006). "Retarded oxidation of Si nanowires". In: *Applied Physics Letters* 89.

Callister Jr., W. D. and Rethwisch, D (2010). *Material Science and engineering. An introduction.* 8th ed. Wiley.

Chang, S., Moon, J., and Cho, M. (2015). "Stress-diffusion coupled multiscale analysis of Si anode for Li-ion battery". In: *Journal of Mechanical Science and Technology* 29(11), pp. 4807–4816.

Chao, B. *et al.* (2007). "Investigation of diffusion and electromigration parameters for Cu–Sn intermetallic compounds in Pb-free solders using simulated annealing". In: *Acta Materialia* 55.8, pp. 2805–2814.

Chao, B. H.-L. *et al.* (2009). "Recent advances on kinetic analysis of electromigration enhanced intermetallic growth and damage formation in Pb-free solder joints". In: *Microelectronics Reliability* 49.3, pp. 253–263.

Chenchiah, I. V. and Bhattacharya, K. (2008). "The relaxation of two-well energies with possibility unequal moduli". In: *Archive for Rational Mechanics and Analysis* 187.3, pp. 409–479.

Chudnovsky, B. H. (2017). *Transmission, Distribution, and Renewable Energy Generation Power Equipment*. 2nd ed. CRC Press.

Cogan, S. F. *et al.* (1984). "Diffusion in the CuSn binary system: application to Nb_3Sn composites". In: *Journal of Materials Science* 19, pp. 497–500.

Cui, Z., Gao, F., and Qu, J. (2012a). "A finite deformation stress-dependent chemical potential and its applications to lithium ion batteries". In: *Journal of the Mechanics and Physics of Solids* 60, pp. 1280–1295.

— (2012b). "Interface-reaction controlled diffusion in binary solids with applications to lithiation of silicon in lithium-ion batteries". In: *Journal of the Mechanics and Physics of Solids* 61, pp. 293–310.

Dariavach, N. *et al.* (2006). "Intermetallic Growth Kinetics for Sn-Ag, Sn-Cu, and Sn-Ag-Cu Lead-Free Solders on Cu, Ni, and Fe-42Ni Substrates". In: *Journal of Electronic Materials* 35.7, pp. 1581–1592.

Duddu, R. *et al.* (Feb. 2011). "Diffusional evolution of precipitates in elastic media using the extended finite element and the level set methods". In: *Journal of Computational Physics* 230.4, pp. 1249–1264. DOI: 10.1016/j.jcp.2010.11.002.

Dybkov, V. I. (2010). *Reaction Diffusion and Solid State Chemical Kinetics: Handbook*. Trans Tech Publications Ltd.

Eremeev, V. A., Freidin, A. B., and Sharipova, L. L. (2003). "Nonuniqueness and Stability in Problems of Equilibrium of Elastic Two-Phase Bodies". In: *Doklady Physics* 48 (7), pp. 359–363.

— (2007). "The stability of the equilibrium of two phase elastic solids". In: *Journal of Applied Mathematics and Mechanics* 71, pp. 61–84.

Freidin, A. B. (1989). "Crazes and shear bands in glassy polymer as layers of a new phase". In: *Mechanics of Composite Materials* 1, pp. 1–7.

— (1999). "Small strains approach in the theory of strain induced phase transformations". In: *Strenth and Fracture of materials (Ed. N.F. Morozov), Studies on Elasticity and Plasticity (St. Petersburg University)* 18, 266–290, (in Russian).

— (2007). "On new phase inclusions in elastic solids". In: *ZAMM Journal of Applied Mathematics and Mechanics* 81.2, pp. 102–116.

Freidin, A. B. (2009). “On chemical reaction fronts in nonlinear elastic solids”. In: *Proceedings of XXXVII International Summer School-Conference Advanced Problems in Mechanics*. Ed. by Indeitsev, D.A. and Krivtsov, A. M., pp. 231–237.

— (2010). *Fracture mechanics: Eshelby problem (in Russian)*. St.Petersburg State Polytechnic University, St.Petersburg.

— (2013). “Chemical affinity tensor and stress-assist chemical reactions front propagation in solids”. In: *Proceedings of the ASME 2013 International Mechanical Engineering Congress and Exposition*. Vol. 9. American Society of Mechanical Engineers, V009T10A102.

— (2015). “On the chemical affinity tensor for chemical reactions in deformable materials”. In: *Mechanics of Solids* 50.3, pp. 260–285.

Freidin, A. B. and Chiskis, A.M. (1994a). “Phase transition zones in nonlinear elastic isotropic materials. Part 1: Basic relations”. In: *Izv. RAN, Mekhanika Tverdogo Tela (Mechanics of Solids)* 29.4, pp. 91–109.

— (1994b). “Phase transition zones in nonlinear elastic isotropic materials. Part 2: Incompressible materials with a potential depending on one of deformation invariants”. In: *Izv. RAN, Mekhanika Tverdogo Tela (Mechanics of Solids)* 29.5, pp. 46–58.

Freidin, A. B. and Sharipova, L. L. (2018). “Forbidden Strains and Stresses in Mechanochemistry of Chemical Reaction Fronts”. In: *Generalized Models and Non-classical Approaches in Complex Materials 1. Advanced Structured Materials*. Ed. by Altenbach, H. *et al.* Vol. 89. Springer Cham. Chap. 17, pp. 335–348.

— (2019). “Two-phase equilibrium microstructures against optimal composite microstructures”. In: *Archive of Applied Mechanics* 89, pp. 561–580.

Freidin, A. B. and Vilchevskaya, E. N. (2020). “Chemical Affinity Tensor in Coupled Problems of Mechanochemistry”. In: *Encyclopedia of Continuum Mechanics*. Ed. by Altenbach, H. and Öchsner, A. Berlin, Heidelberg: Springer Berlin Heidelberg.

Freidin, A. B., Vilchevskaya, E. N., and Korolev, I.K. (2014). “Stress-assist chemical reactions front propagation in deformable solids”. In: *International Journal of Engineering Science* 83, pp. 57–75.

Freidin, A. B. *et al.* (2006). “Spherically symmetric two-phase deformations and phase transition zones”. In: *International Journal of Solids and Structures* 43(14), pp. 4484–4508.

Freidin, A. B. *et al.* (2015). "Chemical reactions in spherically-symmetric problems of mechanochemistry". In: *Acta Mechanica* 227(1), pp. 43–56.

Freidin, A. B. *et al.* (2016). "Chemical affinity tensor and chemical reaction front propagation: Theory and FE-simulations". In: *International journal of Fracture* 202, pp. 245–259.

Fried, E. (1993). "Stability of a two-phase process in an elastic solid". In: *Journal of Elasticity* 31.3, pp. 163–187.

Fu, Y. B. and Freidin, A. B. (2004). "Characterization and stability of two-phase piecewise-homogeneous deformations". In: *The Royal Society* 46, pp. 3065–3094.

Fürtauer, S. *et al.* (2013). "The Cu–Sn phase diagram, Part I: New experimental results". In: *Intermetallics* 34, pp. 142 –147.

Gao, F. *et al.* (2006). "Microstructure and mechanical properties evolution of intermetallics between Cu and Sn-3.5Ag solder doped by Ni-Co additives". In: *Journal of Electronic Materials* 35, pp. 905–911.

Gao, H. *et al.* (2019). "Effect of nickel (Ni) on the growth rate of Cu_6Sn_5 intermetallic compounds between Sn–Cu–Bi solder and Cu substrate". In: *Journal of Materials Science: Materials in Electronics* 30, pp. 2186–2191.

Gibbs, J. (1948). *The Collected Works of J.W. Gibbs, Vol. 1: Thermodynamics.* Yale University Press.

Glansdorff, P. and Prigogine, I. (1971). *Thermodynamic theory of stability and fluctuation.* Wiley-interscience, New-York.

Grabovsky, Y. and Truskinovsky, L. (2011). "Roughening Instability of Broken Extremals". In: *Archive for Rational Mechanics and Analysis* 200 (1), pp. 183–202.

— (2013). "Marginal Material Stability". In: *Journal of Nonlinear Science* 23, pp. 891–969.

Grinfeld, M. A. (1980). "On conditions of thermodynamic equilibrium of phases of a nonlinearly elastic material". In: *Soviet Mathematics. Doklady.* 251, pp. 824–827.

— (1982). "Stability of heterogeneous equilibrium in system containing solid elastic phases". In: *Doklady Akademii Nauk SSSR* 253.6, pp. 836–840.

— (1990). *Methods of continuum mechanics in the theory of phase transformations.* in Russian. Nauka, Moscow.

Grinfeld, M. A. (1991). *Thermodynamic methods in the theory of heterogeneous systems*. Longman Sc & Tech.

Gross, D., Mueller, R., and Kolling, S. (2002). "Configurational forces - morphology evolution and finite elements". In: *Mechanics Research Communications* 29, pp. 529–536.

Gurtin, M. E. (1983). "Two-phase deformations of elastic solids". In: *Archive for Rational Mechanics and Analysis* 84.1, pp. 1–29.

— (2000). *Configurational forces as basic concepts of continuum physics*. Springer, New York, Berlin, Heidelberg.

Han, J. *et al.* (2017). "Effects of Grain Orientation on Cu_6Sn_5 Growth Behavior in Cu_6Sn_5-Reinforced Composite Solder Joints During Electromigration". In: *Journal of Electronic Materials* 47.2, pp. 1705–1712.

Hansbo, P. (2005). "Nitsche's method for interface problems in computa-tional mechanics". In: *GAMM-Mitteilungen* 28.2, pp. 183–206.

Hansbo, P., Larson, M. G., and Larsson, K. (2017). "Cut finite element methods for linear elasticity problems". In: *Geometrically Unfitted Finite Element Methods and Applications*. Ed. by Bordas, S. P. A. *et al.* Springer International Publishing, pp. 25–63.

Heidemeyer, H. *et al.* (2000). "Self-limiting and pattern dependent oxidation of silicon dots fabricated on silicon-on-insulator material". In: *Journal of Applied Physics* 87.9, pp. 4580–4585.

Hu, X. and Ke, Z. (2014). "Growth behavior of interfacial Cu–Sn intermetallic compounds of Cu/Sn reaction couples during dip soldering and aging". In: *Journal of Materials Science: Materials in Electronics* 25.2, pp. 936–945.

Huang, L. *et al.* (2015). "Thermodynamic understanding of Sn whisker growth on the Cu surface in Cu(top)-Sn(bottom) bilayer system upon room temperature aging". In: *Journal of Applied Physics* 117.21, p. 215308.

Hughes, T. J. R., Cottrell, J. A., and Bazilevs, Y. (2005). "Isogeometric analysis: CAD, finite elements, NURBS, exact geometry and mesh refinement". In: *Computer Methods in Applied Mechanics and Engineering* 194, pp. 4135–4195.

Hüter, C. *et al.* (2017). "Electrode-electrolyte interface stability in solid state electrolyte systems: Influence of coating thickness under varying residual stresses". In: *AIMS Materials Science* 4 (4), pp. 867–877.

Jadhav, N. *et al.* (2010). "Understanding the Correlation Between Intermetallic Growth, Stress Evolution, and Sn Whisker Nucleation". In: *IEEE Transactions on Electronics Packaging Manufacturing* 33.3, pp. 183–192.

James, R. D. (1981). "Finite deformation by mechanical twinning". In: *Archive for Rational Mechanics and Analysis* 77.2, pp. 143–176.

Jia, Z. and Li, T. (2015). "Stress-modulated driving force for lithiation reaction in hollow nano-anodes". In: *Journal of Power Sources* 275, pp. 866–876.

Jiang, Nan *et al.* (1997). "Thermal Expansion of Several Sn-Based Intermetallic Compounds". In: *Scripta Materialia* 37.12, pp. 1851 –1854.

Juntunen, M. and Stenberg, R. (2009). "Nitsche's Method for General Boundary Conditions". In: *Mathematics of Computation* 78.267, pp. 1353–1374.

Kao, D. *et al.* (1988). "Two-dimensional thermal oxidation of silicon. II. Modeling stress effects in wet oxides". In: *IEEE Transactions on Electron Devices* 35.1, pp. 25–37.

Kasavajjula, U., Wang, C., and Appleby, J. A. (2007). "Nano- and bulk-silicon-based insertion anodes for lithium-ion secondary cells". In: *Journal of Power Sources* 163, pp. 1003–1039.

Kim, H. K. and Tu, K. N. (1996). "Kinetic analysis of the soldering reaction between eutectic SnPb alloy and Cu accompanied by ripening". In: *Physical Review B* 53 (23), pp. 16027–16034.

Kim, K. S., Huh, S. H., and Suganuma, K. (2003). "Effects of intermetallic compounds on properties of Sn–Ag–Au lead-free soldered joints". In: *Journal of Alloys and Compounds* 352.1, pp. 226–236.

Knyazeva, A. G. (2003). "Cross Effects in Solid Media with Diffusion". In: *Journal of Applied Mechanics and Technical Physics* 44.3, pp. 373–384.

Kubanov, L. and Freidin, A. B. (1988). "Solid phase seeds in a deformable material". In: *Journal of Applied Mathematics and Mechanics* 52, pp. 382–389.

Kumar, S., Handwerker, C. A., and Dayanada, M. A. (2011). "Intrinsic and Interdiffusion in Cu–Sn System". In: *Journal of Phase Equilibria and Diffusion* 32, pp. 309–319.

Kunin, I. (1983). *Elastic media with microstructure*. Springer, Berlin.

Lee, B.-Z. and Lee, D. N. (1998). "Spontaneous growth mechanism of tin whiskers". In: *Acta Materialia* 46, pp. 3701–3714.

Lee, L. M. and Mohamad, A. A. (2013). "Interfacial Reaction of Sn–Ag-Cu Lead-Free Solder Alloy on Cu: A Review". In: *Advances in Materials Science and Engineering* 2013, pp. 1–11.

Levitas, V. I. and Hamed, A. (2013). "Anisotropic Compositional Expansion and Chemical Potential for Amorphous Lithiated Silicon under Stress Tensor". In: *Scientific Reports* 3:1615.

Liashenko, O., Gusak, A., and Hodaj, F. (2014). "Phase growth competition in solid/liquid reactions between copper or Cu3Sn compound and liquid tin-based solder". In: *Journal of Materials Science: Materials in Electronics* 25.10, pp. 4664–4672.

Lin, E. J. *et al.* (2017). "Effect of Cu solubility on electromigration in Sn(Cu) micro joint". In: *Journal of Applied Physics* 122.9, p. 095702.

Liu, A. A. *et al.* (1996). "Spalling of Cu6Sn5 spheroids in the soldering reaction of eutectic SnPb on Cr/Cu/Au thin films". In: *Journal of Applied Physics* 80.5, pp. 2774–2780.

Liu, X. H. *et al.* (2012a). "In situ atomic-scale imaging of electrochemical lithiation in silicon". In: *Nature Nanotechnology* 7, pp. 749–756.

Liu, X. H. *et al.* (2012b). "Size-Dependent Fracture of Silicon Nanoparticles During Lithiation". In: *ACSNANO* 6.2, pp. 1522–1531.

Liu, X. H. *et al.* (2013). "Self-Limiting Lithiation in Silicon Nanowires". In: *ACSNANO* 7.2, pp. 1495–1503.

Loeffel, K. and Anand, L. (2011). "A chemo-thermo-mechanically coupled theory for elastic–viscoplastic deformation, diffusion, and volumetric swelling due to a chemical reaction". In: *International Journal of Plasticity* 27.9, pp. 1409 –1431.

Marcus R. B.and Sheng, T. T. (1982). "The Oxidation of Shaped Silicon Surfaces". In: *Journal of The Electrochemical Society* 129.6, pp. 1278–1282.

Maugin, G. A. (2010). *Configurational forces. Thermomechanics, physics, mathematics, and numerics.* Chapman & Hall/CRC.

McDowell, Matthew T. *et al.* (2013). "In Situ TEM of Two-Phase Lithiation of Amorphous Silicon Nanospheres". In: *Nano letters* 13, pp. 758–764.

Mei, Z., Sunwoo, A. J., and Morris, J. W. (1992). "Analysis of low-temperature intermetallic growth in copper-tin diffusion couples". In: *Materials Science and Engineering: A* 23, pp. 857–864.

Mihalyi, A., Jaccodine, R. J., and Delph, T. J. (1999). "Stress effects in the oxidation of planar silicon substrates". In: *Applied Physics Letters* 74.14, pp. 1981–1983.

Min-Suk, S., Chan-Jin, P., and Hyuk-Sang, K. (2008). "Growth kinetics of Cu–Sn intermetallic compounds at the interface of a Cu substrate and 42Sn–58Bi electrodeposits, and the influence of the intermetallic compounds on the shear resistance of solder joints". In: *Materials Chemistry and Physics* 110.1, pp. 95–99.

Moghadam, M. M. and Voorhees, P. W. (2016). "Thin film phase transformation kinetics: From theory to experiment". In: *Scripta Materialia* 124, pp. 164–168.

Monroe, C. and Newman, J. (2004). "The Effect of Interfacial Deformation on Electrodeposition Kinetics". In: *Journal of The Electrochemical Society* 151.6, A880–A886.

Morganti, S. *et al.* (2015). "Patient-specific isogeometric structural analysis of aortic valve closure". In: *Computer Methods in Applied Mechanics and Engineering* 284, pp. 508–520.

Morozov, A. V., Freidin, A. B., and Müller, W. H. (2019). "Stability of chemical reaction fronts in the vicinity of a blocking state". In: *PNRPU Mechanics Bulletin* 2019.3, pp. 58–64.

Morozov, A. V. *et al.* (2020). "Experimental and Theoretical Studies of Cu-Sn Intermetallic Phase Growth During High-Temperature Storage of Eutectic SnAg Interconnects". In: *Journal of Electronic Materials*.

Morozov, N. F. and Freidin, A. B. (1998). "Zones of Phase Transitions and Phase Transformations in Elastic Bodies under Various Stress States". In: *Proceedings of the Steklov Institute of Mathematics* 223, pp. 219–232.

Mueller, R. and Gross, D. (1998). "3D simulation of equilibrium morphologies of precipitates". In: *Computational Materials Science* 11, pp. 35–44.

— (1999). "3D inhomogeneous, misfitting second phase particles equilibrium shapes and morphological development". In: *Computational Materials Science* 16, pp. 53–60.

Mueller, R., Gross, D., and Lupascu, D. C. (2006). "Driving forces on domain walls in ferroelectric materials and interaction with defects". In: *Computational Materials Science* 35, pp. 42–52.

Muhlstein, C., Brown, S., and Ritchie, R. (2002). "High-cycle fatigue and durability of polycrystalline silicon thin films in ambient air". In: *Sensors and Actuators* A94, pp. 177–188.

Muhlstein, C. and Ritchie, R. (2003). “High-cycle fatigue of micronscale polycrystalline silicon films: fracture mechanics analyses of the role of the silica/silicon interface”. In: *International Journal of Fracture* 119/120, pp. 449–474.

Muhlstein, C., Stach, E., and Ritchie, R. (2001). “A reaction-layer mechanism for the delayed failure of micron-scale polycrystalline silicon structural films subjected to high-cycle fatigue loading”. In: *Acta Materialia* 50, pp. 3579–3595.

Müller, W. H., Vilchevskaya, E. N., and Freidin, A. B. (2015). “Structural changes in micro-materials: Phenomenology, theory, applications, and simulations”. In: *Lecture Notes of TICMI* 16, pp. 3–72.

Natsiavas, P. P. *et al.* (2016). “Effect of prestress on the stability of electrode–electrolyte interfaces during charging in lithium batteries”. In: *Journal of the Mechanics and Physics of Solids* 95, pp. 92 –111.

Onishi, M. and Fujibuchi, M. (1975). “Reaction-Diffusion in the Cu–Sn System”. In: *Transactions of the Japan Institute of Metals* 16, pp. 539–547.

Ortiz, M., Repetto, E. A., and Si, H. (1999). “A continuum model of kinetic roughening and coarsening in thin films”. In: *Journal of the Mechanics and Physics of Solids* 47.4, pp. 697–730.

Osmolovsky, V. G. (2000). *The variational problem of phase transitions in continuum mechanics*. in Russian. Publ. of SPb university, St.Petersburg.

Paul, A. (2004). “The Kirkendall effect in solid state diffusion”. English. PhD thesis. Department of Chemical Engineering and Chemistry. ISBN: 90-386-2646-0.

Paul, A., Ghosh, C., and Boettinger, W. J. (2011). “Diffusion Parameters and Growth Mechanism of Phases in the Cu–Sn System”. In: *Metallurgical and Materials Transactions A* 42A, pp. 952–963.

Phan, A.-V. *et al.* (2001). “On Transient Layers as New Phase Domains in Composite Materials”. In: *Modelling and simulation in materials science and engineering* 9.1, pp. 309–325.

Poluektov, M. and Figiel, Ł. (2019). “A numerical method for finite-strain mechanochemistry with localised chemical reactions treated using a Nitsche approach”. In: *Computational Mechanics* 63.5, pp. 885–911.

Prigogine, I. and Defay, R. (1954). *Chemical thermodynamics*. Longmans, Green.

Ross, G., Vuorinen, V., and Paulasto-Kröckel, M. (2016). "Void formation and its impact on CuSn intermetallic compound formation". In: *Journal of Alloys and Compounds* 677, pp. 127 –138.

Rusanov, A. I. (2005). "Surface thermodynamics revisited". In: *Surface Science Reports* 58.5-8, pp. 111–239.

— (2006). *Thermodynamic foundations of mechanochemistry*. in Russian. Nauka, St. Petersburg.

Sang, X., Du, K., and Ye, H. (2009). "An ordered structure of Cu_3Sn in Cu-Sn alloy investigated by transmission electron microscopy". In: *Journal of Alloys and Compounds* 469 (1), pp. 129–136.

Schaefer, M., Fournelle, R. A., and Liang, J. (1998). "Theory for intermetallic phase growth between Cu and liquid Sn-Pb solder based on grain boundary diffusion control". In: *Journal of Electronic Materials* 27.11, pp. 1167–1176.

Schneider, D. *et al.* (Aug. 2017). "On the stress calculation within phase-field approaches: A model for finite deformations". In: *Computational Mechanics* 60.2, pp. 203–217.

Schneider, D. *et al.* (Mar. 2018). "Small strain multiphase-field model accounting for configurational forces and mechanical jump conditions". In: *Computational Mechanics* 61.3, pp. 277–295.

Silhavy, M. (1997). *The Mechanics and Thermodynamics of Continuous Media*. Springer-Verlag Berlin, Heidelberg.

Sobiech, M. *et al.* (2011). "Phase formation at the Sn/Cu interface during room temperature aging: Microstructural evolution, whiskering, and interface thermodynamics". In: *Journal of Materials Research* 26.12, pp. 1482–1493.

Suganuma, K. (2003). *Lead-Free Soldering in Electronics: Science, Technology, and Environmental Impact*. New York: CRC Press, Marcel Dekker.

Sun, F. and Yin, Z. (2009). "The interfacial Cu-Sn intermetallic compounds (IMCs) growth behavior of Cu/Sn/Cu sandwich structure via induction heating method". In: *Journal of Materials Science: Materials in Electronics* 30, pp. 18878–18884.

Sunwoo, A. J., Morris, J. W., and Lucey, G. K. (1992). "The growth of Cu-Sn intermetallics at a pretinned copper-solder interface". In: *Metallurgical Transactions A* 23 (4), pp. 1323–1332.

Svendsen, B., Shanthraj, P., and Raabe, D. (Mar. 2018). "Finite-deformation phase-field chemomechanics for multiphase, multicomponent solids". In: *Journal of the Mechanics and Physics of Solids* 112, pp. 619–636.

Truesdell, C. (1969). *Rational Thermodynamics*. McGraw-Hill, London.

Vilchevskaya, E. N., Filippov, R. A., and Freidin, A. B. (2013). "On Transient Layers as New Phase Domains in Composite Materials". In: *Mechanics of Solids* 48.1, pp. 92–118.

Vilchevskaya, E. N. and Freidin, A. B. (2007). "On Phase Transitions in a Domain of Material Inhomogeneity. I. Phase Transitions of an Inclusions in a Homogeneous External Field". In: *Mechanics of Solids* 42.5, pp. 823–840.

— (2013). "On kinetics of chemical reaction fronts in elastic solids". In: *Surface Effects in Solid Mechanics*. Ed. by Altenbach, H. and Morozov, N. F. Springer Berlin Heidelberg, pp. 181–194.

Wang, Y. *et al.* (2020). "Effect of Sn Grain c-Axis on Cu Atomic Motion in Cu Reinforced Composite Solder Joints Under Electromigration". In: *Journal of Electronic Materials* 49, pp. 2159–2163.

Weinberg, K., Werner, M., and Anders, D. (Feb. 2018). "A chemo-mechanical model of diffusion in reactive systems". In: *Entropy* 20.2, p. 140.

Xin, M. *et al.* (2003). "Development of Cu–Sn intermetallic compound at Pb-free solder/Cu joint interface". In: *Materials Letters* 57.22, pp. 3361–3365.

Yang, F. (2010). "Effect of local solid reaction on diffusion-induced stress". In: *Journal of Applied Physics* 107.

Yang, P.-F. *et al.* (2008). "Nanoindentation identifications of mechanical properties of Cu_6Sn_5, Cu_3Sn, and Ni_3Sn_4 intermetallic compounds derived by diffusion couples". In: *Materials Science and Engineering: A* 485, pp. 305–310.

Yu, D. Q. and Wang, L. (2008). "The growth and roughness evolution of intermetallic compounds of Sn–Ag–Cu/Cu interface during soldering reaction". In: *Journal of Alloys and Compounds* 458.1, pp. 542–547.

Yu, D. Q. *et al.* (2005). "Intermetallic compounds growth between Sn–3.5Ag lead-free solder and Cu substrate by dipping method". In: *Journal of Alloys and Compounds* 392.1, pp. 192–199.

Yuan, Y. *et al.* (2015). "Investigation of diffusion behavior in Cu–Sn solid state diffusion couples". In: *Journal of Alloys and Compounds* 661, pp. 282–293.

Zeeshan, A. and Venkatasubramanian, V. (2017). "Kinetically Driven Growth Instability in Stressed Solids". In: *Physical Review Letters* 119.5, p. 056003.

Zenga, Z. *et al.* (2016). "In situ measurement of lithiation-induced stress in silicon nanoparticles using micro-Raman spectroscopy". In: *Nano Energy* 22, pp. 105–110.

Zhao, K. *et al.* (2012a). "Concurrent Reaction and Plasticity During Initial Lithiation of Crystalline Silicon in Lithium-Ion Batteries". In: *ECS Meeting Abstracts*.

Zhao, K. *et al.* (2012b). "Fracture and debonding in lithium-ion batteries with electrodes of hollow core shell nanostructures". In: *Journal of Power Sources* 218, pp. 6–14.

Zhao, X. J., Bordas, S. P. A., and Qu, J. M. (Dec. 2013). "A hybrid smoothed extended finite element/level set method for modeling equilibrium shapes of nano-inhomogeneities". In: *Computational Mechanics* 52.6, pp. 1417–1428.

— (Aug. 2015). "Equilibrium morphology of misfit particles in elastically stressed solids under chemo-mechanical equilibrium conditions". In: *Journal of the Mechanics and Physics of Solids* 81, pp. 1–21.

Zhao, X. J. *et al.* (June 2013). "Effects of elastic strain energy and interfacial stress on the equilibrium morphology of misfit particles in heterogeneous solids". In: *Journal of the Mechanics and Physics of Solids* 61.6, pp. 1433–1445.

A Analytical solutions for planar and cylindrical reaction fronts kinetics

One should note that analytical solutions based on the chemical affinity tensor concept for various simple geometries were obtained in many works, *e.g.* for planar interface in Freidin, Vilchevskaya, and Korolev [2014]; Morozov *et al.* [2018b], for cylindrical problems in Vilchevskaya and Freidin [2013]; Morozov *et al.* [2018a], and for spherically symmetric problems in Freidin [2015]; Freidin *et al.* [2015]. Here the solutions for planar and cylindrical problems are presented in a form used as unperturbed solutions in the stability analyses given in Sections 2.3 – 2.5. Also, these solutions were used as a reference to validate the numerical results in Chapter 3.

A.1 Planar reaction front kinetics

As an example, a chemical reaction in the infinite layer of thickness H is considered, as illustrated in Fig. 2.3. The diffusing constituent is supplied through the lower boundary. This gives the following boundary conditions for equations (2.19) and (2.21):

$$\begin{aligned}
&\mathbf{u} = \mathbf{0}, \qquad \text{at } y = 0,\\
&\mathbf{u} = u_0 \mathbf{e}_y, \qquad \text{at } y = H,\\
&\mathbf{u}\cdot\mathbf{e}_x = 0, \qquad \boldsymbol{\sigma} : \mathbf{e}_x\mathbf{e}_y = 0, \qquad \text{at } x = 0 \text{ and } x = L,\\
&D\mathbf{n}\cdot\nabla c + \alpha\,(c - c_*) = 0, \qquad \text{at } y = 0,\\
&\mathbf{n}\cdot\nabla c = 0, \qquad \text{at } x = 0 \text{ and } x = L.
\end{aligned} \tag{A.1}$$

Solid constituents are assumed to be linear elastic and isotropic:

$$\boldsymbol{\sigma}_- = \mathbf{C}_- : \boldsymbol{\varepsilon}_-, \quad \boldsymbol{\sigma}_+ = \mathbf{C}_+ : (\boldsymbol{\varepsilon}_+ - \boldsymbol{\varepsilon}^{\mathrm{tr}}), \tag{A.2}$$

$$\mathbf{C}_\pm = \lambda_\pm \mathbf{II} + 2\mu_\pm {}^4\mathbf{I}, \tag{A.3}$$

where $\lambda_\pm$ and $\mu_\pm$ are Lamé parameters.

Due to the symmetry of the problem solutions for displacements and con-

centration depend only on y coordinate. Hence, they can be found as

$$\begin{aligned} \mathbf{u}_{\pm} &= \left(A^{\pm} y + B^{\pm}\right) \mathbf{e}_y, \\ c &= A^c y + B^c. \end{aligned}$$

Introducing the parameter $\zeta = h/H$, the constants can be found from the boundary conditions (A.1) as:

$$\begin{aligned} A^+ &= \frac{u_0/H(\lambda_- + 2\mu_-) + \theta(\lambda_+ + \mu_+)(1-\zeta)}{\zeta(\lambda_- + 2\mu_-) + (1-\zeta)(\lambda_+ + 2\mu_+)}, \\ A^- &= \frac{u_0/H(\lambda_+ + 2\mu_+) - \theta(\lambda_+ + \mu_+)\zeta}{\zeta(\lambda_- + 2\mu_-) + (1-\zeta)(\lambda_+ + 2\mu_+)}, \\ B^+ &= 0, \qquad B^- = H\left(\frac{u_0}{H} - A^-\right). \end{aligned} \tag{A.4}$$

One should note that $\boldsymbol{\varepsilon}_{\pm} = A^{\pm}\mathbf{e}_y\mathbf{e}_y$ and stresses can be obtained from (A.2). These stresses and strains are substituted into the expression for A_{nn}

$$A_n = \frac{n_- M_-}{\rho_-}\chi_\zeta + n_* RT \ln\frac{c}{c_*}, \tag{A.5}$$

where χ_ζ is defined by Eq. (2.23) and represents the mechanical contribution to the chemical affinity tensor at the interface position ζ.

The reaction rate can be rewritten as

$$\begin{aligned} \omega &= k_* c\left(1 - \exp\left(-\frac{A_{NN}}{RT}\right)\right) = \\ &= k_* c\left(1 - \exp\left(-\frac{n_- M_-}{\rho_- RT}\,\chi_\zeta - \ln\frac{c}{c_*}\right)\right). \end{aligned} \tag{A.6}$$

Now if the following notation is introduced,

$$e_\zeta = \exp\left(-\frac{n_- M_-}{\rho_- RT}\,\chi_\zeta\right). \tag{A.7}$$

a splitting of the exponent leads to

$$\omega = k_* c\left(1 - e_\zeta\frac{c_*}{c}\right) = k_*(c - e_\zeta c_*). \tag{A.8}$$

With this expression for the reaction rate, boundary conditions for the diffusion

problem reads

$$\begin{aligned} D\frac{\mathrm{d}c}{\mathrm{d}y}\bigg|_{y=h} + k_*(c(h) - e_\zeta c_*) = 0, \\ - D\frac{\mathrm{d}c}{\mathrm{d}y}\bigg|_{y=0} - a(c_* - c(0)) = 0. \end{aligned} \tag{A.9}$$

Then, the constants for the solution can be found uniquely

$$A^c = -\frac{k_* c_* (1 - e_\zeta)}{D\left(1 + \dfrac{k_*}{a}\right) + k_* h}, \quad B^c = c_* + \frac{D}{a} A^c, \tag{A.10}$$

and the reaction rate as a function of the current thickness has the form

$$\omega(h) = \frac{k_* c_* (1 - e_\zeta) D}{D\left(1 + \dfrac{k_*}{a}\right) + k_* h}.$$

One should note that e_ζ is also a function of current thickness. Then according to Eq. (2.6) the reaction front velocity reads:

$$V_y = \frac{\mathrm{d}h}{\mathrm{d}t} = \frac{n_- M_-}{\rho_-}\omega = \frac{n_- M_-}{\rho_-} \frac{k_* c_* (1 - e_\zeta) D}{D\left(1 + \dfrac{k_*}{a}\right) + k_* h}. \tag{A.11}$$

This equation can be integrated numerically with explicit Euler scheme with given initial thickness h_0 and time increment δt:

$$h_{i+1} = h_i + V_y^i \delta t, \tag{A.12}$$

where V_y^i is the front velocity calculated at i^{th} iteration, and $i = 1, 2 \cdots$ is the iteration number.

A.2 Cylindrical reaction front kinetics

The plane strain problem for the hollow and solid cylinder undergoing chemical reaction (Figure 2.6) is considered. The internal and external radii are a and b, respectively, the current position of the reaction front is a cylindrical surface of the radius ρ. Diffusing reactant is supplied through the outer surface of the cylinder. The transformation strain is assumed to be plane:

$$\boldsymbol{\varepsilon}^{\mathrm{tr}} = \varepsilon^{\mathrm{tr}}(\mathbf{e}_r \mathbf{e}_r + \mathbf{e}_\phi \mathbf{e}_\phi), \tag{A.13}$$

where $\boldsymbol{e}_r$ and $\boldsymbol{e}_\phi$ are the unit vectors of the cylindrical coordinates. Solid constituents are assumed to be linear elastic and isotropic as in the previous example, (A.2).

In order to find the stresses and strains at the reaction front we use the equilibrium equation, which in the case of axial symmetry takes the form

$$\frac{\mathrm{d}\sigma_r}{\mathrm{d}r} + \frac{\sigma_r - \sigma_\phi}{r} = 0 \tag{A.14}$$

with boundary conditions for the hollow cylinder

$$\sigma_r(a) = 0, \quad \sigma_r(b) = 0, \quad [\![u(\rho)]\!] = 0, \quad [\![\sigma_r(\rho)]\!] = 0 \tag{A.15}$$

or for the solid cylinder

$$u_r|_{r\to 0} = 0, \quad \sigma_r(b) = 0, \quad [\![u(\rho)]\!] = 0, \quad [\![\sigma_r(\rho)]\!] = 0. \tag{A.16}$$

The radial displacement is given by the Lamé solution:

$$u_\pm(r) = A_\pm r + \frac{B_\pm}{r}, \tag{A.17}$$

and the strains can be found through

$$\boldsymbol{\varepsilon}_r^\pm(r) = \frac{\mathrm{d}u_\pm(r)}{\mathrm{d}r} = A_\pm - \frac{B_\pm}{r^2}, \qquad \boldsymbol{\varepsilon}_\phi^\pm(r) = \frac{u_\pm(r)}{r} = A_\pm + \frac{B_\pm}{r^2}. \tag{A.18}$$

Four unknown constants $A_\pm$ and $B_\pm$ can be found from the boundary conditions (A.15) or (A.16), and *e.g.* for the case of solid cylinder:

$$\begin{aligned} A_+ &= \frac{\dfrac{u_0}{b}(\lambda_- + \mu_- + \mu_+) + \varepsilon^{\mathrm{tr}}\zeta^2(\lambda_+ + \mu_+)}{\zeta^2(\lambda_+ + 2\mu_+) + (1-\zeta^2)(\lambda_- + \mu_- + \mu_+)}, \\ A_- &= \frac{1}{\zeta^2}\left(\frac{u_0}{b} + (\zeta^2 - 1)A_+\right), \\ B_+ &= b^2\left(\frac{u_0}{b} - A_+\right), \qquad B_- = 0 \end{aligned} \tag{A.19}$$

where $\zeta = \rho/b$.

The stresses and strains at the reaction can then be found from (A.2) and (A.18), respectively. These stresses and strains are substituted into the expression for A_{nn}

$$A_n = \frac{n_- M_-}{\rho_-}\chi_\zeta + n_* RT \ln\frac{c}{c_*}, \tag{A.20}$$

where χ_ζ is defined by Eq. (2.23) and represents the mechanical contribution to the chemical affinity tensor at the interface position ζ.

As in the previous example in A.1, the reaction rate takes form (A.8) with same notation for the e_ζ (which depends on the current interface radius) being introduced.

The corresponding stationary diffusion equation in the case of axial symmetry becomes:

$$\frac{\mathrm{d}}{\mathrm{d}r}\left(\frac{1}{r}\frac{\mathrm{d}c}{\mathrm{d}r}\right) = 0, \quad r \in [\rho, b]. \tag{A.21}$$

Boundary and interface conditions according to the notation of Figure 2.6 can be written as follows (as described in Section 2.1):

$$D\frac{\mathrm{d}c}{\mathrm{d}r}\bigg|_{r=b} - \alpha(c_* - c(b)) = 0, \qquad D\frac{\mathrm{d}c}{\mathrm{d}r}\bigg|_{r=\rho} - k_*\left(c(\rho) - c_* e_\zeta\right) = 0. \tag{A.22}$$

In a cylindrical coordinate system the solution of the Laplace equation can be found as follows:

$$c(r) = C_1 \ln\left(\frac{r}{b}\right) + C_2. \tag{A.23}$$

The two unknown constants C_1 and C_2 can be found uniquely from the boundary conditions (A.22):

$$C_1 = \frac{c_*(e_\zeta - 1)}{\ln\dfrac{\rho}{b} - D\left(\dfrac{1}{k_*\rho} + \dfrac{1}{\alpha b}\right)}, \quad C_2 = c_* - \frac{D}{\alpha b}C_1. \tag{A.24}$$

From (A.23), (A.24) it follows that

$$c(\rho) = \frac{c_*}{\ln\dfrac{\rho}{b} - D\left(\dfrac{1}{k_*\rho} + \dfrac{1}{\alpha b}\right)}\left\{\left(\ln\frac{\rho}{b} - \frac{D}{\alpha b}\right)e_\zeta - \frac{D}{k_*\rho}\right\} \tag{A.25}$$

Since $\mathbf{n} = -\mathbf{e}_r$ the normal component of the reaction front velocity is

$$V_r = -\frac{\mathrm{d}\rho}{\mathrm{d}t} = \frac{n_- M_-}{\rho_-} k_*\left(c(\rho) - c_* e_\zeta\right), \tag{A.26}$$

and the reaction front kinetics – the dependence $\rho(t)$ – can be obtained by integration of Eq. (A.26) where the dependencies $c(\rho)$ and e_ζ are already found.